AD

USAAVLABS TECHNICAL REPORT 68-18C

PREDICTION OF ROTOR INSTABILITY AT HIGH FORWARD SPEEDS

VOLUME III
STALL FLUTTER

By

Franklin O. Carta

Charles F. Niebanck

February 1969

U. S. ARMY AVIATION MATERIEL LABORATORIES
FORT EUSTIS, VIRGINIA

CONTRACT DA 44-177-AMC-332(T)

UNITED AIRCRAFT CORPORATION
SIKORSKY AIRCRAFT DIVISION
STRATFORD, CONNECTICUT

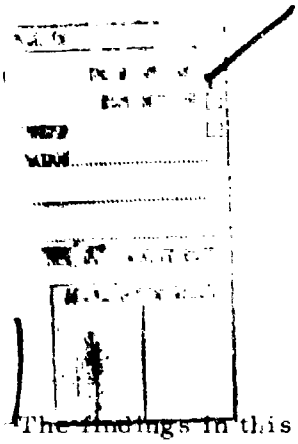

Disclaimers

The findings in this report are not to be construed as an official Department of the Army position unless so designated by other authorized documents.

When Government drawings, specifications, or other data are used for any purpose other than in connection with a definitely related Government procurement operation, the United States Government thereby incurs no responsibility nor any obligation whatsoever; and the fact that the Government may have formulated, furnished, or in any way supplied the said drawings, specifications, or other data is not to be regarded by implication or otherwise as in any manner licensing the holder or any other person or corporation, or conveying any rights or permission, to manufacture, use, or sell any patented invention that may in any way be related thereto.

Disposition Instructions

Destroy this report when no longer needed. Do not return it to the originator.

DEPARTMENT OF THE ARMY
U. S. ARMY AVIATION MATERIEL LABORATORIES
FORT EUSTIS, VIRGINIA 23604

This contract was initiated to determine the aeroelastic stability limits of articulated and unarticulated helicopter rotor systems at high forward speeds. The four primary modes of aeroelastic instability (classical flutter, stall flutter, torsional divergence, and flapping or flatwise bending instability) were investigated. The possibility of a flap-lag instability suggested by Dr. Maurice I. Young of the Vertol Division, The Boeing Company, was inves igated as a special case of flapping instability.

The results are published as a five-volume set; the subject of each volume is as follows:

Volume I	Equations of Motion
Volume II	Classical Flutter
Volume III	Stall Flutter
Volume IV	Torsional Divergence
Volume V	Flapping Instability

These reports have been reviewed by the U. S. Army Aviation Materiel Laboratories. These reports, which are published for the exchange of information and the stimulation of ideas, are considered to be technically sound with regard to technical approach, results, conclusions, and amended parameter ranges for accurate usage.

Task 1F125901A13904
Contract DA 44-177-AMC-332(T)
USAAVLABS Technical Report 68-18C
February 1969

PREDICTION OF ROTOR INSTABILITY AT HIGH FORWARD SPEEDS

SER-50469

Volume III

Stall Flutter

By

Franklin O. Carta
and
Charles F. Niebanck

Prepared by

United Aircraft Corporation
Sikorsky Aircraft Division
Stratford, Connecticut

for

U. S. ARMY AVIATION MATERIEL LABORATORIES
FORT EUSTIS, VIRGINIA

SUMMARY

The purposes of this research program were to extend or develop analytical methods for determining rotor blade aeroelastic stability limits and to perform stability calculations over a range of design and operating variables for articulated and nonarticulated configurations. The usefulness of simpler analytical methods was investigated by comparing results with operating boundaries from the more elaborate analysis.

The analytical study in this volume was carried out to determine the susceptibility of helicopter rotor blades to a stall flutter instability. This analysis was based on the use of unsteady aerodynamic data previously obtained by Sikorsky Aircraft for an NACA 0012 airfoil oscillating in pitch about its quarter-chord over a wide range of values of incidence angle, oscillatory frequency, amplitude of motion, and free-stream velocity. These data were originally available in the form of moment coefficient-incidence angle loops, and a twofold task was performed in carrying out the present study. First, it was necessary to convert the moment coefficient data to an aerodynamic damping parameter form. This was accomplished by integrating the moment over one cycle of motion to yield the aerodynamic work per cycle, and this in turn was multiplied by appropriate conversion factors to produce the desired two-dimensional aerodynamic damping. Second, it was necessary to apply these two-dimensional results to a helicopter rotor to evaluate the weighted three-dimensional damping at each azimuth station, and to interpret the implications of any predicted region of instability.

It was found that under certain combinations of forward speed and high disc loading, a helicopter rotor blade could encounter regions of negative torsional aerodynamic damping while operating as a retreating blade. The extent of the negative damping regime was sensitive to change in incidence angle distribution, and for some parameter combinations it could produce two or three cycles of unstable torsional motion per revolution.

Generally good agreement was found to exist between the results of the present study and those of other investigators at all stages in the development; e.g., the two-dimensional damping data were in good agreement with the results of Reference 1 and the final three-dimensional damping variation with azimuth over the rotor disc was in qualitatively good agreement with the recent work of Reference 2.

The stall flutter analysis was used in conjunction with the blade motion solution of Volume I to provide flight condition boundaries for stall flutter intensity.

FOREWORD

The investigation presented in this volume is part of an extensive study, which is presented in five volumes. The work was performed under Contract DA 44-177-AMC-337(T) with the U. S. Army Aviation Materiel Laboratories, Fort Eustis, Virginia. The program was monitored for USAAVLABS by Mr. Joseph McGarvey.

The rotor blade stall flutter analysis presented in this volume is the work of Mr. Franklin O. Carta of the United Aircraft Research Laboratories. The test data used in the analysis are from a wind tunnel test which was performed previously under Sikorsky Aircraft sponsorship.

The subheading entitled "Stall Flutter Flight Condition Boundaries" is the result of work done at Sikorsky Aircraft by Mr. Charles F. Niebanck. The information under that subheading is the result of the application of the stall flutter analysis of this volume in conjunction with the Extended Normal Mode Transient Analysis of Volume I.

Volume I of this report contains the development of the differential equations of motion of an elastic rotor blade with chordwise mass unbalance.

Volume II presents a linearized discrete azimuth classical flutter analysis for rotor blades, with an appropriate parameter variation study, a comparison with test data, and a comparison with results calculated by using the method of Volume I.

Volume IV contains the results of a study of static torsional divergence. A set of design charts and the effects of a range of parameter variations are presented. The results of the static divergence calculation are compared with results calculated by using the method of Volume I.

Volume V presents the results of a study of flapping and coupled flap-lag instabilities. The results of a parametric study based on a single degree-of-freedom flapping or flatwise bending analysis are presented. Comparisons are made with results from the more elaborate method of Volume I. The results obtained by using the method of Volume I to determine the coupled flap-lag response of a rotor to a number of sudden control changes are presented.

BLANK PAGE

CONTENTS

LIST OF ILLUSTRATIONS

LIST OF TABLES

LIST OF SYMBOLS

a	dimensionless distance of pivot axis of the mid-chord, in semichords, Eq. (9)
a_{1s}	blade lateral flapping, deg
b	semichord, ft, Eq. (7)
b_{1s}	blade longitudinal flapping, deg
c	damping coefficient, ft-lb-sec, Eq. (19)
c_A	chord, ft
C_L/σ	rotor lift coefficient - solidity ratio
C_Q/σ	rotor torque coefficient - solidity ratio
$C(k)$	Theodorsen's circulation function
C_M	moment coefficient, Eq. (11)
C_N	normal force coefficient, Eq. (10)
C_W	work coefficient, Eq. (14)
f	oscillatory frequency in pitch, cps
f_a	mode shape distribution, Eq. (41)
$F(k)$	real part of Theodorsen's function, Eq. (5)
$G(k)$	imaginary part of Theodorsen's function, Eq. (5)
h	bending deflection, ft
$i =$	$\sqrt{-1}$
I	inertia, ft-lb-sec^2, Eq. (19)
k	reduced frequency parameter, Eq. (7)
L	unsteady lift function, Eq. (37), or lift, lb, Eq. (48)
M	unsteady moment function, Eq. (37), or moment, ft-lb, Eq. (9), or Mach number
M_1, M_2, M_3	unsteady moment components, Eq. (22)
N	normal force, lb, Eq. (8)

p	pressure, lb/ft^2, Eq. (1)
Δp	pressure difference, lb/ft^2, Eq. (1)
q	dynamic pressure, lb/ft^2, Eq. (4)
Q	generalized force, Eq. (89)
r	radial distance, ft
R	rotor radius, ft
t	time, sec, Eq. (1)
U	velocity relative to airfoil, ft/sec, Eq. (4)
U_T	reference relative velocity, chosen at the blade tip for the 0 azimuth position, ft/sec
V	aircraft forward velocity, ft/sec
W	work, ft-lb, Eq. (13)
x	dimensionless chordwise station, Eq. (5)
α	incidence angle, deg or rad, Eq. (12)
$\bar{\alpha}$	oscillatory amplitude, deg or rad, Eq. (16)
α_M	mean incidence angle, deg or rad, Eq. (66)
α_s	stalling angle, deg or rad, Eq. (66)
α_{SH}	rotor shaft angle of attack
$\delta( )$	virtual change, Eq. (85)
η	dimensionless spanwise station, Eq. (93)
κ	stiffness, ft-lb, Eq. (19)
μ	advance ratio, $\mu = V/\Omega R$
μ_T	auxiliary moment function, Eq. (36)
ν	velocity ratio, Eq. (98)
ξ	aerodynamic damping in pitch, ft-lb, Eq. (28)
$\Pi_{\alpha 2}$	two-dimensional aerodynamic damping parameter in pitch, Eq. (34)

$\Pi_{\alpha 3}$	three-dimensional aerodynamic damping parameter in pitch, Eq. (41)
ρ	air density, lb-sec^2/ft^4
σ	rotor solidity
σ_T	stalling angle parameter, Eq. (66)
ϕ	phase angle, deg or rad
ψ	azimuth angle, deg or rad
ψ_{SF}	total unstable stall flutter azimuth range
ω	oscillatory frequency in pitch, rad/sec, Eq. (1)
Ω	rotor rotational speed, rad/sec

SUBSCRIPTS

h	due to translation (used in References 8 and 13 coefficients)
I	imaginary part
L	lift
M	moment or mean
0	root value
P	due to pitch (used in Reference 1 coefficients)
R	real part
T	due to translation (used in Reference 1 coefficients), or tip value
TOT	total
U	unsteady
α	due to pitch
2	two-dimensional
3	three-dimensional

SUPERSCRIPTS

$( )^*$	complex
$\bar{(\ )}$	amplitude
$\dot{(\ )}, \ddot{(\ )}$	first and second derivatives with respect to time
$( )'$	per unit span
$( )^H$	quantities taken from Reference 1

BLANK PAGE

INTRODUCTION

Recently, as a result of the combined requirements of higher forward speeds and greater blade loadings for helicopters, there has been a renewed interest in the study of stall-induced oscillatory blade instabilities, with particular emphasis on the effects of these extreme requirements on the stall flutter phenomenon. This is evidenced by the work reported in References 2, 3, and 4, to name only a few. However, with the exception of Reference 2, all of these studies had one major deficiency in common — a dearth of valid, unsteady aerodynamic data encompassing a substantial portion of the stall flow regime. In fact, even in Reference 2 the data were synthesized and idealized from a number of sources.

These increased performance requirements were foreseen some time ago, and Sikorsky Aircraft obtained a large quantity of two-dimensional unsteady aerodynamic test data from an isolated NACA 0012 airfoil section, which was oscillated in pitch about its 25% chord. These data are utilized in the stall flutter stability analysis described in this volume.

Similar data were obtained from Reference 1. These data were converted to a form comparable with the Sikorsky data and were used in a similar stability analysis. The two sets of results showed good qualitative agreement.

The stall flutter stability analysis was used to provide stall flutter boundaries for a typical rotor. The boundaries indicate flight conditions for which stall flutter may be particularly troublesome.

DESCRIPTION OF TEST EQUIPMENT, MODEL INSTALLATION, AND PROCEDURE

TEST EQUIPMENT AND MODEL

The experimental program was conducted in the two-dimensional channel of the UAC 8-foot main wind tunnel, which has an atmospheric, single-return, closed-throat circuit with an octagonal throat. Test section Mach number is variable below M = 1.0, and the Reynolds number for the 2-foot chord model used in the test program was approximately $R_c = 1.4\ M \times 10^7$. Figure 1 shows schematically the mechanical system used in the dynamic tests to obtain unsteady aerodynamic data for the oscillating airfoil.

The NACA 0012 model tested during this program consisted of a balsa wood core supported by chordwise aluminum stiffeners and wrapped in three layers of fiber glass. The model, which had a span of 33 inches and a chord of 24.5 inches, is shown in Figure 2. Thirteen pairs of differential pressure orifices were located on the top and bottom of the model along a chordwise line which was 11.5 inches inboard from the tip. The orifices were connected with internal tubing to 13 miniature differential pressure pickups of the variable reluctance type which were enclosed in a cavity in the model tip. In this manner, pressure acting on the airfoil surface at a given chordwise station was converted to an electrical signal which was transmitted to a recording oscillograph. Representative oscillograph traces of the pressure transducer signals are presented in Figure 3. In addition, a linear transformer was attached to the end of the shaft, and its output was used to record variations in angle of attack.

TEST PROCEDURE

In general, the following test procedure was employed. A set of eccentric cams was installed which fixed the amplitude of motion, $\bar{\alpha}$. After a preliminary shake test, all recording instruments were zeroed and the tunnel was started and brought up to its operating Mach number M . At the prescribed Mach number, the mean angle of attack, α_M , was varied over a range of values, and for each value of α_M the frequency, f , was varied over a range of values. After data had been recorded at all of the desired combinations of α_M and f , the Mach number was changed and records were taken for a new set of values of α_M and f . Finally, after all desired values of M had been obtained, the cams were changed to obtain a new value of $\bar{\alpha}$ and the entire process was repeated.

The oscillograph records of the steady and unsteady pressure response were taken for most combinations of the following parameter values:

Amplitude of motion, $\bar{\alpha} = \pm 4, 6, 8$ deg

Mach number, $M = 0.2, 0.3, 0.4$

Mean angle of attack, α_M = 0 to 33 deg in 3-deg increments

Frequency, $f = 0.0, 0.5, 1, 2, 4, 8, 12, 16$ cps

In the interest of expediency or safety, certain combinations were omitted. For example, it was decided to limit the maximum frequency to 12 cps for mean angles of attack greater than 24 degrees to ensure the structural integrity of the system, particularly at the higher Mach numbers.

TEST RESULTS

DATA REDUCTION

The oscillograph records were read, and the measured data were tabulated. A digital computer was then used to reduce these data to obtain, for each run, the chordwise differential pressure distribution as well as normal force and moment as functions of instantaneous angle of attack. The magnitude of the corrections to the measured pressures for the influence of tunnel wall constraint under steady-state conditions was estimated to be less than 3% of the full-scale values in the linear range; therefore, no corrections to the data were made. The unsteady wall interference effects were small compared to the gross unsteady parameters being measured and were also neglected (Reference 5).

PRESSURE DISTRIBUTIONS

The output of each pressure transducer was directly proportional to the local, instantaneous pressure difference,

$$\Delta p^*(x,t) = \Delta \bar{p}^*(x) e^{i\omega t} = p^*_{upper} - p^*_{lower} \tag{1}$$

where the asterisk denotes a complex quantity and the superscript bar denotes an amplitude function. The pressure difference amplitude $\Delta \bar{p}^*$ is expressed as a complex number,

$$\Delta \bar{p}^* = \Delta \bar{p}_R + i \Delta \bar{p}_I \tag{2}$$

to account for possible phase differences between the local pressure response and the motion. As shown in Figure 3, the peak-to-peak difference in the oscillograph trace was proportional to the absolute magnitude of the complex pressure difference given in Eq. (2),

$$\left| \Delta \bar{p} \right| = \sqrt{\Delta \bar{p}_R^{\,2} + \Delta \bar{p}_I^{\,2}} \tag{3}$$

Some representative results of these measurements are shown in Figures 4 and 5, in which the absolute magnitude of the pressure difference from Eq. (3) has been divided by the dynamic pressure,

$$q = \frac{1}{2} \rho U^2 \tag{4}$$

and the resulting pressure coefficient, $|\Delta\bar{p}/q|$, has been plotted as a function of dimensionless chordal station. In Figure 4, the experimentally determined values of this dimensionless amplitude of the differential pressure coefficient are presented for a range of mean angles of attack (α_M = 0 to 32 degrees in 3-degree increments) at a fixed frequency of 4 cps. In Figure 5, a similar set of results is presented for a range of frequencies (f = 4, 8, 12, 16 cps) for a given set of mean angles of attack (α_M = 0, 3, 6, 9 degrees). In both figures, the solid curve represents the pressure coefficient predicted from classical unsteady potential flow theory. In the present case the theoretical pressure distribution formula was obtained from Reference 6, which is based on the fundamental work of Theodorsen (Reference 7). The pitching results in Reference 6 have been derived for a pivot axis at the 25% chord; for convenience, the real and imaginary parts are reproduced below, with the notation revised slightly to conform to present usage.

$$\left(\frac{\Delta\bar{p}}{q}\right)_R = -4\bar{a}k^2\left[-\frac{1+x}{2}\sqrt{1-x^2} + \left(\frac{F}{k^2} - \frac{G}{k}\right)\sqrt{\frac{1-x}{1+x}}\right] \tag{5}$$

$$\left(\frac{\Delta\bar{p}}{q}\right)_I = -4\bar{a}k^2\left[\frac{1}{k}\sqrt{1-x^2} + \frac{1}{k}\left(\frac{G}{k} + F + \frac{1}{2} + x\right)\sqrt{\frac{1-x}{1+x}}\right] \tag{6}$$

In these formulas, x is the dimensionless chordwise position relative to the midchord; in semichords, and k is the reduced frequency parameter,

$$k = \frac{b\omega}{U} \tag{7}$$

and F and G are the real and imaginary parts, respectively, of the Theodorsen circulation function, $C(k) = F(k) + iG(k)$.

It is seen, from Figure 4, that at low to moderate incidence angles, the experimental values are in good agreement with theory; even at high incidence angles, the leading-edge peak is still maintained, although the agreement between theory and experiment has deteriorated. Finally, at extremely high incidence angles, even the leading-edge experimental values no longer agree with theory. The effects of increasing frequency at low incidence angle are shown in Figure 5, and it is seen that in all four parts of this figure the agreement between theory and experiment is excellent.

NORMAL FORCE AND MOMENT AMPLITUDE

On pages 394 and 395 of Reference 8 are found the equations for normal force and moment about the pivot axis in terms of the pressure distributions,

$$N^* = b\int_{-1}^{1}\Delta p^*(x)\,dx \tag{8}$$

$$M^* = b^2\int_{-1}^{1}(x-a)\Delta p^*(x)\,dx \tag{9}$$

or, in coefficient form,

$$C_N^* = \frac{N^*}{q(2b)} = \frac{1}{2}\int_{-1}^{1}\frac{\Delta p^*(x)}{q}\,dx \tag{10}$$

$$C_M^* = \frac{M^*}{q(2b)^2} = \frac{1}{4}\int_{-1}^{1}(x-a)\,\frac{\Delta p^*(x)}{q}\,dx \tag{11}$$

Pressure data obtained during the experimental program were reduced to coefficient form by use of Eqs. (10) and (11). The results of these integrations form the basis for the stability analysis to follow. However, before proceeding with this analysis, consideration will be given to Figure 6 in which the amplitudes of C_N^* and C_M^* have been plotted versus reduced frequency, k, over a small range of mean angles of attack. Included in both of these figures are the theoretical variations of these functions as predicted by the potential flow analysis (Reference 7). The analytical expressions used here may be obtained from Reference 8, and the explicit relationships for unsteady moment coefficient will be considered in great detail in a subsequent section of this volume. For the moment, though, it is sufficient to note that the general trends of the experimental data are in good agreement with the theory for mean incidence angles up to $\alpha_M = 9$ degrees; in fact, the data for zero mean incidence angle are in excellent agreement with theory.

NORMAL FORCE AND MOMENT HYSTERESIS LOOPS

When the instantaneous normal force or moment coefficient is plotted versus angle of attack, the resulting closed curve surrounds an area which, in the case of the moment, is representative of the energy absorbed or dissipated. This is found to be the case in both classical and separated flows. Consider the case depicted in Figure 7. The two upper curves represent hypothetical sinusoidal variations of angle of attack and either normal force or moment, both expressed in arbitrary units, as a function of time. In the example shown, the normal force or moment leads the angle of attack by one-eighth of a cycle or 15 degrees in phase. In the bottom portion of

the figure, the time variable has been eliminated and the normal force or moment has been plotted directly as a function of angle of attack. The arrows denote the direction of increasing time. This figure shows that a phase shift between force or moment and motion produces a loop which encloses a finite area. The same effect will be found to exist in the case of a nonsinusoidal force-motion-time relationship caused by the presence of separated flow. In classical or potential flow, the closed contour will be elliptical; whereas in separated flow, the contour will be distorted.

Normal Force Loops

A few representative unsteady normal force coefficient loops are presented in Figure 8 for a constant amplitude of $\bar{\alpha}$ = 6 degrees and a constant Mach number of M = 0.3. In this figure the experimentally determined unsteady normal force coefficients are plotted versus instantaneous incidence angle, with the superimposed arrowheads indicating the direction of increasing time. The solid lines represent the unsteady data, and the dashed lines represent the steady-state characteristics (also obtained from pressure readings in this test). The arrows indicate the direction of increasing time. Three of the inset figures were for a constant frequency of 4 cps and serve to show the effects of varying mean incidence angle, from α_M = 6 to 12 to 18 degrees. The two right-hand inset figures are both for a mean incidence angle of α_M = 12 degrees and illustrate the effect of a change in frequency from 4 cps to 16 cps. It is clear that the increase in mean incidence angle to values greater than the steady-state stall angle has a rather profound effect on the dynamic force response of the oscillating airfoil. It is also clear that an increase in frequency produces a radical change in the dynamic stalling behavior of the airfoil. Specifically, at low frequency the dynamic force response reaches its peak value just before the maximum incidence angle is reached; it then drops precipitously to a value far below the steady-state stall value and remains there for almost the entire region of decreasing incidence. In contrast to this behavior, the effect of high frequency is to maintain a nearly elliptical response loop, even for incidence angles beyond stall, over the entire range of instantaneous incidence angle. The further significance of this behavior will be explored at length below and in subsequent sections in connection with the moment coefficient loops and their stability implications.

Moment Loops

Some representative unsteady moment coefficient loops are presented in Figures 9 through 11. These loops are the basis for the stability analysis which follows; hence, they are shown in greater detail than the normal force loops. In these figures, an effort has been made to illustrate the variations in the moment hysteresis loops for each of the variable test parameters. Thus, the effect of varying mean incidence angle, α_M, is shown in Figure 9; the effect of varying frequency, f, is shown in Figure 10; and the effect of varying Mach number, M, and torsional amplitude, $\bar{\alpha}$, is shown in Figure 11. In all of these figures, the superimposed arrowheads indicate the direction of increasing time.

Figure 9 illustrates the variation in moment coefficient with incidence angle at the fixed conditions $M = 0.2$, $\tilde{\alpha} = 6$ degrees and $f = 4$ cps. The solid curves are associated with the unsteady motion presently under consideration, and the dashed curve represents the steady-state moment (from balance data) for the same Mach number and Reynolds number. (Once again, the arrows indicate the direction of increasing time.) It can be seen that all three moment loops generally follow the steady-state curve, and it will be shown presently in Figure 10 that the loop for $\alpha_M = 0$ degrees is in good agreement with the results obtained from potential flow theory. (This is also evidenced by the proximity of the data point for $\alpha_M = 0$ degrees to the theoretical curve in Figure 6 for a reduced frequency value of $k = 0.112$.) The character of the hysteresis loop changes radically as α_M increases, and the moment loop for $\alpha_M = 12$ degrees displays the characteristic crossover behavior of the unsteady moment in the neighborhood of the stalling angle. This separation-induced distortion of the moment hysteresis loop has been the subject of a number of early investigations, including those reported in References 1 and 9 and, hence, will not be discussed at length herein. However, it will be shown later in this report that the system stability is strongly dependent on the direction in which the area of the moment loop is enclosed; in particular, it will be shown that a counterclockwise enclosure is stable, whereas a clockwise enclosure is unstable. Thus, it is seen that in some mean incidence range containing $\alpha_M = 12$ degrees, there may be some potentially unstable regions which could affect the stability of rotor systems. Finally, for a mean incidence angle of 24 degrees, the moment loop once again implies a stable motion.

Figure 10 shows the effects of increasing the frequency from 4 cps to 16 cps for two mean angles of incidence. Also in Figure 10, the experimental results are shown as solid curves, and the results from unsteady potential flow theory are shown as dashed curves. (A brief discussion of these theoretical predictions is presented later in this volume in Appendix I). It is seen that except for a slight upward displacement of the experimental results relative to the theoretical curves, the two are in excellent agreement. The right side of this figure shows that for $\alpha_M = 15$ degrees, the effect of an increase in frequency (and, hence, an increase in reduced frequency) appears to be stabilizing, even though the incidence angle is considerably greater than the stalling angle over much of the range. This is in accord with the implied results in References 10 and 17, as pointed out and further amplified by Reference 1, and also as reported in Reference 12. However, in the left column of Figure 11, it appears that an increase in reduced frequency (caused by a decrease in Mach number at constant frequency, $f = 4$ cps) yields a contradictory result in that the stable closed loops for $k = 0.056$ and 0.075 are replaced by a marginally stable crossed loop for $k = 0.112$. It is believed that this behavior is characteristic of very small values of k, and it will be seen later in this volume that all of these results are self-consistent. Finally, the right column of Figure 11 shows the effect of increasing the torsional amplitude. Superimposed on each curve in Figure 11 is the steady-state moment variation, represented by the dashed line. Once again, the results appear to be self-consistent.

This concludes the review of the original test program. In the next section, the analytical expressions necessary for the stability investigation will be developed; following this, the application of this analysis to the data will be discussed. The last section of the report will deal with the stability characteristics of a typical rotor under various loading conditions.

ANALYSIS

TWO-DIMENSIONAL WORK PER CYCLE

The differential work done by the aerodynamic moment during the course of the torsional motion is obtained by computing the product of the in-phase components of moment and differential twist, or

$$dW = M_R \, d\alpha_R \tag{12}$$

where M_R and α_R are the real parts of these quantities. Hence, the work per cycle of motion is obtained by integrating Eq. (12) over one cycle, or

$$W = \oint M_R \, d\alpha_R \tag{13}$$

This may be rendered dimensionless by dividing both sides of the equation by $\frac{1}{2}\rho U^2 (2b)^2$, which yields the equation for the work coefficient in terms of the integral of the moment coefficient, as follows:

$$C_W = \frac{W}{\frac{1}{2}\rho U^2 (2b)^2} = \oint C_{M_R} \, d\alpha_R \tag{14}$$

To evaluate the integral in Eq. (14), it is necessary to introduce the quantities C_{M_R} and $d\alpha_R$. The derivation of these functions is presented in Appendix I, which has been included in the present volume for completeness. From Eq. (74), after expanding the exponential function in sines and cosines, the real part of the moment coefficient may be obtained in the form

$$C_{M_R} = C_{M_M} + \bar{C}_{M_{UR}} \cos \omega t - \bar{C}_{M_{UI}} \sin \omega t \tag{15}$$

The differential of Eq. (80) is

$$d\alpha_R = -\bar{\alpha} \sin \omega t \; d(\omega t) \tag{16}$$

and after Eqs. (15) and (16) are substituted into Eq. (14), the result is

$$C_W = -\int_0^{2\pi} \left[C_{M_M} + \bar{C}_{M_{UR}} \cos\omega t - \bar{C}_{M_{UI}} \sin\omega t \right] \bar{\alpha} \sin\omega t \; d(\omega t) \qquad (17)$$

(The integration range, $0 \leq \omega \leq 2\pi$, is equivalent to one complete cycle of motion.) After the integrations indicated in Eq. (17) are performed, it is found that the term involving the mean moment vanishes as well as the term containing the real part of the unsteady moment; the final result for the theoretical work coefficient is given by

$$C_W = \pi \bar{\alpha} \bar{C}_{M_{UI}} \qquad (18)$$

This is the work done by the air on the airfoil; hence, a positive value of C_W will indicate an unstable motion, since this implies a net energy exchange from the surrounding medium to the airfoil, whereas a negative value of C_W will indicate a stable, or damped motion.

TWO-AND THREE-DIMENSIONAL AERODYNAMIC DAMPING

Before proceeding with the analysis of the aerodynamic damping of the system, it is useful to review briefly the behavior of a linear, damped, torsional system such as the one described by the differential equation

$$I \ddot{\alpha}^* + C \dot{\alpha}^* + \kappa \alpha^* = 0 \qquad (19)$$

where I is the inertia, C is the damping, and κ is the stiffness of the system. If the motion is essentially sinusoidal (i.e., only slightly damped and, hence very nearly a constant amplitude sinusoid) then Eq. (69) of Appendix I is a solution. The equation becomes

$$(-\omega^2 I + i\omega c + \kappa)\, \bar{\alpha} = 0 \qquad (20)$$

It is seen that the damping coefficient is contained in the imaginary part of this expression, and it may be assumed that the equivalent damping terms for any similar linear system will also be contained in the imaginary part of the differential equation solution.

Eq. (19) represents a system oscillating in torsion in a vacuum. If the same system were to oscillate in torsion in a moving airstream, the right-hand side of the equation would no longer be zero but would represent the unsteady moment imposed by the moving air on the body, or

$$I\ddot{\alpha}^* + C\dot{\alpha}^* + \kappa\alpha^* = M_U^* \qquad (21)$$

It is shown in References 8 and 13 that in the case of a single-degree-of-freedom torsional oscillation, the unsteady moment is a function of the torsional displacement and its first two time derivatives and may be expressed in the general form

$$M_U^* = M_1 \ddot{\alpha}^* + M_2^* \dot{\alpha}^* + M_3^* \alpha^* \tag{22}$$

In the results cited in References 8 and 13 for an isolated airfoil oscillating in an incompressible, potential flow (based on Theodorsen's theory, Reference 7), the component M_1 is a pure real quantity, whereas both M_2^* and M_3^* are complex; hence,

$$\begin{aligned} M_2^* &= M_{2R} + iM_{2I} \\ M_3^* &= M_{3R} + iM_{3I} \end{aligned} \tag{23}$$

After Eqs. (22) and (23) are substituted into Eq. (21) and the terms are rearranged slightly, the result is

$$\left(I - M_1\right)\ddot{\alpha}^* + \left(C - M_{2R} - iM_{2I}\right)\dot{\alpha}^* + \left(\kappa - M_{3R} - iM_{3I}\right)\alpha^* = 0 \tag{24}$$

Once again, if the damping is sufficiently small, the motion will be nearly sinusoidal and Eq. (69) represents a solution, whereupon Eq. (24) becomes

$$\left[-\omega^2\left(I - M_1\right) + i\omega\left(C - M_{2R} - iM_{2I}\right) + \left(\kappa - M_{3R} - iM_{3I}\right)\right]\bar{\alpha} = 0 \tag{25}$$

After collecting real and imaginary parts,

$$\left[\left\{-\omega^2\left(I - M_1\right) + \omega M_{2I} + \kappa - M_{3R}\right\} + i\left\{\omega\left(C - M_{2R}\right) - M_{3I}\right\}\right]\bar{\alpha} = 0 \tag{26}$$

As in the case of the system oscillating in vacuum, the imaginary part of Eq. (26) will represent the total damping of the system, as follows:

$$\text{total damping} = \omega\left(C - M_{2R}\right) - M_{3I} \tag{27}$$

Since the quantity ωC constitutes the system damping in the absence of a moving airstream, then the remainder of Eq. (27) must be the effective aerodynamic damping of the system, as follows:

$$\xi = -\omega M_{2R} - M_{3I} \tag{28}$$

The symbol ξ denotes the (dimensional) aerodynamic damping parameter of a system executing a single-degree-of-freedom torsional motion. Return now to Eq. (22). It will be assumed that the left-hand side of this equation is a time dependent, sinusoidal function having the form

$$M_U^* = \bar{M}_U^* e^{i\omega t} \tag{29}$$

where

$$\bar{M}_U^* = \bar{M}_{UR} + i\bar{M}_{UI}$$

After Eqs. (29), (30), and (69) are substituted into Eq. (22) and the exponential factor $e^{i\omega t}$ is cancelled, the result is

$$\bar{M}_{UR} + i\bar{M}_{UI} = \left[\left\{-\omega^2 M_1 - \omega M_{2I} + M_{3R}\right\} + i\left\{\omega M_{2R} + M_{3I}\right\}\right]\bar{\alpha} \tag{31}$$

When real and imaginary parts are equated, it is seen that

$$\bar{M}_{UI} = \left[\omega M_{2R} + M_{3I}\right]\bar{\alpha} \tag{32}$$

A comparison of Eqs. (28) and (32) shows that the aerodynamic damping parameter, ξ, is equal to the negative of the derivative of the imaginary component of the unsteady moment with respect to the amplitude of motion,

$$\xi = -\frac{d\bar{M}_{UI}}{d\bar{\alpha}} = -\left[\omega M_{2R} + M_{3I}\right] \tag{33}$$

It is convenient at this point to rewrite Eq. (33) in dimensionless coefficient form, as previously done in Eq. (14). Hence, after defining the dimensionless two-dimensional aerodynamic damping parameter in pitch by the symbol

$$\Xi_{\alpha_2} = \frac{\xi}{(1/2)\rho U^2 (2b)^2} \tag{34}$$

then Eq. (33) may be rewritten as

$$\Xi_{\alpha 2} = -\frac{d\bar{C}_{M_{UI}}}{d\bar{\alpha}} = -\frac{\omega M_{2R} + M_{3I}}{(1/2)\rho U^2 (2b)^2} \tag{35}$$

In the ultimate formulation to be obtained herein, it will be useful to express the aerodynamic damping parameter in terms of the work per cycle of motion, since the latter is a quantity which is most easily measured from the available test data. To accomplish this, a few manipulations are necessary. First, Eq. (76) of Appendix I will be rewritten in the form

$$\bar{C}_{M_{UI}} = \mu_T(k,a)\bar{\alpha} \tag{36}$$

where

$$\mu_T(k,a) = \frac{\pi k^2}{2}\left[M_{\alpha_I} - (L_{\alpha_I} + M_{h_I})(\tfrac{1}{2} + a) + L_{h_I}(\tfrac{1}{2} + a)^2\right] \tag{37}$$

is a function of k and a only. Now, substitute Eq. (36) into Eq. (18) to obtain

$$C_W = \pi \mu_T \bar{\alpha}^2 \tag{38}$$

and next substitute Eq. (36) into the derivative of Eq. (35) with the result

$$\Xi_{\alpha_2} = -\frac{\partial \bar{C}_{M_{UI}}}{\partial \bar{\alpha}} = -\mu_T \tag{39}$$

Finally, after solving Eq. (38) for μ_T, substitution into Eq. (39) yields the useful formula

$$\Xi_{\alpha_2} = -\frac{C_W}{\pi \bar{\alpha}^2} \tag{40}$$

Ultimately, these two-dimensional data must be used in the stability evaluation of the three-dimensional rotor system; hence, they must be converted to three-dimensional aerodynamic damping form. This has been done in Appendix II.

$$\Xi_{\alpha_3} = \int_0^1 \Xi_{\alpha_2}\, \nu^2(\eta)\, f_\alpha^2(\eta)\, d\eta \tag{41}$$

where $\nu(\eta)$ is the spanwise velocity ratio, $f_\alpha(\eta)$ is the spanwise mode shape distribution, and η is the dimensionless spanwise variable.

SPECIALIZATION TO 25% CHORD PIVOT AXIS

Most of the analytical development in the preceding sections of this volume has been derived for an arbitrary location of the pivot axis. The experimental data to be used in the stability analysis were obtained on an airfoil pivoted about its 25% chord and the rotor blade to be analyzed below will also have its effective pivot axis at or very near the 25% chord (assuming a conventionally designed blade system). It will be useful, then, to convert the results of the previous sections for the special case of 25% chord pivot axis location, in anticipation of the need for these specialized formulas in subsequent sections.

It was stated earlier that for a 25% chord pivot location $a = -1/2$, and hence, the factor $1/2 + a = 0$. When this is substituted into Eq. (76) of Appendix I the result for the imaginary part of the unsteady moment coefficient amplitude becomes

$$\bar{C}_{M_{UI}} = -\frac{\pi k^2}{2} M_{\alpha I} \bar{\alpha} \tag{42}$$

and substitution into Eq. (18) yields

$$C_W = \frac{\pi^2 k^2}{2} M_{\alpha I} \bar{\alpha}^2 \tag{43}$$

for the work coefficient. Similarly, Eq. (40) becomes

$$\Xi_{\alpha 2} = -\frac{\pi k^2}{2} M_{\alpha I} \tag{44}$$

for the two-dimensional damping coefficient. In the case of an incompressible, potential flow past the airfoil, the imaginary part of Eq. (84) will be substituted from Appendix I for $M_{\alpha I}$. Eqs. (42), (43) and (44) then become

$$\bar{C}_{M_{UI}} = -\frac{1}{2} \pi k \bar{\alpha} \tag{45}$$

$$C_W = -\frac{1}{2} \pi^2 k \bar{\alpha}^2 \tag{46}$$

and

$$\Xi_{\alpha 2} = \frac{\pi k}{2} \tag{47}$$

Eq. (46) shows that for these ideal conditions, the work coefficient will always be negative (i.e., the system will always be stable), and is directly dependent on both k and $\bar{\alpha}$. Similarly, Eq. (47) shows that the aerodynamic damping is always positive and is independent of amplitude.

TWO-DIMENSIONAL STABILITY CALCULATIONS

FINAL DATA REDUCTION

In the course of the original test program, approximately 550 test points were taken; for each of these a C_M-α loop was generated. Figures 9, 10, and 11 contain fourteen separate examples of these loops. In principle, Eq. (14) was used to evaluate the work coefficient for each of these loops; however, a planimeter was used to obtain the actual area. Each loop was planimetered at least three times, and an average of these three measurements was used to represent the area of a given loop. (The maximum error incurred by this averaging procedure is estimated to be less than 3%). Appropriate conversion factors were used to transform the raw area data into work coefficient form, and Eq. (40) was then used to convert these work coefficients into two-dimensional damping parameter form.

The results of these calculations are presented in Tables I through III. The gaps in these tables denote values of frequency and/or mean incidence angle at which either no data were taken or no data were reduced. For example, only a limited amount of very low frequency data was taken, and these points were restricted to mean incidence angles of $\alpha_M = 12$ degrees and greater. Also, as Mach number was increased, some of the higher frequency and higher incidence angle runs were omitted. Occasionally, a double entry was made in the tables for a particular combination of f and α_M. This occurred whenever a C_M-α loop failed to close on itself. For example, in Table I, for $\bar{\alpha} = 6$ degrees at the point $\alpha_M = 3$ degrees and $f = 4$ cps ($k = 0.1125$) there are two values. The loop for this case does not return along the same path after one cycle of motion. In this case, as in other similar cases, an estimate was made of the two most likely loops, the areas of both were taken, and both numbers were entered in the appropriate table.

A representative group of these reduced damping parameter values is shown in Figures 12 and 13. These results were plotted directly from the second subtable of Table I. This pair of figures shows the variation of $\Xi_{\alpha 2}$ with reduced frequency k for the entire range of mean incidence angles. Included in each plot is the predicted theoretical variation of $\Xi_{\alpha 2}$ with k, taken from Eq. (47) for 25% chord pivot. It is seen from Figure 12 that the experimental values are in good agreement with theory for $\alpha_M = 0$, 3, 6, and 9 degrees. However, the data show considerable departure from the theory for incidence angles of $\alpha_M = 12$ degrees and above; in fact, there is a range of incidence angles, $12 \leq \alpha_M \leq 21$ degrees, in which the aerodynamic damping is negative (indicating an instability) over some portion of the k range. Finally, at extremely large values of incidence angle, $\alpha_M \geq 24$ degrees, the values of $\Xi_{\alpha 2}$ become positive once again and seem to approach the theoretical prediction at the highest incidence angles shown here.

There are innumerable ways of presenting the entire mass of data contained in Tables I through III. One obvious method is to go through each subtable, plotting the results in an analogous fashion to the results shown in Figures 12 and 13, with each set representing a specific combination of Mach number and torsional amplitude. This procedure is unwieldy in the ultimate application of the data, which is to determine the stability characteristics of helicopter rotor blades. Therefore, an effort has been made to reduce the number of independent parameters by combining these data sets in various ways.

The method to reduce the number of independent parameters which was chosen for this program utilized the grouping of data as presented in Tables I through III. Specifically, all of the data for M = 0.2 were combined, and an effort was made to eliminate $\bar{\alpha}$ as a parameter. Similarly, the data for M = 0.3 and for M = 0.4 were also treated separately. The elimination of $\bar{\alpha}$ as a parameter was effected by plotting the variation of $\Xi_{\alpha 2}$ with k for each mean incidence angle and by including data for all three values of the amplitude. This decision to eliminate $\bar{\alpha}$ was based in part on the fact that the theoretical result presented in Eq. (47) for χ_2 is independent of $\bar{\alpha}$.

After all of the data had been plotted in this fashion ($\Xi_{\alpha 2}$ versus k for each α_M , for each M , with the data for all values of $\bar{\alpha}$ on each plot), a set of curves was faired through the data for each set of parameter values. A tabulation of the coordinates of the faired curves was then made for a large number of conveniently spaced values of k at the given values of α_M , and a set of cross plots of $\Xi_{\alpha 2}$ versus α_M was made using these tabulated values. Once again, a set of curves was faired through the data, and the coordinates were tabulated, this time for a closer spacing of incidence angles than were previously available (every degree instead of every 3 degrees). This process was repeated sufficiently often to reduce the scatter of the coordinates of the faired curves to a negligible amount; in effect, a graphical iteration process was employed to smooth the data. (The reason for adopting this procedure was to provide a smoothed set of unsteady aerodynamic data suitable for bivariant interpolation on a high-speed digital computer.) The results of this process are presented in Tables IV, V, and VI for Mach numbers M = 0.2, 0.3, and 0.4, respectively.

A comparison of the original data and the final smoothed data is shown in Figures 14, 15, and 16. These figures contain almost all of the aerodynamic damping data for M = 0.2 which were originally obtained from the $C_M - \alpha$ loops and were presented in Table I. The faired curves were taken from Table IV. Similar plots could be constructed for M = 0.3 and 0.4 from the original data in Tables II and III and the smoothed data in Tables V and VI. However, in the interest of brevity, they are not included here.

A number of conclusions may be reached by studying the results presented in these figures, as enumerated below. It is seen from Figure 14 that the experimental results are generally in good agreement with the theory at low mean incidence angle ($\alpha_M \leq 9$ deg) for all amplitudes. As the mean incidence angle is increased to values greater than $\alpha_M = 12$ degrees, the

aerodynamic damping is seen to depart from the theory and, in some cases, to become negative over some range of k. A study of Figures 14 and 15 is quite instructive in explaining the apparent contradiction noted earlier in the behavior of $\Xi_{\alpha 2}$ with increasing k. In these figures, it is seen that for sufficiently large k, an initially unstable or marginally stable condition will become more stable as k is increased, as stated earlier in this report. However, at very low values of k, the aerodynamic damping initially increases from a zero value at $k = 0$ and reaches a small positive value before becoming negative at a higher value of k. This was pointed out earlier in connection with the behavior of the loops in Figure 11. Finally, as shown in Figure 15 for sufficiently large values of α_M, the system once again exhibits a stable behavior.

A similar behavior in the variation of $\Xi_{\alpha 2}$ with α_M is seen to exist for intermediate values of k (Figure 16). This figure shows the aerodynamic damping to be initially stable at low incidence angle, unstable in the approximate range of 12 degrees $< \alpha_M <$ 22 degrees, and then stable once again. Thus, there appears to be a "pocket" of instability surrounded by stable regions at both higher and lower incidence angles, and at lower values of reduced frequency.

This isolated region of instability is graphically illustrated in Figures 17, 18, and 19. In these figures, the aerodynamic damping is represented as a surface relative to the k, α_M-plane for Mach numbers of M = 0.2, 0.3, and 0.4. These aerodynamic damping surfaces are presented in both an isometric view and a near planform view in each figure. The superimposed rectangular grid lines on each surface represent constant values of either k or α_M, and the dark-colored region lying below the k, α_M-plane is a region of negative aerodynamic damping and, hence, represents a potentially unstable aerodynamic condition.

CONVERSION OF REFERENCE 1 DATA

A number of years ago, an extensive experimental program was carried out as reported in Reference 1 to determine the variations in lift and moment coefficient on a 12% thick airfoil oscillating in both pitch and translation over a wide range of incidence angles. This work was limited in some respects by the restriction to low free-stream velocities and by the fact that the pivot axis for pitching motions was located at the 37% chord station ($a = -0.26$). However, the type of airfoil employed in the tests and the range of parameters over which experimental data were obtained make the Reference 1 results potentially quite useful in the present analysis. The remainder of this section is devoted to the transformation necessary to convert these coefficients to a form which can be compared directly with the results of the present analysis.

The experimental data tabulated in Reference 1 are presented in the form of an amplitude and phase angle for each component. Specifically, the quantities involved are C_{LT}, ϕ_{LT}, C_{LP}, ϕ_{LP}, C_{MT}, ϕ_{MT}, C_{MP}, ϕ_{MP}, where C represents the amplitude of the coefficient; ϕ, the phase angle by which the force or moment leads the motion; and the subscripts LT, LP, MT, MP, the lift due to translation, lift due to pitch,

moment due to translation, and moment due to pitch, respectively. It will be shown below that all four coefficients and their phase angles are needed to convert the Reference 1 data to a form comparable with the data presented in this volume. This is because the results given in Reference 1 were obtained for a 37% chord pivot axis, whereas the present report is concerned with a pivot axis at the 25% chord station. Other major differences between the Reference 1 and the present results involve the definitions of the coefficients and the fact that the measured unsteady coefficients of Reference 1 were not independent of the amplitudes of oscillation. These differences will be resolved in the course of the analysis.

In Reference 1 the lift and moment coefficients are defined by the equations

$$\bar{C}_{L_U}^{*H} = \frac{\bar{L}_U^*}{2\rho U^2 b} = C_{LT}^* + C_{LP}^* \tag{45}$$

and

$$\bar{C}_{M_U}^{*H} = \frac{\bar{M}_U^*}{2\rho U^2 b^2} = C_{MT}^* + C_{MP}^* \tag{49}$$

where, for example,

$$C_{LT}^* = C_{LT}(\cos\phi_{LT} + i\sin\phi_{LT}) \tag{50}$$

and where the superscript H in Eqs. (48) and (49) is used to denote the coefficient form employed in Reference 1. Eq. (48) and (49) may be solved for the unsteady lift and moment as

$$\bar{L}_U^* = 2\rho U^2 b\,(C_{LT}^* + C_{LP}^*) \tag{51}$$

$$\bar{M}_U^* = 2\rho U^2 b^2 (C_{MT}^* + C_{MP}^*) \tag{52}$$

Note that neither the dimensionless bending deflection amplitude $\bar{h} = h/b$ nor the twist deflection $\bar{\alpha}$ appears on the right side of these equations. As stated earlier, this is because the Reference 1 coefficients are not independent of the amplitudes of motion. The actual values of the parameters used in Reference 1 will be substituted into these equations later in the development.

The unsteady lift and moment amplitudes associated with both translation and pitch about a pivot axis at a may be taken from References 8 or 13.

$$\bar{L}_U^* = \pi\rho b^3\omega^2\left\{L_h\bar{h} + \left[L_\alpha - \left(\tfrac{1}{2}+a\right)L_h\right]\bar{\alpha}\right\} \tag{53}$$

$$\bar{M}_U^* = \pi\rho b^4\omega^2\left\{\left[M_h - \left(\tfrac{1}{2}+a\right)L_h\right]\bar{h} + \left[M_\alpha - \left(\tfrac{1}{2}+a\right)\left(L_\alpha + M_h\right) + \left(\tfrac{1}{2}+a\right)^2 L_h\right]\bar{\alpha}\right\} \tag{54}$$

A combination of Eqs. (51) and (53) and Eqs. (52) and (54) yields the relationships

$$L_h\bar{h} + \left[L_\alpha - \left(\tfrac{1}{2}+a\right)L_h\right]\bar{\alpha} = \frac{2}{\pi k^2}\left(C_{LT}^* + C_{LP}^*\right) \tag{55}$$

and

$$\left[M_h - \left(\tfrac{1}{2}+a\right)L_h\right]\bar{h} + \left[M_\alpha - \left(\tfrac{1}{2}+a\right)\left(L_\alpha + M_h\right) + \left(\tfrac{1}{2}+a\right)^2 L_h\right]\bar{\alpha} = \frac{2}{\pi k^2}\left(C_{MT}^* + C_{MP}^*\right) \tag{56}$$

After separating the motions into single-degree-of-freedom oscillations in bending and torsion, Eqs. (55) and (56) may be recast in an equivalent form as four equations, as follows:

$$L_h\bar{h} = \frac{2}{\pi k^2} C_{LT}^* \tag{57}$$

$$\left[L_\alpha - \left(\tfrac{1}{2}+a\right)L_h\right]\bar{\alpha} = \frac{2}{\pi k^2} C_{LP}^* \tag{58}$$

$$\left[M_h - \left(\tfrac{1}{2}+a\right)L_h\right]\bar{h} = \frac{2}{\pi k^2} C_{MT}^* \tag{59}$$

$$\left[M_\alpha - \left(\tfrac{1}{2}+a\right)\left(L_\alpha + M_h\right) + \left(\tfrac{1}{2}+a\right)^2 L_h\right]\bar{\alpha} = \frac{2}{\pi k^2} C_{MP}^* \tag{60}$$

These, in turn, may be solved for the standard coefficients L_h , L_α , M_h , M_α :

$$k^2 L_h = \frac{2}{\pi} \frac{C_{L_T}^*}{\bar{h}} \tag{61}$$

$$k^2 L_\alpha = \frac{2}{\pi} \left[\frac{C_{L_P}^*}{\bar{\alpha}} + \left(\frac{1}{2} + a \right) \frac{C_{L_T}^*}{\bar{h}} \right] \tag{62}$$

$$k^2 M_h = \frac{2}{\pi} \left[\frac{C_{M_T}^*}{\bar{h}} + \left(\frac{1}{2} + a \right) \frac{C_{L_T}^*}{\bar{h}} \right] \tag{63}$$

$$k^2 M_\alpha = \frac{2}{\pi} \left\{ \frac{C_{M_P}^*}{\bar{\alpha}} + \left(\frac{1}{2} + a \right) \frac{C_{L_P}^*}{\bar{\alpha}} + \left(\frac{1}{2} + a \right) \left[\frac{C_{M_T}^*}{\bar{h}} + \left(\frac{1}{2} + a \right) \frac{C_{L_T}^*}{\bar{h}} \right] \right\} \tag{64}$$

The quantities on the right side of Eqs. (61) through (64) represent the experimental values obtained in Reference 1. Numerical values must be inserted for the pivot axis location, $a = -0.26$, and for the dimensionless displacements, $\bar{h} = h/b = 0.9/5.808 = 0.155$, and $\bar{\alpha} = 6.08\,\pi/180 = 0.106$. The quantities found on the left sides of these equations will also represent the experimental values; however, these quantities will be independent of pivot axis location, at least according to the linear theory employed here.

To use the Reference 1 data in the present analysis, the imaginary part of Eq. (64) must be substituted into Eq. (44). After inserting the value $a = -0.26$, the result for the two-dimensional aerodynamic damping is

$$\Xi_{\alpha_2} = -\frac{1}{\bar{\alpha}} \left[C_{M_P} \sin \phi_{M_P} + 0.24\, C_{L_P} \sin \phi_{L_P} \right] - \frac{0.24}{\bar{h}} \left[C_{M_T} \sin \phi_{M_T} + 0.24\, C_{L_T} \sin \varphi_{L_T} \right] \tag{65}$$

This equation was used to evaluate $\Xi_{\alpha 2}$ from the Reference 1 coefficients after inserting the values $\bar{h} = 0.155$ and $\bar{\alpha} = 0.106$.

COMPARISON OF PRESENT RESULTS WITH REFERENCE 1 DATA

Before these results could be applied in the present stability analysis, some basis of comparison had to be established for the present data and the Reference 1 data, as described below. Three configurations were tested in Reference 1 --the blunt wing, the intermediate wing, and the sharp wing-- in which the profiles differed only in the vicinity of the leading edge. Since there is a slight difference in both the steady-state (i.e., stalling angle) and nonsteady behavior of these configurations, the data for each are presented separately in Reference 1 as functions of mean incidence angle, α_M , and reduced frequency, k . It was decided to correlate these results with one another and with the present data by means of a stall angle parameter,

$$\sigma_T = \alpha_M / \alpha_S \tag{66}$$

The angle α_S is the stalling angle for the particular configuration under consideration. This varied from configuration to configuration in Reference 1, in the present case it was taken to be $\alpha_S = 13$ degrees, which is the incidence angle at which the slope of the steady-state normal force curve becomes horizontal in Figure 8. This choice of a correlation parameter appeared to be a logical one in view of the strong effect the stall point has on unsteady response. It can be seen from Figure 16, for example, that the aerodynamic damping is nearly constant below the stalling angle and begins to vary only when the combination of mean incidence angle and amplitude of motion cause the airfoil to be affected by stalling effects.

As in the case of the present results, the Reference 1 data were bivariantly dependent on both α and k ; a graphical iteration scheme, similar to the method used on the present data, was employed to smooth these data. Equation (65) was then used to calculate the two-dimensional aerodynamic damping as a function, this time, of stall angle parameter, σ_T , and reduced frequency, k . These results are tabulated in Table VII.

A comparison of the two-dimensional aerodynamic damping results from the present data and from the Reference 1 data is presented in Figures 20 and 21. It is seen from these figures that the agreement between the two sets of data is quite good at low values of k , is excellent at intermediate values of k , and is qualitatively good at the highest value of k . Of particular significance is the fact that both sets of data predict essentially the same two-dimensional stability boundary at moderate values of k in the range $0.2 \leq k \leq 0.3$ and, in addition, predict the same damping level as a function of σ_T . Thus, it is seen that the pivot axis transformation procedure is valid, and the use of the stall angle parameter as the basis for correlation is also valid, at least within the variable ranges considered herein.

One further comparison of the two-dimensional aerodynamic damping parameter was made for the results of the present study and those of Reference 14. The aerodynamic damping curve for 25% chord pivot and $U/b\omega = 3.0$ (i.e., for $k = 0.333$) was taken from Figure 85 of Reference 14 (which, in turn, was obtained from a cross plot of previous results presented in Reference 12) and was compared with the curve for $M = 0.2$, $k = 0.3375$ from Figure 16 of this volume. A direct comparison was impossible to make since the airfoil section of Reference 12 was a thin (less than 0.04 thickness ratio) NACA 65-series profile which undoubtedly did not have the same stalling characteristics as the NACA 0012 airfoil used herein. Unfortunately, the static stall angle of this 65-series airfoil was not provided in Reference 12. Hence, to provide some sort of comparison of the Reference 14 results and the present results, it was necessary to improvise a basis of correlation. To this end, it was decided to scale the abscissa in Figure 14 of Reference 14 to force a coincidence of the first zero crossing of $\Pi_{\alpha 2}$ for the 25% chord pivot curve with the first zero crossing of the curve in Figure 16. This comparison is presented in Figure 22, in which the abscissa has been converted to stall angle parameter form.

It is obvious that this comparison can have only qualitative value, in view of the liberties taken with the scale of the abscissa values from Reference 14. Nevertheless, the comparison shows a general agreement between the two results, including the extent of the negative damping region and the recovery at higher values of σ_T, despite the large differences in the airfoil configurations and the test procedures employed.

ROTOR STABILITY CALCULATIONS

DESCRIPTION OF TYPICAL ROTOR CONFIGURATION

The Sikorsky S-61F rotor was chosen for the application of the stability analysis described in previous sections of this report. The rotor blade had a total chord of 1.521 feet and extended from a root radius of r_0 = 8.438 feet to a tip radius of r_T = 31.0 feet. Performance data for this configuration were calculated for four flight conditions: forward speed of 165 knots and 10,660 pounds gross weight, 165 knots and 12,460 pounds, 149 knots and 18,200 pounds, and 210 knots and 16,280 pounds. The tabulated data provided for each condition consisted of radial and azimuthal variations in incidence angle and Mach number.

It was assumed that the rotor blade was capable of responding to an infinitesimal disturbance in its fundamental torsional mode at every azimuth position, and the stability analysis was employed to determine the damping of this incipient vibration. The fundamental torsional frequency of the S-61F rotor blade is f = 27.3 cps or ω = 171.4 rad/sec; this quantity, together with the semichord dimension b = 0.76 feet, was used in Eq. (7) to calculate the numerator of the reduced frequency parameter, k. At each azimuthal station selected for the analysis, the radial variation in Mach number was converted to a comparable radial variation in velocity by multiplying each value by the assumed local speed of sound, 1100 ft/sec. This was used to calculate the radial variation in k which, together with the given radial variation in α, was used to interpolate the appropriate aerodynamic damping table for the required value of $\Xi_{\alpha 2}$ at each radial station. (Polar plots of typical k - and α - distributions over the rotor disc are shown in Figure 23.) The reference velocity, U_T, was chosen to be the tip value of the velocity at the zero azimuth station, $\psi = 0^\circ$, and it was used to compute the velocity ratio, $\nu(\eta)$, defined by Eq. (98) in Appendix II. The computed torsional mode shape function, $f_\alpha(\eta)$, was calculated for the S-61F helicopter rotor blade and is presented in Table VIII. With the introduction of these quantities into Eq. (41), the spanwise integral was calculated and the three-dimensional damping parameter, $\Xi_{\alpha 3}(\psi)$, was obtained for each value of azimuth angle.

STABILITY ANALYSIS

Three different procedures were employed in extracting information from the tables. In the first case, only the M = 0.2 table was used and the actual Mach number was used only to calculate U. If the value of either k or α exceeded the tabulated value in Table IV in a corner value of the damping parameter was used; i.e., the oversize parameter was artifically returned to the maximum tabulated value, and the interpolation with respect to the other parameter was performed.

A second case involved data for all three Mach numbers from Tables IV through VI. Here the actual Mach number was used to interpolate between tables as well as to provide values of the velocity, U. Corner values were also taken here; however, because of the truncation of the tables for the higher Mach numbers, this procedure led to somewhat unsatisfactory compromises.

The third case utilized the Reference 1 data presented in Table VII. Once again, the Mach number was used to calculate U only, as in the first case; and, once again, corner values were employed.

Stability analyses for the four flight conditions mentioned earlier were carried out by using each of these three options. The results are presented in Figures 24 and 25, in which the variation of the three-dimensional aerodynamic damping parameter, $\Xi \alpha_3$, with azimuth angle, ψ, is presented. In each figure the abscissa has been extended by 40 degrees beyond a full cycle to show more clearly the behavior of the damping in the region surrounding $\psi = 0$ degrees.

In Figure 24, for a flight speed of 165 knots and moderate gross weights, all three sets of data are in good agreement and predict a stable operation over all values of ψ. The results from the present data are somewhat more conservative than the Reference 1 results for the advancing blade region ($0° \leq \psi \leq 180°$), and all three inputs are in very close agreement over the retreating blade region ($180° \leq \psi \leq 360°$). As expected, the damping is greater in magnitude for $0° \leq \psi \leq 180°$ than it is for $180° \leq \psi \leq 360°$. This is because the dynamic pressure attains a maximum value in this region; hence, the square of the velocity ratio, which weights the integrand in Eq. (41) will also attain a maximum value.

In the upper portion of Figure 25 the flight speed has been reduced slightly, but the gross weight has experienced a significant increase, relative to the previous two figures. Once again, the results of the three damping-table options are in generally good agreement; and, once again, the Reference 1 data yield less conservative results than the present data in the range $0° \leq \psi \leq 180°$. It is seen that in the region of the retreating blade, the system damping decreases to very small values, which implies reduced flutter margin for the retreating blade.

Finally, in the lower portion of Figure 25, both flight speed and gross weight are considerably increased relative to the previous three cases. As shown in Figure 23, an extensive region of the rotor disc is simultaneously operating at large values of k and at incidence angles exceeding the steady-state stall angle ($\alpha_s = 13$ degrees). As a result, both the present data for $M = 0.2$ only and the Reference 1 data predict a region of large negative damping over the approximate range $340° \leq \psi \leq 366°$. This behavior will be considered in detail in a later section. (Note that the present data for $M = 0.2$ only also predict a shallow region of negative damping over the approximate range $233° \leq \psi \leq 251°$. This, too, will be studied in more detail later.) First, it should be noted that although the present data taken from all Mach numbers do not agree with the other two sources in predicting the instability for the retreating blade, they do agree elsewhere for the advancing blade. This disagreement is caused in part by the method adopted in the computer program in choosing the corner values. The corner values used in the case of free interpolation among Mach numbers are determined by the tabular value of M nearest to the actual local value of M. It is seen from Figures 18 and 19 that available damping information is truncated for both α and k as M is increased. Hence, although k and α may have large values on the retreating blade, if the Mach number

is high enough, the corner value imposed by the interpolation scheme may yield a value of the damping which is considerably removed from the actual damping for the given conditions. It is felt that this compromise limits the usefulness of the free Mach number interpolation scheme; and the remainder of the results considered herein will be restricted to the use of the present data for M = 0.2 only, with occasional reference to the use of the Reference 1 data.

The actual effect of these potentially unstable regions on the stall flutter response of the rotor is probably not too serious for the few cases considered so far in this report. This is because the torsional vibration frequency of 27.3 cps corresponds to an 8-cycle-per-revolution torsional motion; hence, each complete cycle will extend over 45 degrees of azimuth. The largest of the two unstable regions predicted by the use of the present data for M = 0.2 extends for only 25 degrees of azimuth; therefore it is incapable of exciting more than a half cycle of torsional response. Thereafter, the aerodynamic damping returns to a large positive value, which is sufficient to damp out the motion.

COMPARISON WITH RESULTS OF REFERENCE 2

After the work reported herein was well under way, it was found that a parallel study had been carried out, Reference 2, in which both an oscillatory limit-cycle experiment was conducted and a stability analysis based on available aerodynamic data was carried out. The significant result of Reference 2 is the fact that a region of instability can exist for the retreating blade. This is shown in Figure 13 of Reference 2 and it is interesting to note that the damping variation with ψ portrayed in this figure first increases with ψ for the advancing blade and reaches a maximum value at approximately ψ = 60 degrees, after which it decreases to zero at approximately ψ = 225 degrees, which indicates an instability over the approximate range $225^\circ < \psi < 360^\circ$. This bears a very strong resemblance to the results shown in the lower portion of Figure 25 of the present volume, although there are certain significant differences between the two results, particularly in the region of the retreating blade. Specifically, the present result indicates two narrow, unstable regions separated by a stable region, while the Reference 2 result predicts a rather broad, continuous region of instability. (Note that the result based on Reference 1 data in Figure 25 also agrees closely with the result from the present data; the deep instability over the range $340^\circ \leq \psi \leq 366^\circ$ is matched almost exactly, and there is a tendency toward instability in the vicinity of ψ = 240 degrees.)

The general agreement between the present results and those of Reference 2 is very encouraging in view of the fact that, although these were parallel studies, they were carried out independently of one another and utilized distinctly different sets of input data, both for rotor performance characteristics and for unsteady aerodynamic damping data.

The differences in input data lead directly to the differences in the stability results on the retreating blade. First, the damping data used in Reference 2 were synthesized from earlier results in Reference 4, 12, and

15. Although these data were corrected for static stalling angles and rotational axis location, the basic profile shapes were undoubtedly different from the NACA 0012 profile used herein and could conceivably lead to differences in the coefficient values. In particular, the first two-dimensional damping curve to become negative in Figure 8 of Reference 2 is that for $\alpha = 8$ degrees; whereas in the present study, the first to become negative is that for $\alpha = 13$ degrees, as seen in either Figure 14 or in Table IV. These differences in damping coefficient behavior are certainly reflected in the three-dimensional damping response differences noted above.

A second important difference between the two results lies in the rotor loading characteristics considered in each case. In Reference 2, the maximum blade incidence angle is $\alpha \cong 16$ degrees on the retreating blade, which yields almost the maximum possible value of negative aerodynamic damping. In contrast to this, the maximum rotor incidence angle for the present case is $\alpha \cong 40$ degrees on the retreating blade (see Figure 23) which is considerably beyond the point of maximum negative damping and, in fact, is also considerably beyond the point where the two-dimensional damping becomes positive once again. Thus, the double instability predicted in Figure 25 is explained quite simply by a careful study of Figure 23. In particular, Figure 23 indicates that an initial region of instability may be encountered in the third quadrant as the incidence angle increases through the negative damping regime, followed by a stable region as the positive damping regime is penetrated at high incidence angles. A second region of instability may be encountered near the interface of the fourth and first quadrants, as the incidence angle decreases once again through the negative damping regime.

STABILITY IMPLICATIONS OF LOADING VARIATIONS

The observations of both the similarities and differences between the present work and the results of Reference 2 led rather naturally to the question of rotor loading variations and to what their effect on rotor stability might be. Specifically, it was decided to reduce the effective loading of the maximum load condition of the S-61F to determine whether or not the system would experience the same extended region of instability as that described in Reference 2. Rather than employing an exact rotor performance calculation for each new loading condition desired, it was decided instead to multiply the entire incidence angle distribution over the rotor by a constant factor. In other words, a factor of 0.5 might be applied to the incidence angle distribution over the rotor disc, whereupon all incidence angles would be halved before the table search for damping values would be employed. No changes were made in the k-distribution. Although this procedure neglected the effect of loading changes on rotor inflow, it was felt that any error incurred would be of second order in relation to the observed changes in stability characteristics.

The values of the incidence angle multiplier chosen for this study were 0.9, 0.8, 0.7, 0.667, 0.5 and 0.375. The results obtained with these multipliers are presented in Figure 26. It is clear, from the bottom portion of Figure 26 that the incidence angle reduction produced by the 0.8 and 0.9 multipliers was insufficient to remove the stable region lying between the

unstable extremes, although the two unstable regions tended to move toward one another. Furthermore, the azimuthal extent of each unstable region increased with decreasing multiplier level.

In the center portion, the 0.667 and 0.7 multipliers both yielded continuously unstable regions. In both of these cases, it appears that the multiplier caused a sufficient reduction in α to prevent the incidence angle from exceeding the upper limit of the unstable region. Although the initial and final azimuth angles for instability are somewhat less than they were for the original data, the total extent of the unstable region is considerably greater for the 0.7 multiplier than for the original data. Specifically, it encompasses 95 degrees of azimuth, for an 8-cycle-per-revolution torsional motion, this amounts to slightly more than two full cycles of motion which can be excited by this unstable region. This behavior is now quite consistent with the result given in Reference 2.

Finally, in the top portion of Figure 26, the multipliers 0.5 and 0.375 are small enough to reduce the incidence angle to levels below the unstable limit. In fact, use of the 0.375 multiplier yields a near sinusoidal response, characteristic of potential flow behavior. No stall flutter would be possible with these multipliers.

A further clarification of these stability characteristics is afforded by Figure 27 in which the $k - \alpha$ trajectory for one cycle of motion for each of three multiplier values has been superimposed on the top view of the aerodynamic damping surface for $M = 0.2$ only. This figure clearly shows that, in the case of the original data, the trajectory passes completely through the unstable region twice and emerges into the stable regions on either side of it each time. This accounts for the double region of instability for this case. It is also seen that the trajectory for a multiplier of 0.7 remains within the unstable region over a substantial portion of each cycle, which produces the extensive region of instability. Finally, the trajectory for a multiplier of 0.5 is seen to miss the unstable region completely.

RESULTS

With regard to the two-dimensional damping parameter in pitch for the NACA 0012 airfoil, the following results were obtained:

1. The measured values of the two-dimensional aerodynamic damping parameter, $\Xi_{\alpha 2}$, are in good agreement with potential flow theory for low mean incidence angles, $\alpha_M \leq 9°$, and depart from the theory for $\alpha_M \geq 12°$.

2. At low incidence angles, $\Xi_{\alpha 2}$ increases linearly with reduced frequency parameter, k .

3. At high incidence angles, $\Xi_{\alpha 2}$ initially increases with k , then decreases to a negative level (implying instability), and finally increases again.

4. The Reference 1 and the present data are in generally good agreement over a substantial range of both k and α_M . Both sets of data predict essentially the same two-dimensional stability boundary at moderate values of k . Other results for much different profile shapes are in good qualitative agreement with the present data.

With regard to the three-dimensional damping in pitch and the attendant stability of an S-61F helicopter rotor blade, the following results were obtained:

5. At low blade loading and flight speed, the rotor blade is stable over the entire disc. The damping in pitch is greater for the advancing blade than for the retreating blade.

6. At large blade loading and flight speed, the rotor blade is still stable over the advancing portion but tends toward instability over the retreating portion of the rotor disc.

7. In the case of the largest loading and flight speed considered thus far, the predicted negative damping region for the retreating blade is confined to two small pockets, each of which extends over an insufficient azimuth range to excite more than one-half cycle of torsional motion.

8. Use of the Reference 1 data yields slightly larger blade damping for the advancing blade but produces good agreement with the present data for the retreating blade, even in the case of retreating blade instability.

9. If the loading is reduced (without changing inflow), a condition can be reached wherein two full cycles of torsional motion can be excited by the negative damping of the retreating blade.

10. The results of the present stability analysis are in good qualitative agreement with the results of Reference 2.

11. The available two-dimensional data for M = 0.3 are inadequate for use in the stability analysis. The data for M = 0.2 are sufficient, but they are limited to the low-velocity incompressible flow regime.

TABLE I. ORIGINAL TWO-DIMENSIONAL AERODYNAMIC DAMPING DATA, $\Xi_{\alpha 2}$, FOR M = 0.2

f(cps) =	0.5	1.0	2.0	4.0	8.0	12.0	16.0
k =	0.0140	0.0281	0.0562	0.1125	0.2250	0.3375	0.4500
$\alpha_M°$				Pitching Amplitude, $\bar{\alpha}$ = 4°			
0				0.111	0.222	0.386	0.536
3				0.111	0.261	0.386	0.536
6				0.092	0.235	0.373	0.523
9				0.092	0.261	0.392	0.516
12	-0.020	-0.052	-0.020	0.072	0.307	0.451	0.431
15	-0.020		-0.183	-0.235	-0.346	-.026/-.065	.268/.046
18				0.536	-0.686	0.360	.785/.569
21							
24							
27				0.477	0.157	0.732	1.124/1.431
30				0.307	0.065	.523/.503	1.131/1.046
32				-0.118	-0.190	.602/.915	-.301/-.810
$\alpha_M°$				Pitching Amplitude, $\bar{\alpha}$ = 6°			
0				0.131	0.259	0.485	0.636
3				.177/.119	0.264	0.447	0.619
6				0.137	0.279	0.462	0.651
9				0.160	0.314	0.482	0.639
12	-0.012	0.017	0.029	-0.044	0.058	0.392	0.604
15	-0.081	-0.078	0.099	0.055	-0.177	.038/.195	0.351
18	-0.116	0.110	0.015	0.099	-0.360	-0.674	-0.293
21			0.404	0.459	-0.346	-0.572	-0.468
24	0.029	0.020	0.058	0.471	0.911	0.813	0.279
27		0.049	0.369	0.270	0.503	0.709	1.173
30				0.232	.148/.256	0.569	1.156
32				0.116	0.465	0.691	0.918

TABLE I - CONCLUDED

f (cps) =	0.5	1.0	2.0	4.0	8.0	12.0	16.0
k =	0.0140	0.0281	0.0562	0.1125	0.2250	0.3375	0.4500
$\alpha_M°$	Pitching Amplitude, $\bar{\alpha} = 8°$						
0				0.127	0.266	0.462	0.619
3				0.139	0.286	0.444	
6				0.139	0.296	0.458	
9				0.152	0.310	0.477	
12	0.020	0.059	0.292	-0.062	-0.093	0.248	0.536
15	0.047	0.054	0.015	0.052	-0.221	-0.098	0.092
18	0.047	0.170	0.237	0.190	-0.258	-0.606	-0.302
21	0.066	0.137	0.294	0.369	-0.183	-0.660	-0.804
24	0.051	0.141	0.399	0.430	0.417	-0.186	-0.784
27	0.111	-0.007	0.330	0.150	0.595	0.770	1.028
30	0.085	0.093	0.508	0.023	0.458	0.585	1.085
32	0.028	0.036	-0.103	0.145	0.469	0.802	

TABLE II ORIGINAL TWO-DIMENSIONAL AERODYNAMIC DAMPING DATA, $\Xi_{\alpha 2}$, FOR M = 0.3

f(cps)=	0.5	1.0	2.0	4.0	8.0	12.0	16.0
k	= 0.0094	0.0187	0.0375	0.0750	0.150	0.225	0.300
$\alpha_M°$				Pitching Amplitude, $\bar{\alpha}$ = 4°			
0				0.065	0.176	0.281	0.392
3				0.085	0.183	0.314	0.366
6				0.098	0.209	0.314	0.399
9				0.098	0.222	0.340	0.444
12	0.059	-0.052	0.013	0.092	-0.150	-0.013	-0.477
15	0.007	0.177	0.320	0.085	0.288	0.026	-1.373/-.889
18				0.059	0.601	0.726	.196/-.281
21				1.431	0.902	1.712/.758	.431/.706
24				0.863	0.614	0.595	1.373/1.575
27				0.523	1.229/1.503		1.203/1.144
$\alpha_M°$				Pitching Amplitude, $\bar{\alpha}$ = 6°			
0				0.096	0.177	0.285	0.383
3				0.087	0.168	0.279	0.398
6				0.099	0.186	0.282	0.412
9				0.038	0.166	0.311	0.430
12			0.070	0.215	0.017	-0.073	-0.171
15	-0.058	0.157	0.134	0.322	0.180	-0.523	-0.250
18	0.009	0.122	0.261	0.360	0.317	-0.110	0.099
21				0.601	0.424	-0.032	0.613
24				0.221	0.749	0.651	
27				0.273	0.468	0.511	0.186
30				0.192	0.325	0.314	0.581
32				0.131	0.224		

TABLE II - CONCLUDED

f(cps) =	0.5	1.0	2.0	4.0	8.0	12.0	16.0
k =	0.0094	0.0187	0.0375	0.0750	0.150	0.225	0.300
α_M°	Pitching Amplitude, $\bar{a}$ = 8°						
0				0.06[illegible]	0.193	0.312	0.407
3				0.085	0.186	0.314	
6				0.093	0.214	0.309	
9				0.131	0.021	0.227	
12	-0.013	-0.087	0.095	-0.154	0.240	-0.049	0.291
15	-0.025	-0.103	-0.134	0.294	.358/.173	0.322	0.103
18	-0.062	-0.003	0.172	0.324	0.387	-.157/-.229	.002/.060
21	0.078	0.047	0.245	0.358	0.485	0.163	0.216
24				0.221	-0.526	-0.371	
27	-0.054	-0.002	-0.198	0.340	0.449	0.544	
30	-0.075	-0.162	-0.062	0.201	0.216	0.567	

TABLE III. ORIGINAL TWO-DIMENSIONAL AERODYNAMIC DAMPING DATA, $\Xi_{\alpha 2}$, FOR M = 0.4

f(cps) =	0.5	1.0	2.0	4.0	8.0	12.0	16.0
k =	0.007	0.014	0.028	0.0562	0.1125	0.1688	0.225
α_M°				Pitching Amplitude, $\bar{\alpha} = 4^\circ$			
0				0.072	0.124	0.222	0.307
3				0.072	0.144	0.216	0.314
6				0.085	0.163	0.242	0.320
9				0.144	.150/.137	0.281	.373/.281
12	0.013	0.026	0.098	0.183	0.412	0.484	-.170/.111
15	0.059	-0.072	0.196	0.039	0.418	0.543	0.569
18				0.320	0.575	1.013	0.771
21				0.373	0.131	0.765	1.020
24				0.183		0.523	1.020
α_M°				Pitching Amplitude, $\bar{\alpha} = 6^\circ$			
0				0.064	0.122	0.206	0.288
3				0.061	0.139	0.212	0.296
6				0.093	0.186	0.267	0.369
9				0.090	0.174	0.183	.163/.232
12	0.006	0.020	0.006	0.134	0.116	0.163	0.102
15		0.015	0.023	0.110	0.078	0.038	0.067
18	0.055	-0.023	0.041	0.151	0.389	0.177	0.090
21				0.343	0.378	0.392	0.305
24				0.035	0.256		
α_M°				Pitching Amplitude, $\bar{\alpha} = 8^\circ$			
0				0.060	0.136	0.214	0.320
3				0.065	0.149	0.239	
6				0.098	0.126	0.147	
9				0.113	0.142	0.141	

TABLE IV. PAIRED TWO-DIMENSIONAL AERODYNAMIC DAMPING DATA, $\Sigma_{\alpha 2}$, FOR M = 0.2

$\alpha_v°$	σ_T	[illegible]	0.025	0.050	0.075	0.100	0.150	0.200	0.250	0.300	0.350	0.400	0.450	0.500
0.	0	0.	0.020	0.040	0.070	0.100	0.170	0.240	0.300	0.380	0.450	0.520	0.590	0.640
1.	0.077	0.	0.020	0.040	0.070	0.100	0.170	0.240	0.300	0.380	0.450	0.520	0.600	0.650
2.	0.154	0.	0.020	0.040	0.070	0.100	0.170	0.240	0.300	0.380	0.450	0.520	0.600	0.660
3.	0.231	0.	0.020	0.040	0.080	0.110	0.180	0.240	0.300	0.380	0.450	0.520	0.600	0.670
4.	0.308	0.	0.030	0.050	0.090	0.120	0.180	0.240	0.300	0.370	0.440	0.510	0.590	0.660
5.	0.385	0.	0.030	0.050	0.090	0.120	0.180	0.240	0.300	0.370	0.440	0.510	0.590	0.660
6.	0.462	0.	0.030	0.050	0.090	0.120	0.180	0.240	0.300	0.370	0.440	0.520	0.590	0.660
7.	0.539	0.	0.030	0.050	0.090	0.120	0.180	0.240	0.310	0.370	0.440	0.510	0.590	0.650
8.	0.616	0.	0.030	0.060	0.090	0.120	0.180	0.240	0.310	0.370	0.440	0.510	0.580	0.650
9.	0.693	0.	0.030	0.060	0.080	0.110	0.170	0.230	0.300	0.360	0.430	0.500	0.570	0.640
10.	0.770	0.	0.030	0.050	0.080	0.110	0.160	0.220	0.280	0.350	0.420	0.490	0.550	0.630
11.	0.847	0.	0.020	0.030	0.050	0.080	0.110	0.160	0.220	0.340	0.410	0.490	0.540	0.600
12.	0.924	0.	0.	0.010	0.010	0.020	0.040	0.080	0.160	0.280	0.400	0.470	0.520	0.560
13.	1.000	0.	0.010	0.010	0.010	0.010	-0.020	0.	0.060	0.180	0.320	0.390	0.440	0.480
14.	1.077	0.	0.020	0.020	0.	-0.020	-0.070	-0.090	-0.060	0.050	0.180	0.260	0.330	0.380
15.	1.154	0.	0.030	0.030	0.020	0.	-0.030	-0.190	-0.180	-0.100	0.	0.110	0.220	0.320
16.	1.231	0.	0.040	0.050	0.040	0.030	-0.080	-0.250	-0.290	-0.250	-0.180	-0.050	0.120	0.320
17.	1.308	0.	0.060	0.090	0.120	0.110	-0.010	-0.260	-0.390	-0.400	-0.360	-0.220	0.050	0.400
18.	1.385	0.	0.080	0.140	0.200	0.250	0.080	-0.250	-0.470	-0.520	-0.510	-0.340	-0.040	0.500
19.	1.462	0.	0.090	0.190	0.260	0.320	0.160	-0.210	-0.500	-0.600	-0.600	-0.440	-0.140	0.460
20.	1.539	0.	0.110	0.220	0.310	0.370	0.280	-0.160	-0.480	-0.620	-0.620	-0.520	-0.350	-0.120
21.	1.616	0.	0.120	0.250	0.340	0.400	0.360	0.020	-0.380	-0.540	-0.600	-0.540	-0.533	-0.420
22.	1.693	0.	0.140	0.240	0.370	0.410	0.440	0.190	-0.120	-0.340	-0.480	-0.580	-0.540	-0.580
23.	1.770	0.	0.130	0.270	0.360	0.420	0.530	0.450	0.300	-0.080	-0.220	-0.460	-0.540	-0.640
24.	1.847	0.	0.120	0.240	0.340	0.420	0.560	0.660	0.640	0.400	0.260	-0.140	-0.370	-0.520
25.	1.924	0.010	0.120	0.220	0.340	0.380	0.520	0.600	0.630	0.570	0.380	0.260	0.050	-0.040
26.	2.000	0.040	0.130	0.230	0.310	0.370	0.440	0.510	0.580	0.620	0.680	0.730	0.740	0.840
27.	2.077	0.040	0.130	0.220	0.280	0.310	0.370	0.440	0.530	0.640	0.780	0.890	1.030	1.210
28.	2.154	0.040	0.140	0.220	0.250	0.260	0.310	0.380	0.480	0.650	0.800	0.970	1.140	1.300
29.	2.231	0.050	0.160	0.250	0.260	0.250	0.250	0.310	0.410	0.580	0.720	0.940	1.120	1.360
30.	2.308	0.060	0.190	0.270	0.290	0.260	0.210	0.240	0.320	0.440	0.610	0.820	1.050	1.320
31.	2.385	0.040	0.170	0.240	0.260	0.220	0.150	0.200	0.300	0.470	0.650	0.830	0.940	1.220
32.	2.462	0.	0.100	0.180	0.180	0.120	0.100	0.150	0.300	0.540	0.720	0.800	0.820	0.920

TABLE V. FAIRED TWO-DIMENSIONAL AERODYNAMIC DAMPING DATA, Ξ_{32}, FOR M = 0.3

$\alpha_M°$	σ_T	k = 0.	0.025	0.050	0.075	0.100	0.150	0.200	0.250	0.300	0.350
0.	0	0.	0.030	0.050	0.080	0.120	0.180	0.250	0.320	0.400	0.470
1.	0 077	0.	0.030	0.060	0.080	0.120	0.180	0.250	0.320	0.390	0.460
2.	0 154	0.	0.030	0.060	0.080	0.120	0.180	0.250	0.320	0.380	0.450
3.	0 231	0.	0.030	0.060	0.090	0.120	0.180	0.250	0.320	0.380	0.450
4.	0 308	0.	0.030	0.060	0.090	0.120	0.180	0.250	0.310	0.380	0.450
5.	0 385	0.	0.040	0.070	0.100	0.120	0.190	0.260	0.310	0.380	0.450
6.	0 462	0.	0.040	0.070	0.100	0.120	0.190	0.260	0.320	0.380	0.460
7.	0 539	0.	0.040	0.070	0.100	0.120	0.190	0.260	0.320	0.390	0.470
8.	0 616	0.	0.040	0.070	0.090	0.120	0.190	0.260	0.330	0.400	0.480
9.	0 693	0.	0.040	0.070	0.090	0.120	0.170	0.240	0.310	0.390	0.480
10.	0 770	0.	0.040	0.070	0.090	0.110	0.140	0.180	0.240	0.330	0.480
11.	0.847	0.	0.040	0.060	0.090	0.090	0.080	0.060	0.120	0.230	0.440
12.	0 924	0.	0.040	0.050	0.080	0.070	0.060	-0.030	0.	0.130	0.320
13.	1 000	0.	0.050	0.070	0.060	0.100	0.100	-0.030	-0.080	0.	0.060
14.	1 077	0.	0.060	0.100	0.130	0.160	0.160	-0.020	-0.140	-0.140	-0.140
15.	1 154	0.	0.080	0.130	0.180	0.220	0.230	0.010	-0.170	-0.210	-0.210
16.	1 231	0.	0.090	0.170	0.230	0.280	0.310	0.060	-0.200	-0.220	-0.230
17.	1 308	0.	0.120	0.210	0.280	0.350	0.400	0.110	-0.200	-0.180	-0.180
18.	1 385	0.	0.130	0.250	0.330	0.410	0.480	0.180	-0.180	-0.120	-0.040
19.	1 462	0.	0.160	0.290	0.400	0.480	0.540	0.260	-0.060	0.060	0.160
20.	1 539	0.	0.180	0.340	0.460	0.540	0.600	0.350	0.220	0.260	0.380
21.	1 616	-0.010	0.160	0.390	0.560	0.620	0.640	0.490	0.390	0.460	0.620
22.	1 693	-0.030	0.180	0.440	0.630	0.680	0.670	0.580	0.520	0.650	0.850
23.	1 770	-0.040	0.180	0.460	0.660	0.700	0.680	0.590	0.590	0.820	1.100
24.	1 847	-0.040	0.180	0.460	0.660	0.690	0.660	0.600	0.640	0.970	1.360
25.	1 924	-0.040	0.140	0.410	0.600	0.630	0.620	0.590	0.660	1.030	1.480
26.	2 000	-0.040	0.100	0.340	0.510	0.560	0.570	0.580	0.660	1.030	1.520
27.	2 077	-0.050	0.070	0.260	0.420	0.480	0.520	0.540	0.650	0.980	1.460
28.	2 154	-0.060	0.050	0.200	0.340	0.400	0.460	0.500	0.610	0.920	1.280
29.	2 231	-0.080	0.020	0.160	0.270	0.330	0.400	0.440	0.560	0.820	1.040
30.	2 308	-0.100	0.	0.110	0.200	0.260	0.330	0.380	0.510	0.700	0.880
31.	2 385	-0.100	0.	0.080	0.150	0.190	0.250	0.310	0.430	0.590	0.750
32.	2 462	-0.100	0.	0.060	0.100	0.120	0.170	0.240	0.340	0.470	0.640

TABLE VI. FAIRED TWO-DIMENSIONAL AERODYNAMIC DAMPING DATA, $\Xi_{\alpha 2}$, FOR M = 0.h

$\alpha_M°$	σ_T	k = 0.	0.025	0.050	0.075	0.100	0.150	0.200	0.250
0.	0	0.	0.040	0.060	0.080	0.100	0.180	0.270	0.370
1.	0.077	0.	0.040	0.060	0.080	0.110	0.180	0.260	0.350
2.	0.154	0.	0.030	0.060	0.090	0.120	0.190	0.260	0.340
3.	0.231	0.	0.030	0.060	0.090	0.130	0.200	0.260	0.340
4.	0.308	0.	0.030	0.060	0.100	0.140	0.210	0.270	0.340
5.	0.385	0.	0.030	0.060	0.100	0.130	0.210	0.280	0.360
6.	0.462	0.	0.040	0.060	0.100	0.130	0.200	0.290	0.380
7.	0.539	0.	0.050	0.080	0.110	0.140	0.200	0.280	0.370
8.	0.616	0.	0.070	0.110	0.130	0.160	0.200	0.260	0.310
9.	0.693	0.	0.060	0.110	0.130	0.170	0.220	0.230	0.210
10.	0.770	0.	0.050	0.100	0.140	0.170	0.230	0.200	0.100
11.	0.847	0.	0.050	0.090	0.140	0.180	0.250	0.200	-0.040
12.	0.924	0.	0.050	0.090	0.140	0.190	0.270	0.200	-0.100
13.	1.000	0.	0.060	0.100	0.150	0.190	0.280	0.220	-0.090
14.	1.077	0.	0.060	0.110	0.160	0.200	0.300	0.260	-0.040
15.	1.154	0.020	0.070	0.110	0.170	0.210	0.330	0.310	0.040
16.	1.231	0.040	0.070	0.110	0.180	0.260	0.400	0.380	0.160
17.	1.308	0.050	0.080	0.130	0.230	0.350	0.480	0.460	0.260
18.	1.385	0.060	0.080	0.170	0.290	0.420	0.550	0.530	0.380
19.	1.462	0.060	0.090	0.180	0.300	0.410	0.570	0.580	0.500
20.	1.539	0.060	0.110	0.190	0.290	0.390	0.560	0.640	0.640
21.	1.616	0.050	0.110	0.180	0.270	0.350	0.540	0.680	0.770
22.	1.693	0.040	0.100	0.170	0.240	0.320	0.500	0.720	0.910
23.	1.770	0.040	0.090	0.140	0.180	0.270	0.460	0.740	1.070
24.	1.847	0.050	0.080	0.110	0.140	0.200	0.420	0.760	1.240

TABLE VII. FAIRED TWO-DIMENSIONAL AERODYNAMIC DAMPING DATA.

$\Xi_{\alpha 2}$, FROM REFERENCE 1

σ_T	k=0.	0.050	0.100	0.150	0.200	0.250	0.300	0.350	0.400
0	0.	0.079	0.157	0.235	0.314	0.393	0.471	0.550	0.628
0.1	0.	0.070	0.185	0.268	0.333	0.390	0.454	0.500	0.560
0.2	0.	0.049	0.175	0.274	0.328	0.373	0.424	0.450	0.479
0.3	0.	0.022	0.193	0.251	0.317	0.360	0.392	0.405	0.412
0.4	0.	-0.020	0.100	0.206	0.299	0.365	0.380	0.375	0.349
0.5	0.	-0.081	0.022	0.152	0.290	0.373	0.378	0.375	0.310
0.6	0.	-0.189	-0.053	0.098	0.255	0.372	0.385	0.359	0.281
0.7	0.	-0.322	-0.140	0.091	0.240	0.379	0.362	0.355	0.403
0.8	0.	-0.425	-0.218	0.033	0.245	0.348	0.292	0.365	0.598
0.9	0.	-0.440	-0.266	-0.017	0.172	0.255	0.180	0.368	0.734
1.0	0.	-0.365	-0.243	-0.110	-0.026	0.049	0.014	0.381	0.874
1.1	0.	-0.199	-0.173	-0.183	-0.242	-0.247	-0.164	0.333	0.970
1.2	0.	0.043	-0.056	-0.269	-0.454	-0.534	-0.315	0.249	1.017
1.3	0.	0.262	0.070	-0.323	-0.603	-0.696	-0.450	0.152	0.946
1.4	0.	0.380	0.183	-0.252	-0.584	-0.693	-0.525	0.021	0.694
1.5	0.	0.426	0.297	-0.122	-0.434	-0.531	-0.511	-0.200	0.307
1.6	0.	0.400	0.321	0.055	-0.132	-0.250	-0.293	-0.299	-0.109
1.7	0.	0.347	0.323	0.199	0.123	0.077	0.044	-0.024	-0.180
1.8	0.	0.279	0.260	0.263	0.294	0.344	0.348	0.291	0.331

TABLE VIII. TORSIONAL MODE SHAPE FUNCTION, $f_\alpha(\eta)$

Radius, r, (ft)	Dimensionless Spanwise Station, η	Mode Shape Function, f_α
8.44	0.000	0.32
10.81	0.105	0.42
13.19	0.211	0.51
15.56	0.316	0.60
17.94	0.421	0.69
20.31	0.526	0.78
22.69	0.632	0.86
25.06	0.737	0.93
27.44	0.842	0.98
29.81	0.947	1.00

CHANNEL WIDTH = 2.75 FT
CHANNEL HEIGHT = 7.75 FT

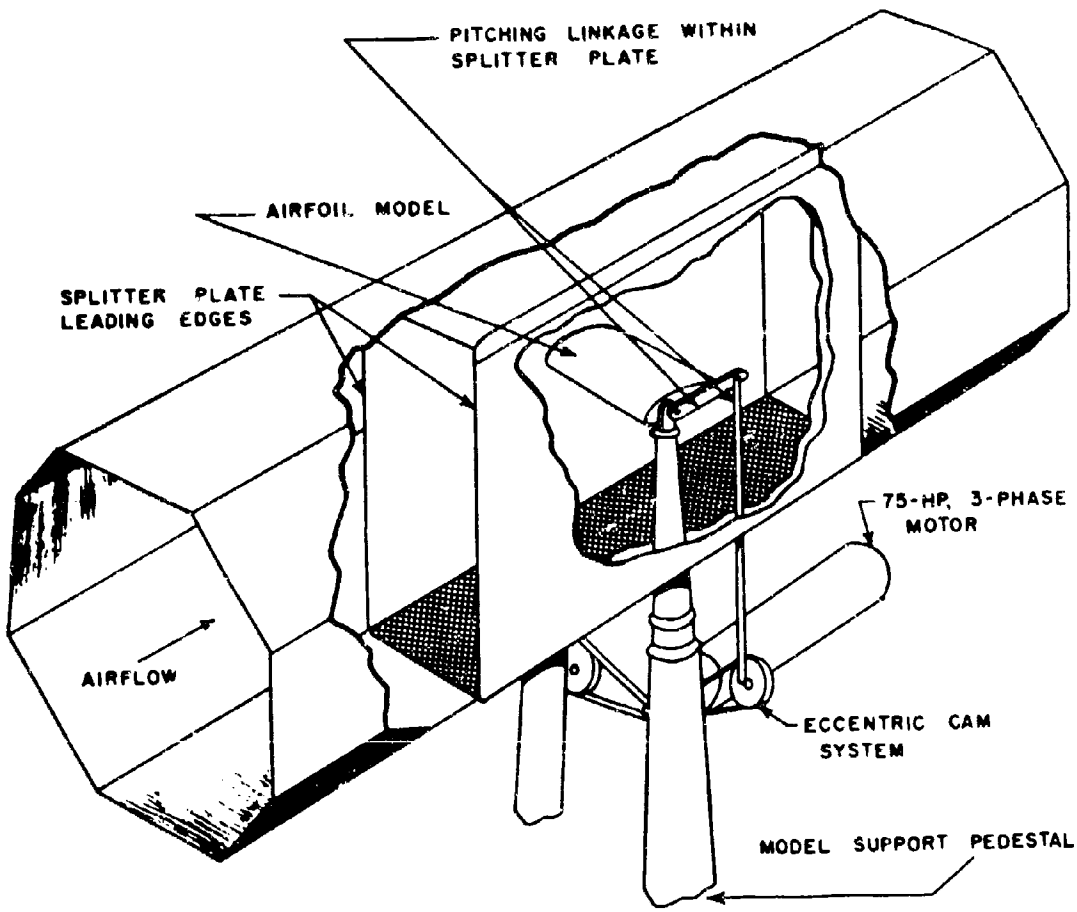

Figure 1. Two-Dimensional Channel for UAC 8-Foot Octagonal Wind Tunnel.

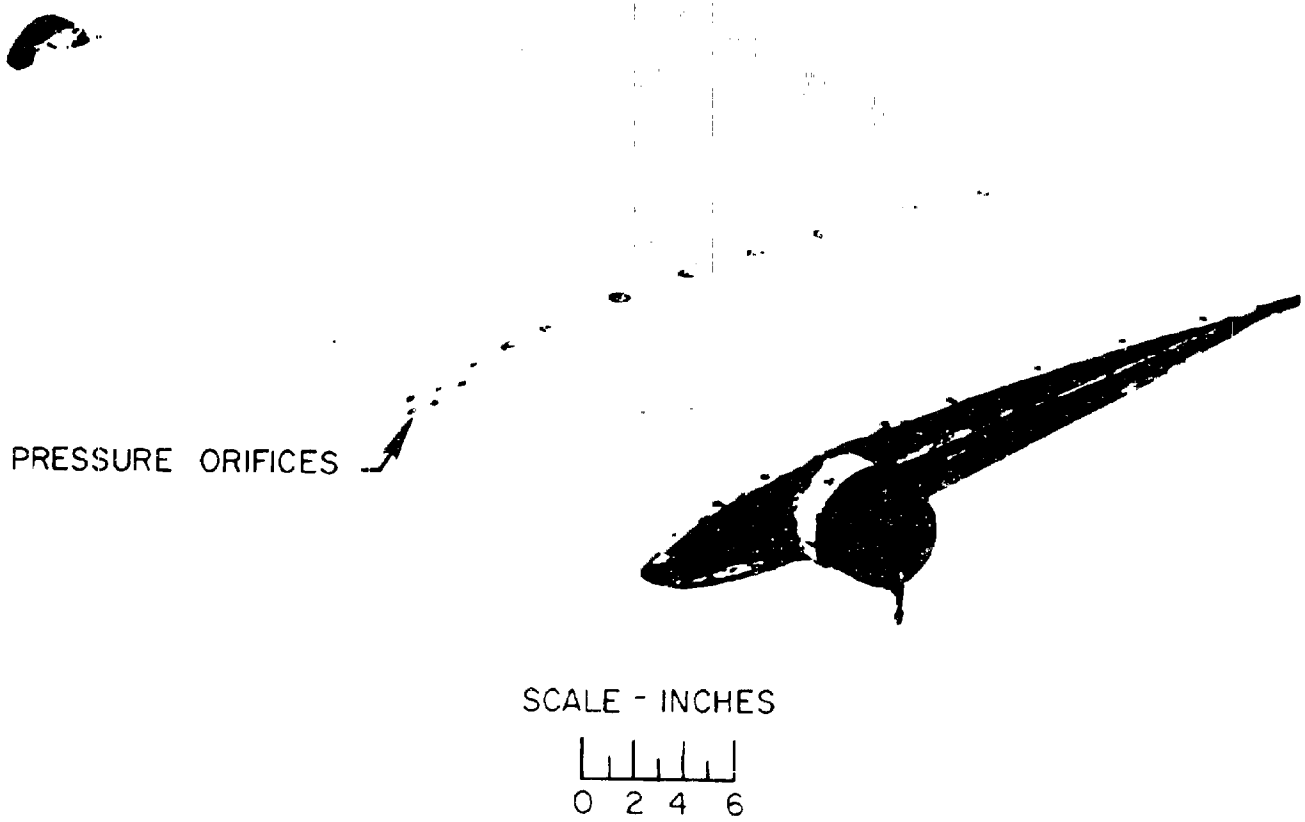

Figure 2. NACA 0012 Airfoil.

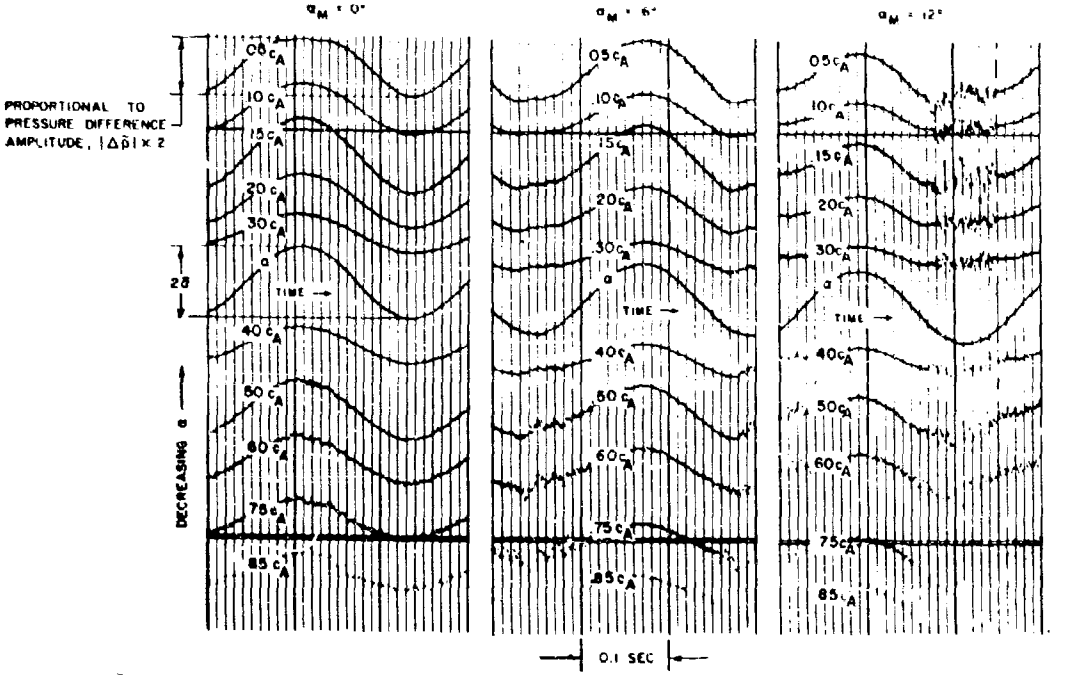

Figure 3. Oscillograph Traces of Pressures on Oscillating Two-Dimensional NACA 0012 Airfoil; M = .4, f = 4 cps, c = 2 ft, k = .057, $\bar{\alpha}$ = 6°.

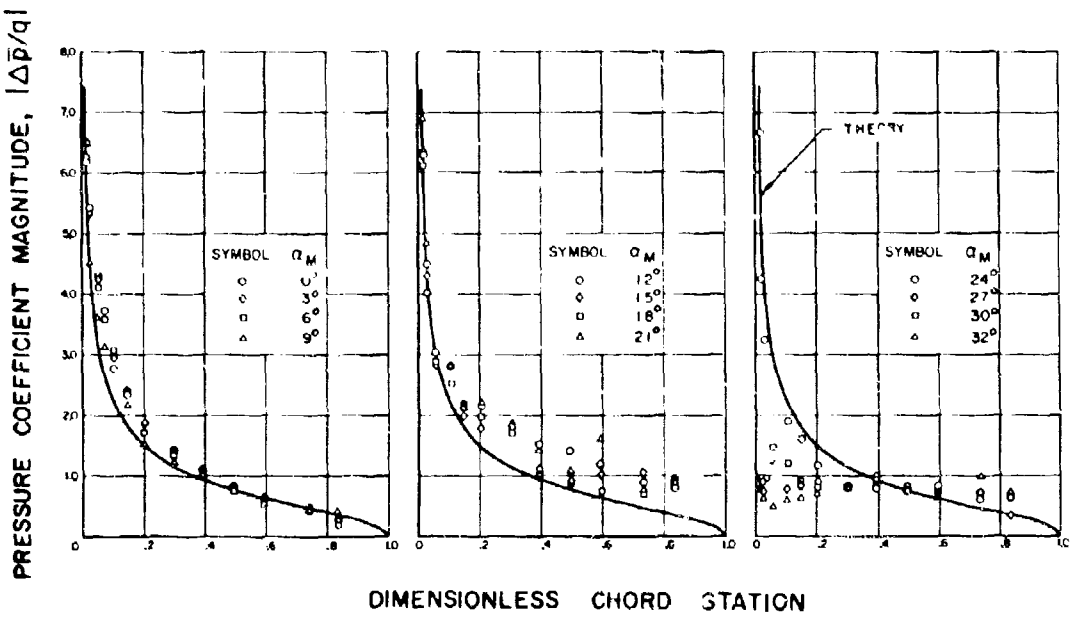

Figure 4. Unsteady Pressure Coefficient Magnitude Versus Chord Station; $\bar{\alpha}$=6°, M=.3, f=4 cps, k=.075.

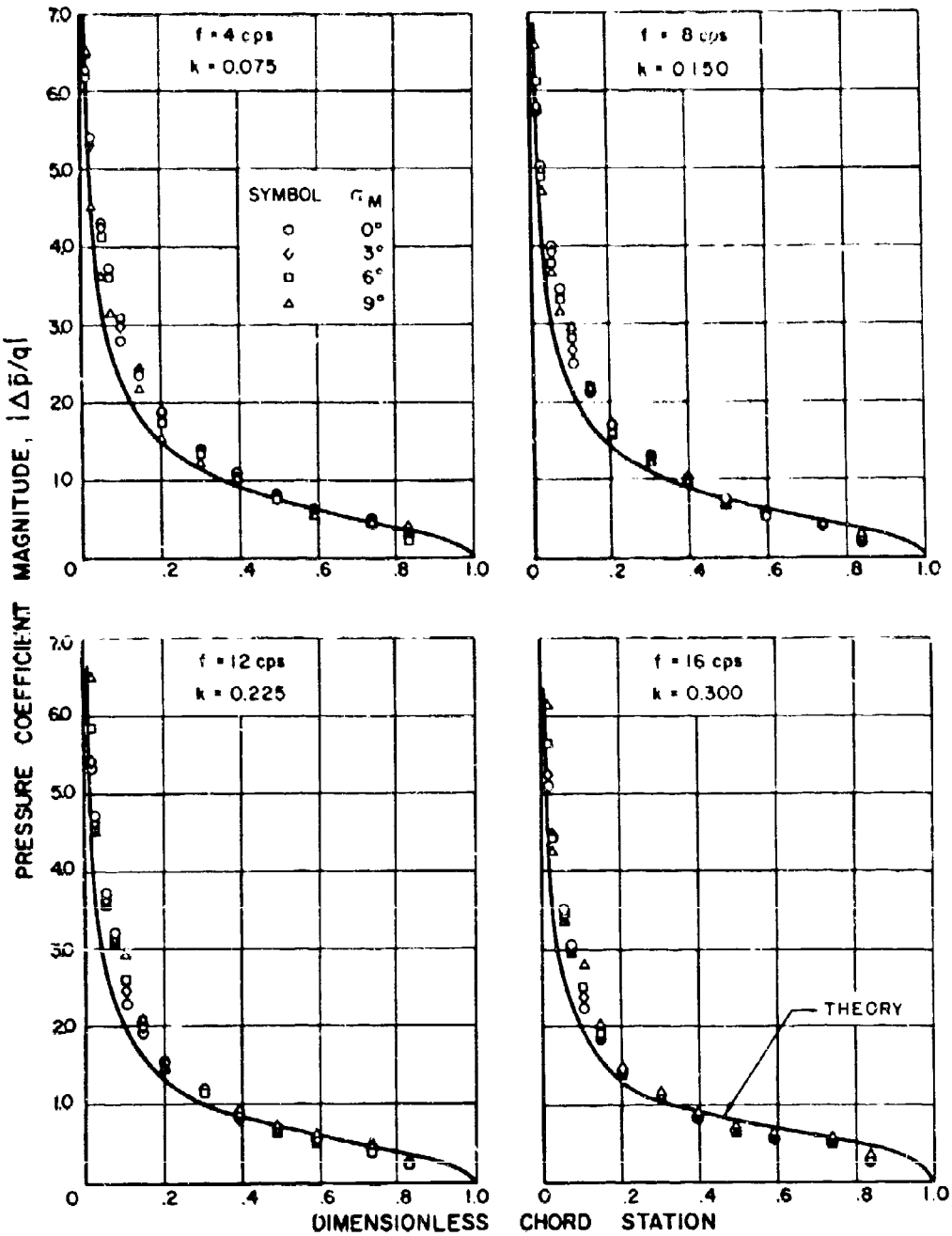

Figure 5. Unsteady Pressure Coefficient Magnitude Versus Chord Station; $\bar{\alpha} = 6°$, M=.3.

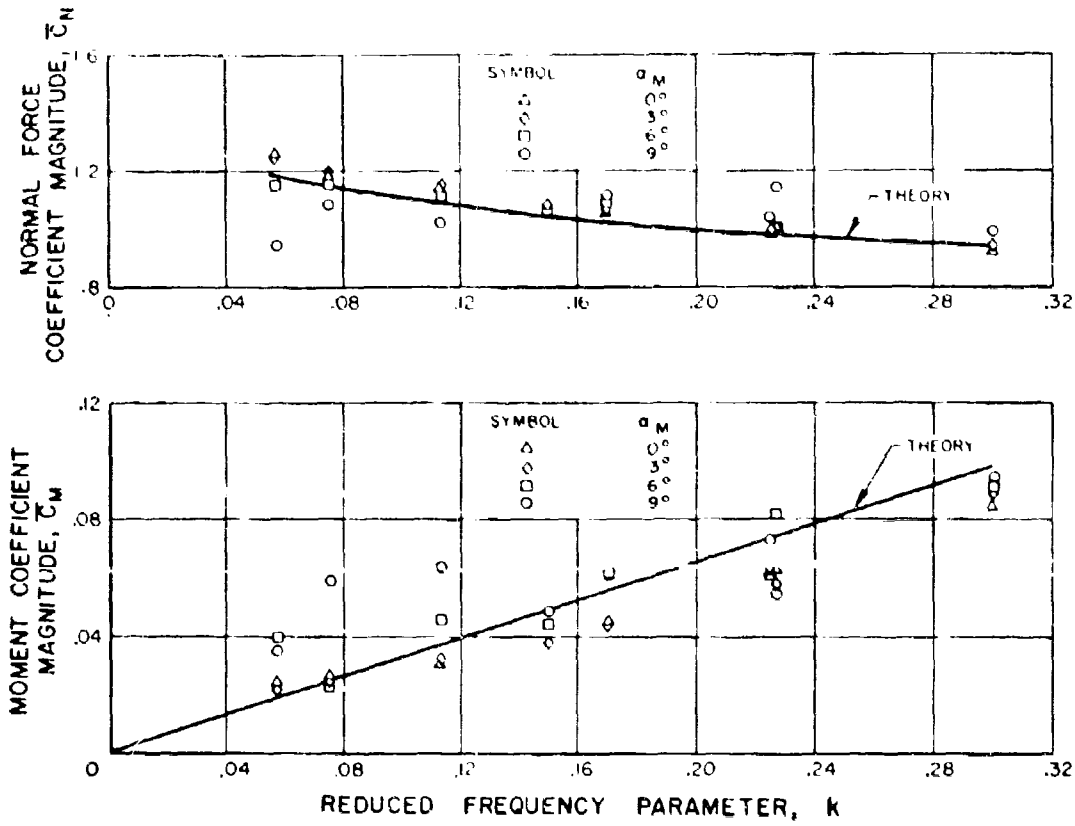

Figure 6. Variation of Normal Force Coefficient Magnitude and Moment Coefficient Magnitude With Reduced Frequency; $\bar{\alpha} = 6°$.

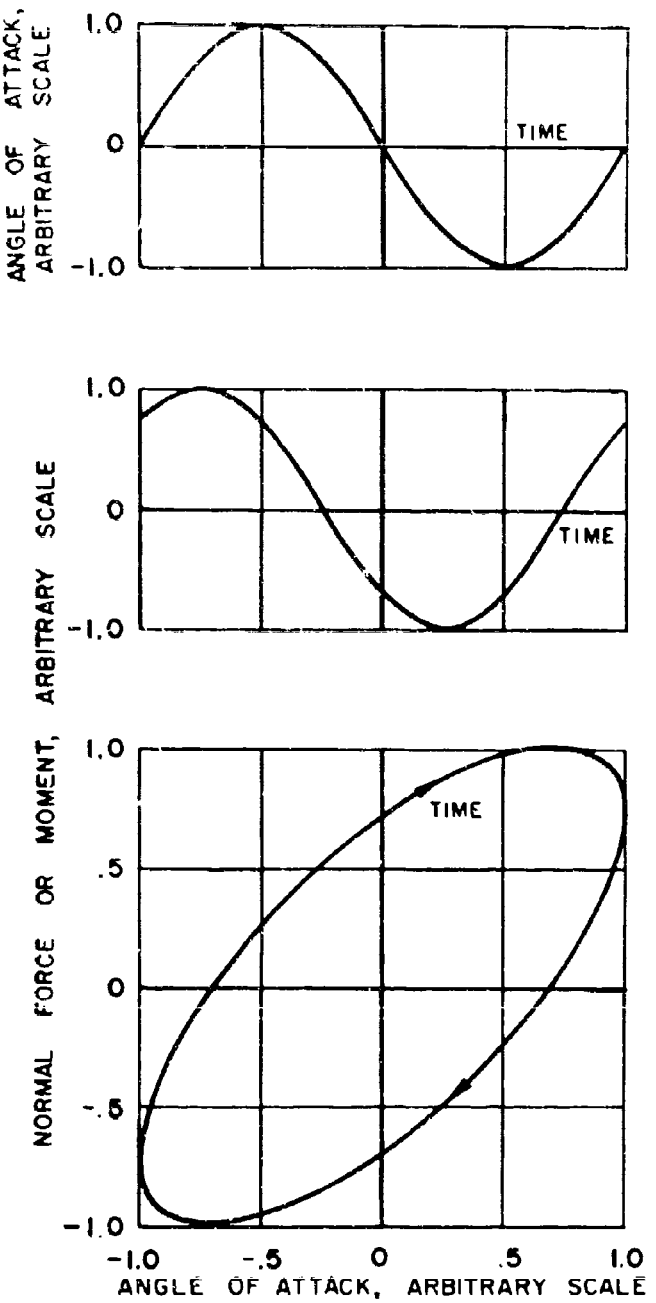

Figure 7. Hypothetical Normal Force or Moment - Angle of Attack Hysteresis Loops.

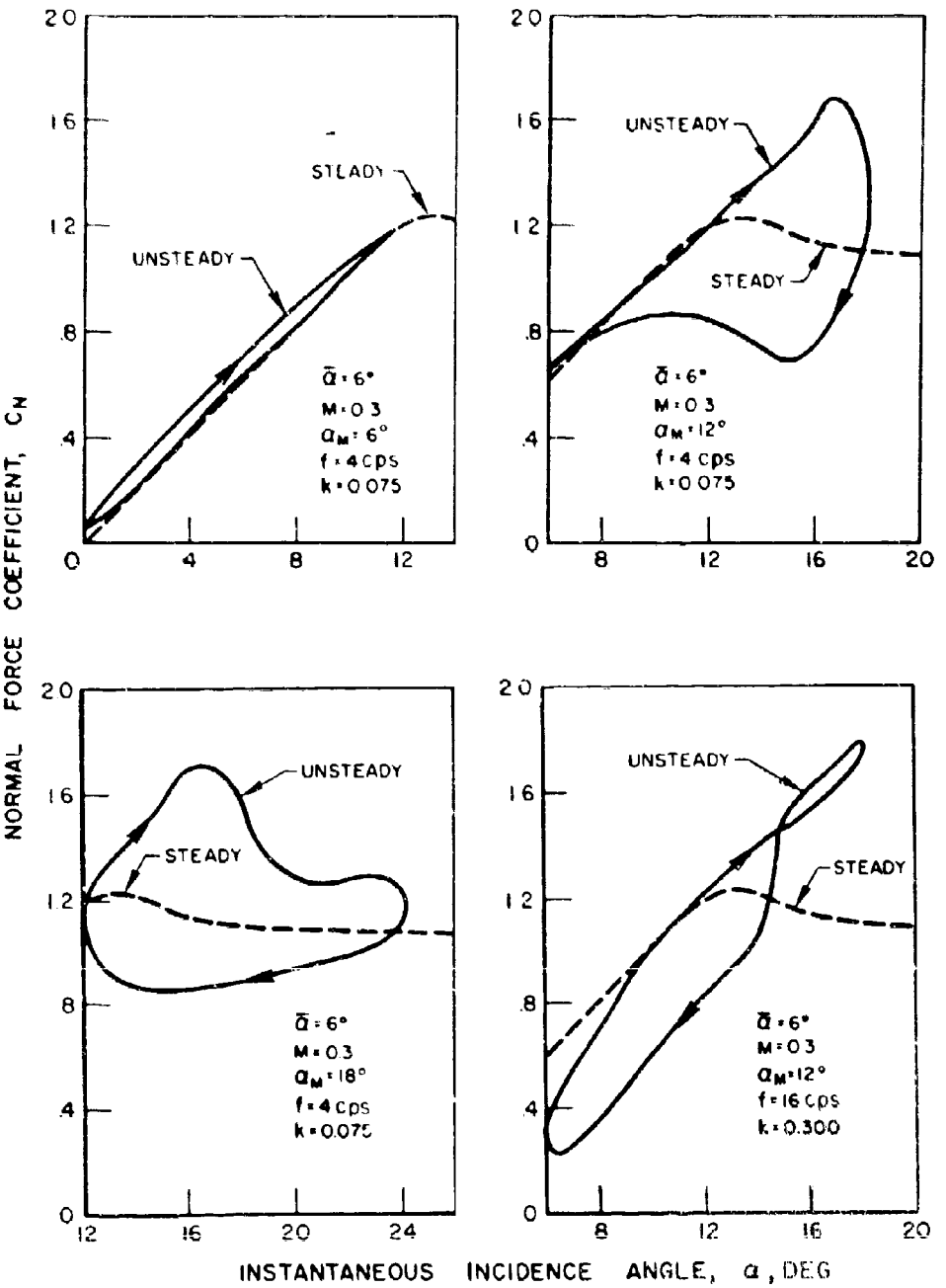

Figure 8. Normal Force Hysteresis Loops.

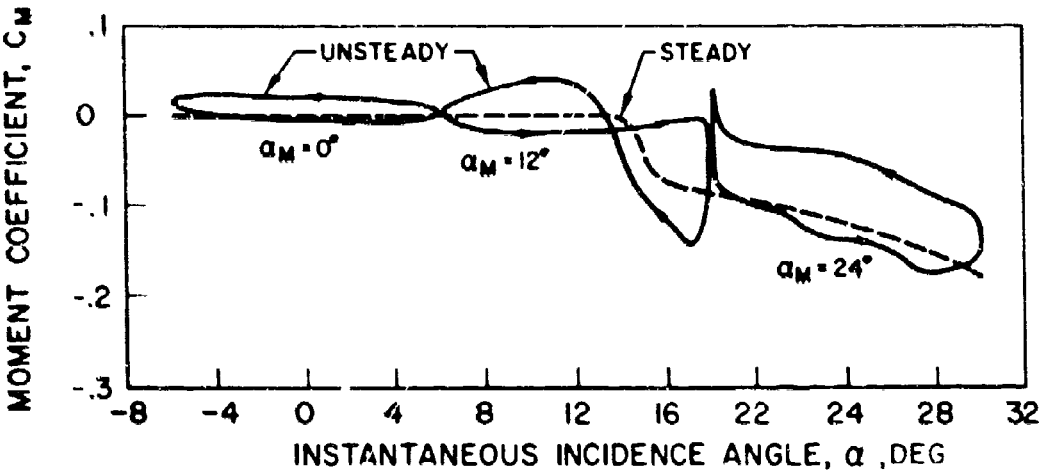

Figure 9. Effect of Mean Incidence Angle on Moment Hysteresis Loops; $\bar{\alpha} = 6°, M = .2, f = 4$ cps, $k = .112$.

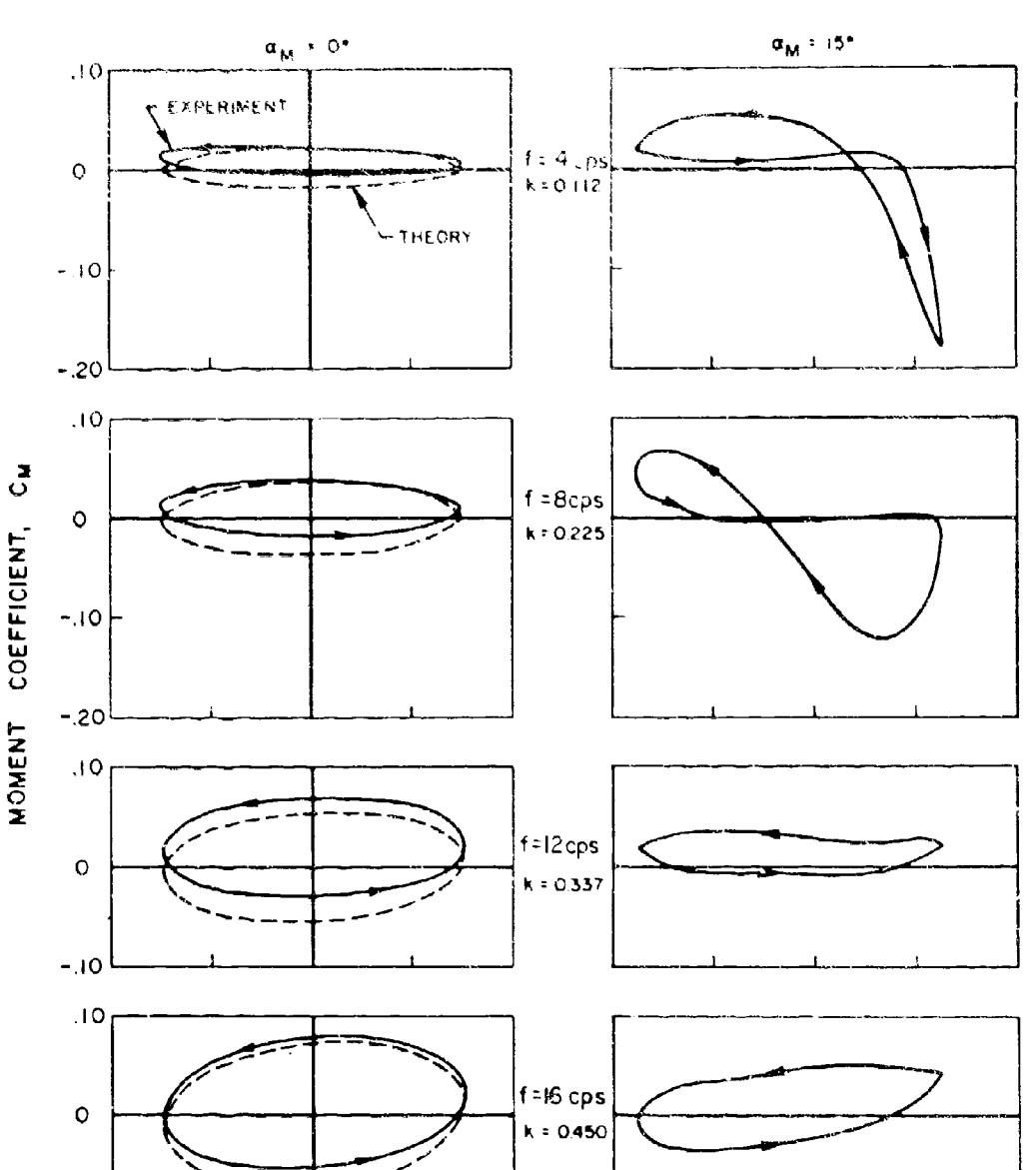

Figure 10. Effect of Frequency and Mean Incidence Angle on Moment Hysteresis Loops; $\bar{\alpha}$=6°, M=.2.

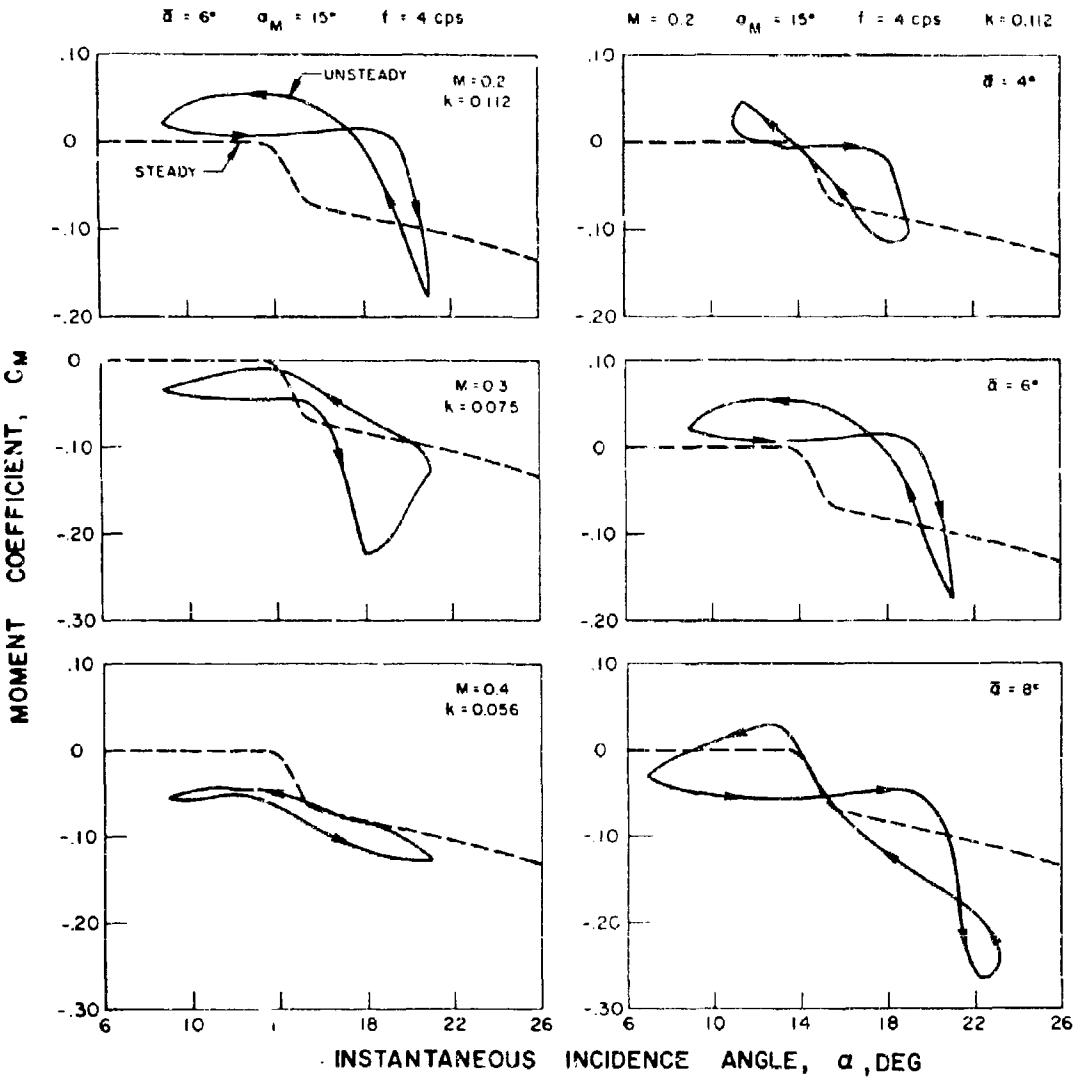

Figure 11. Effect of Mach Number and Pitch Amplitude on Moment Hysteresis Loops.

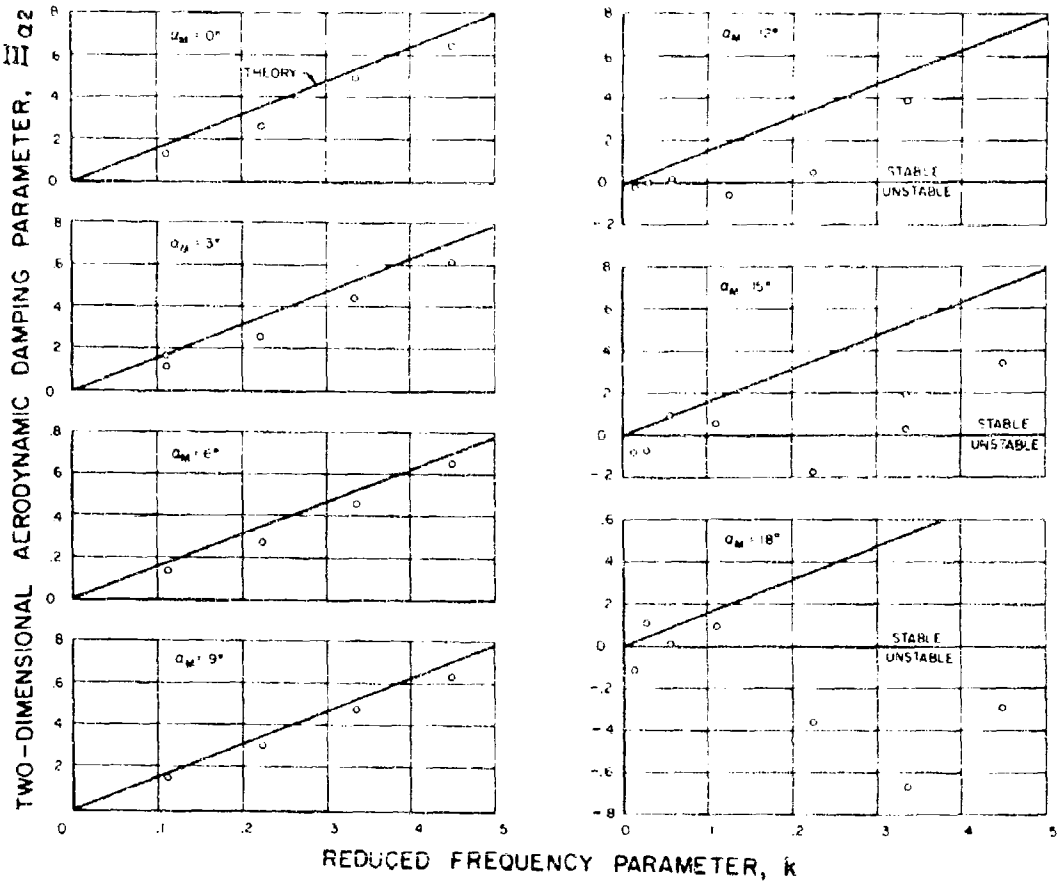

Figure 12. Variation of Two-Dimensional Aerodynamic Damping Parameter With Reduced Frequency and Mean Incidence Angle; $\bar{\alpha} = 6°$, M=.2.

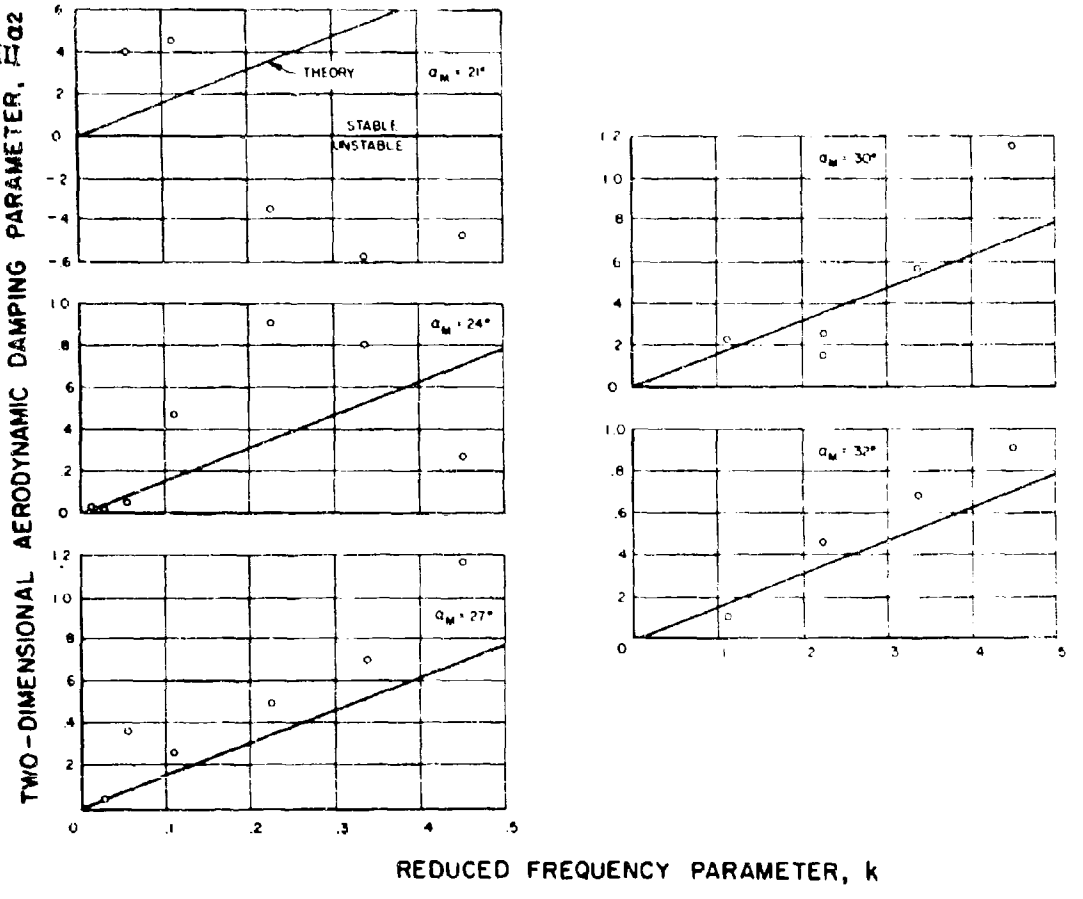

Figure 13. Variation of Two-Dimensional Aerodynamic Damping Parameter With Reduced Frequency and Mean Incidence Angle; $\bar{\alpha}$=6°, M=.2.

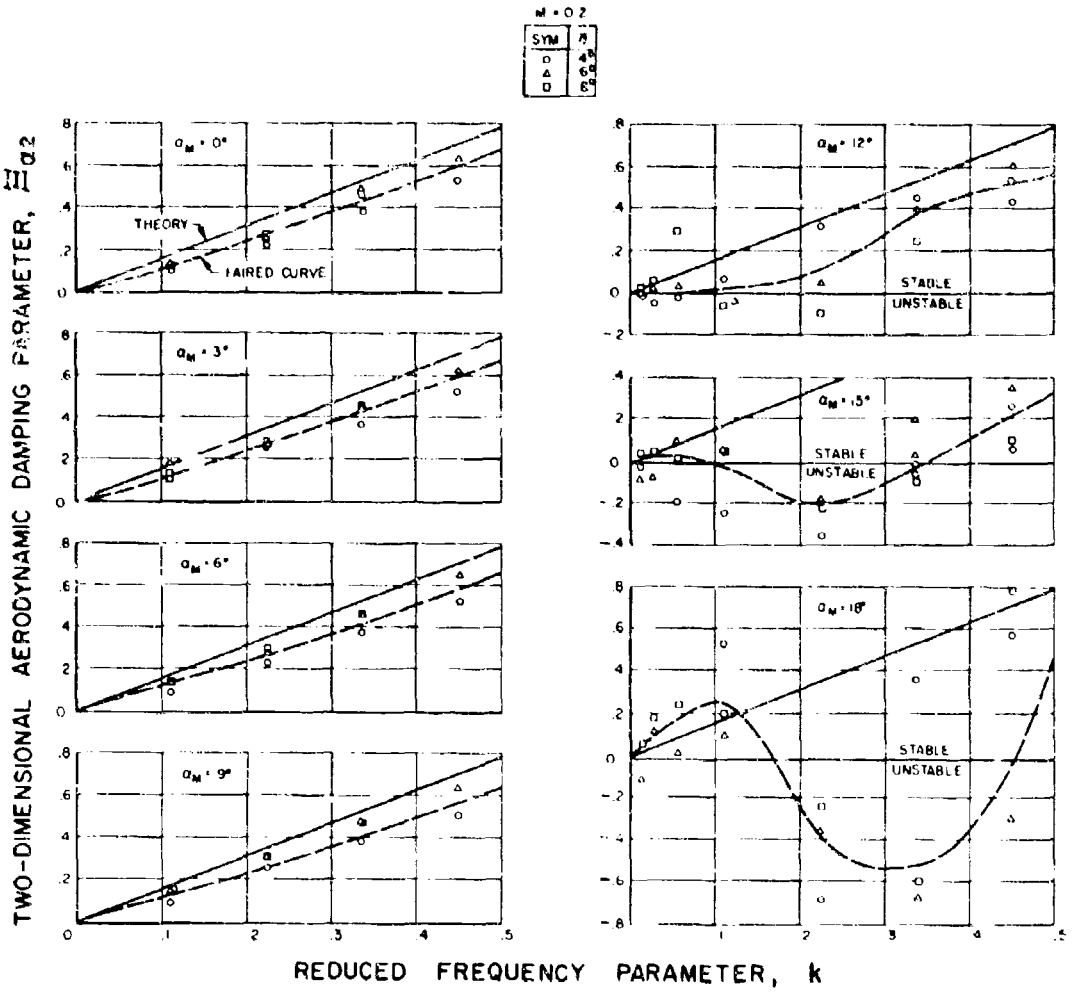

Figure 14. Variation of Two-Dimensional Aerodynamic Damping Parameter With Reduced Frequency and Mean Incidence Angle - Comparison of Theory and Smoothed Data.

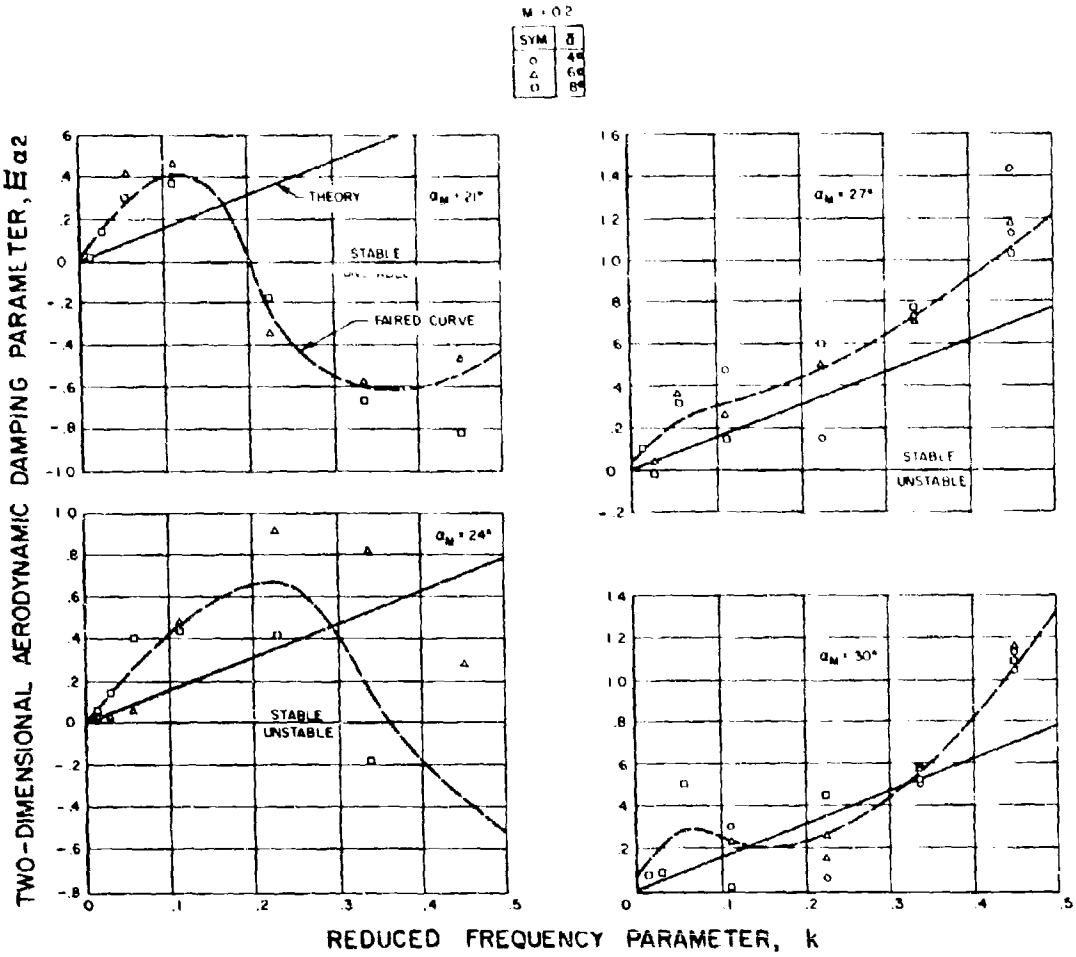

Figure 15. Variation of Two-Dimensional Aerodynamic Damping Parameter With Reduced Frequency and Mean Incidence Angle - Comparison of Theory and Smoothed Data.

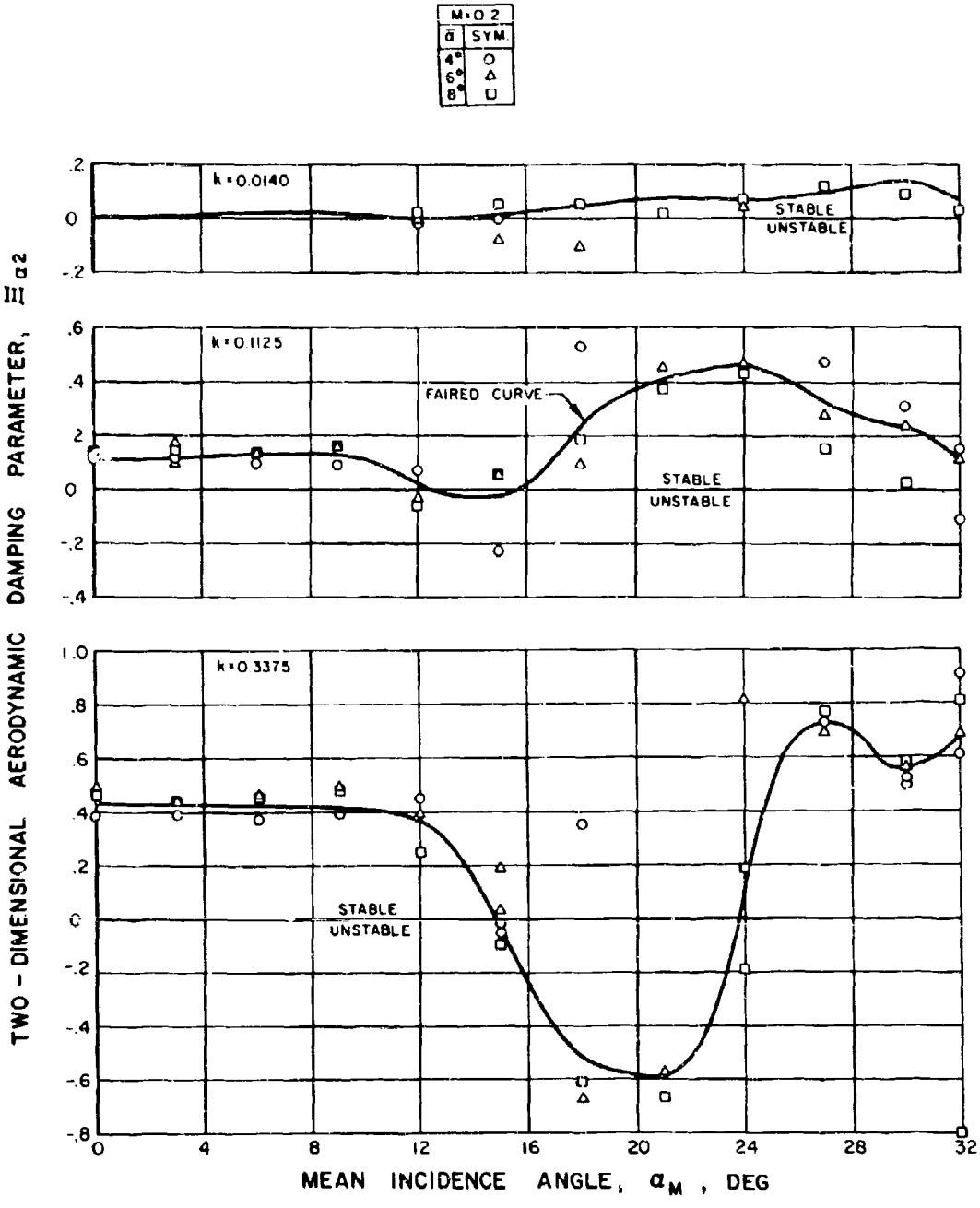

Figure 16. Representative Cross Plots of Smoothed Two-Dimensional Aerodynamic Damping Parameter.

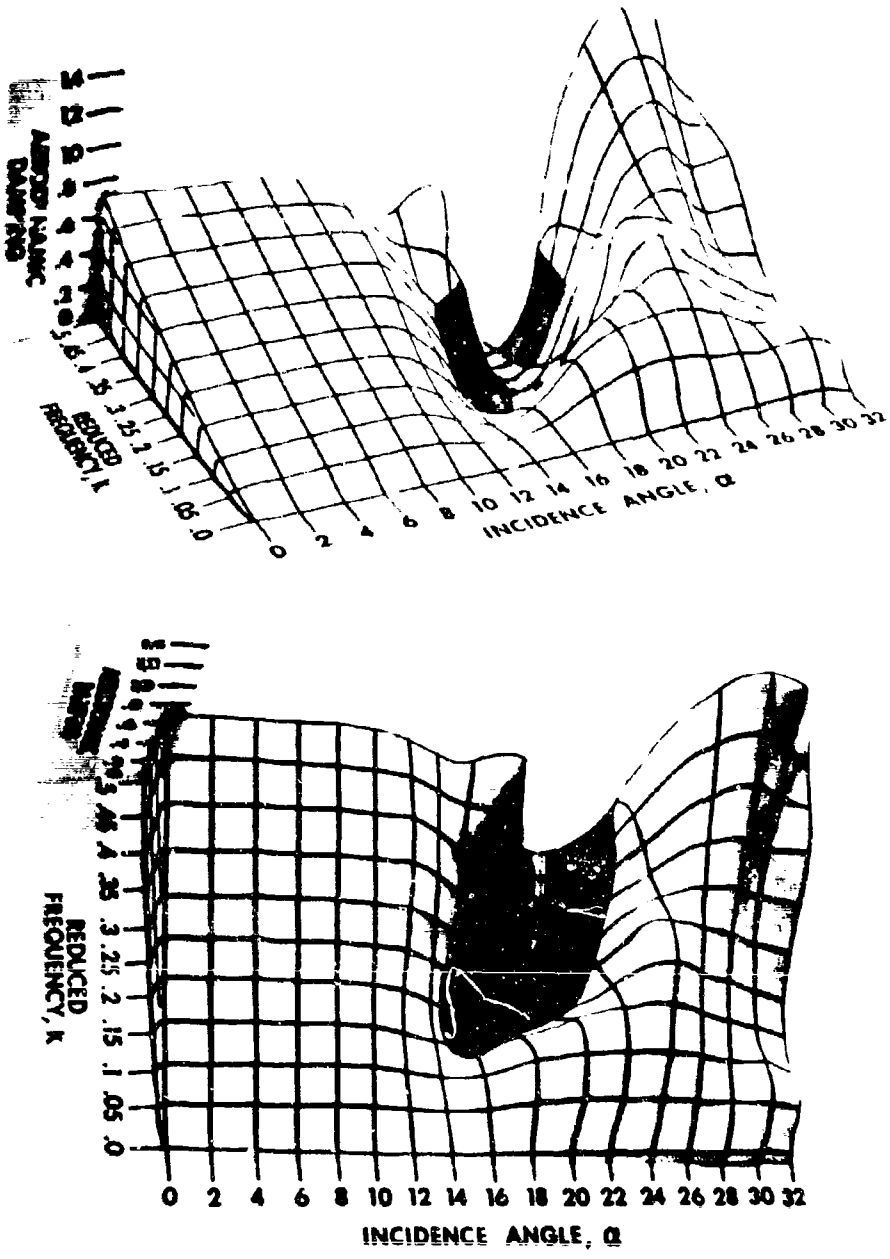

Figure 17. Two-Dimensional Aerodynamic Damping Surface for M = 0.2.

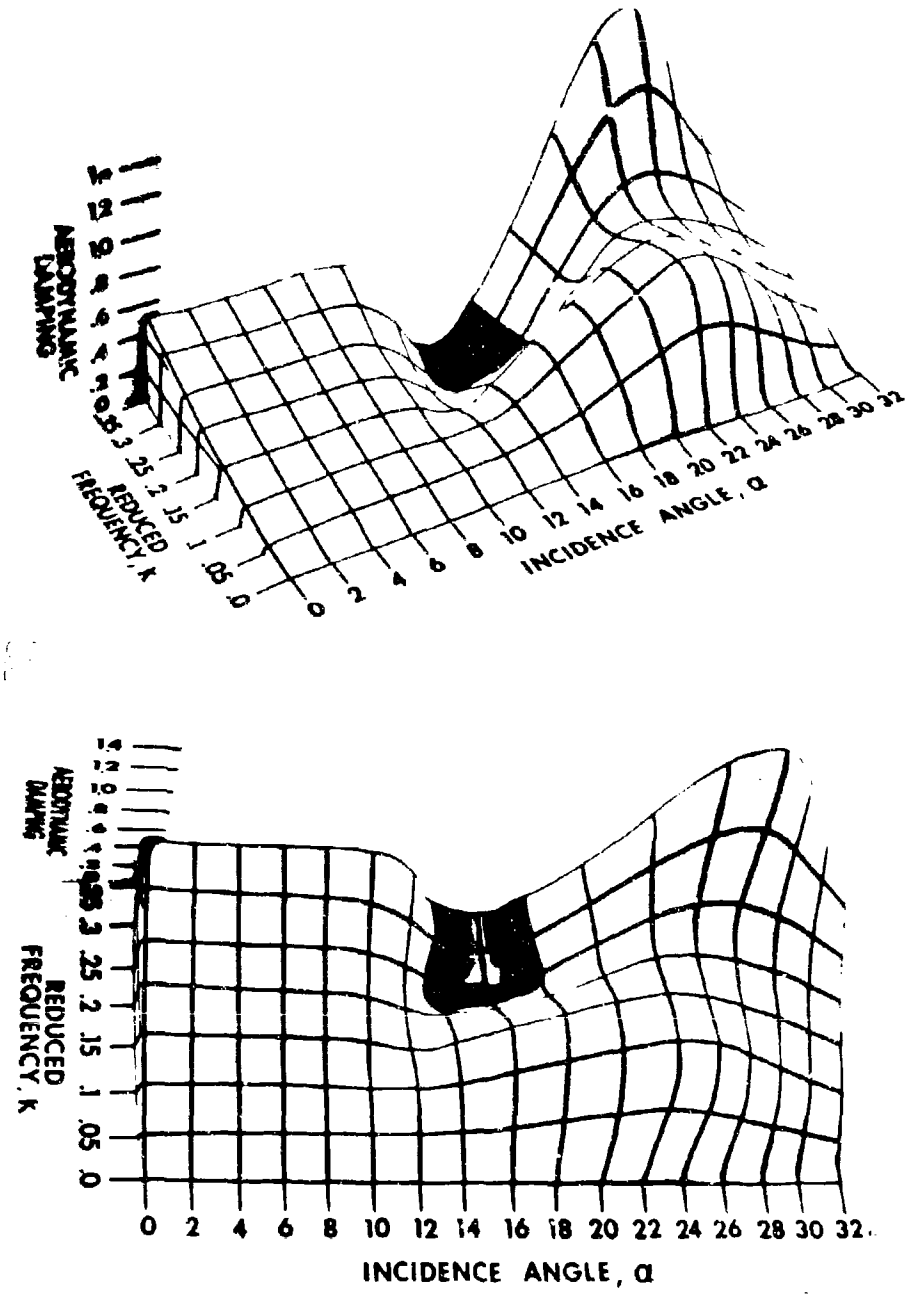

Figure 18. Two-Dimensional Aerodynamic Damping Surface for M = 0.3.

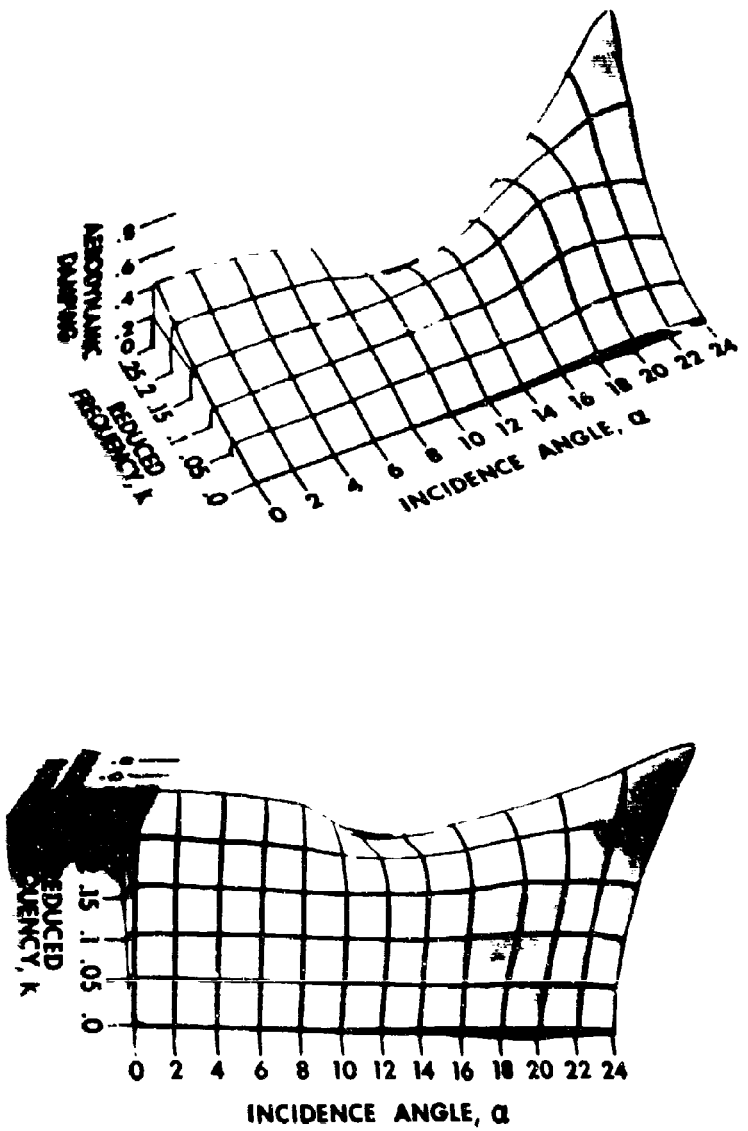

Figure 19. Two-Dimensional Aerodynamic Damping Surface for M = 0.4.

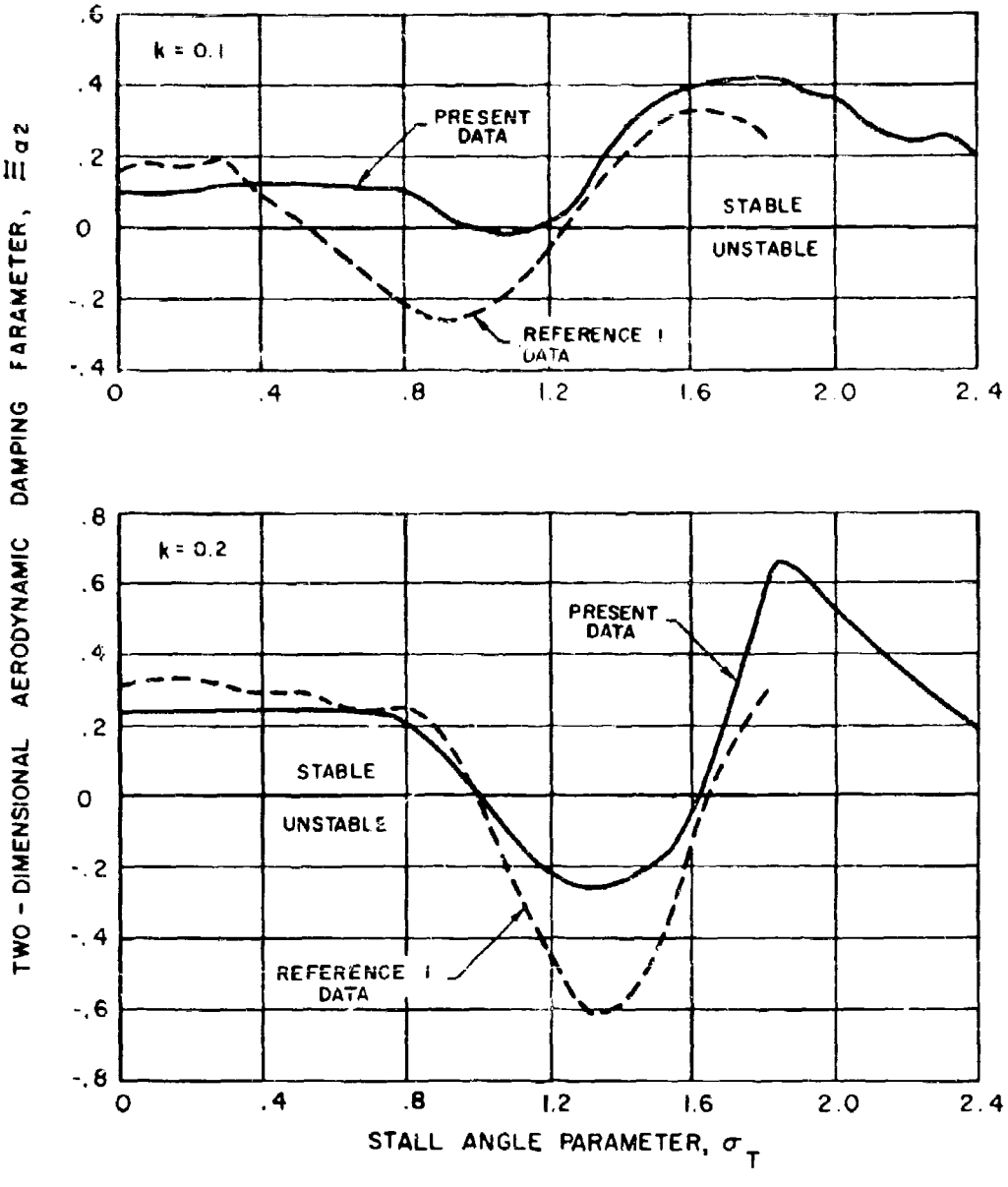

Figure 20. Comparison of Present Data and Reference 1 Data.

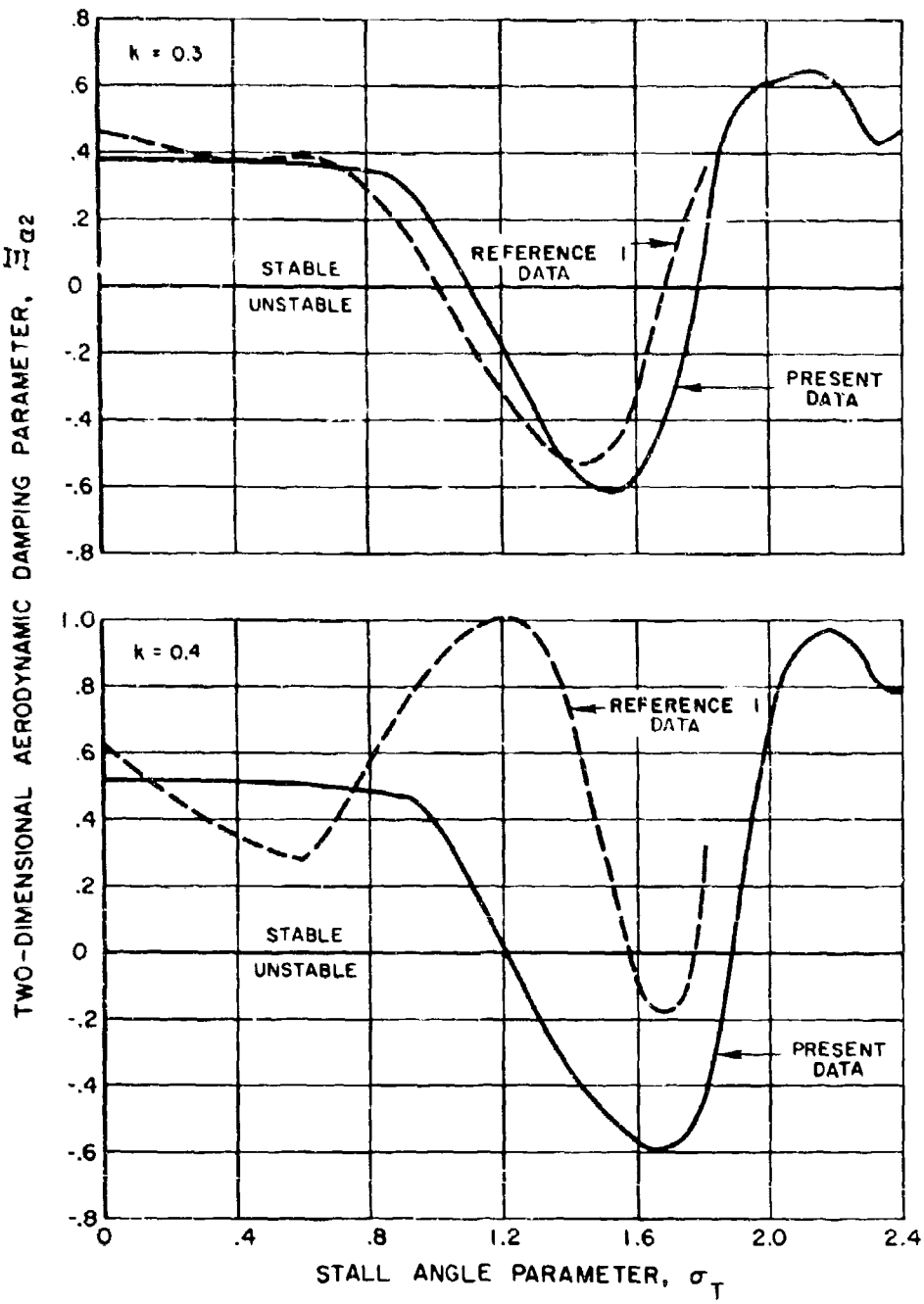

Figure 21. Comparison of Present Data and Reference 1 Data.

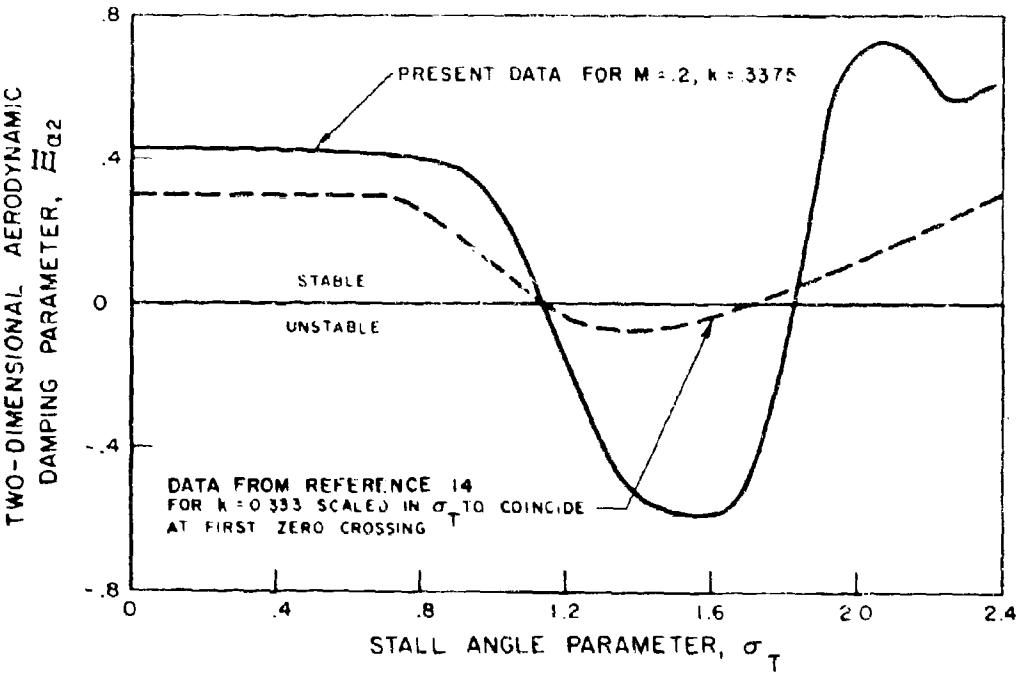

Figure 22. Comparison of Present Data and Reference 14 Data.

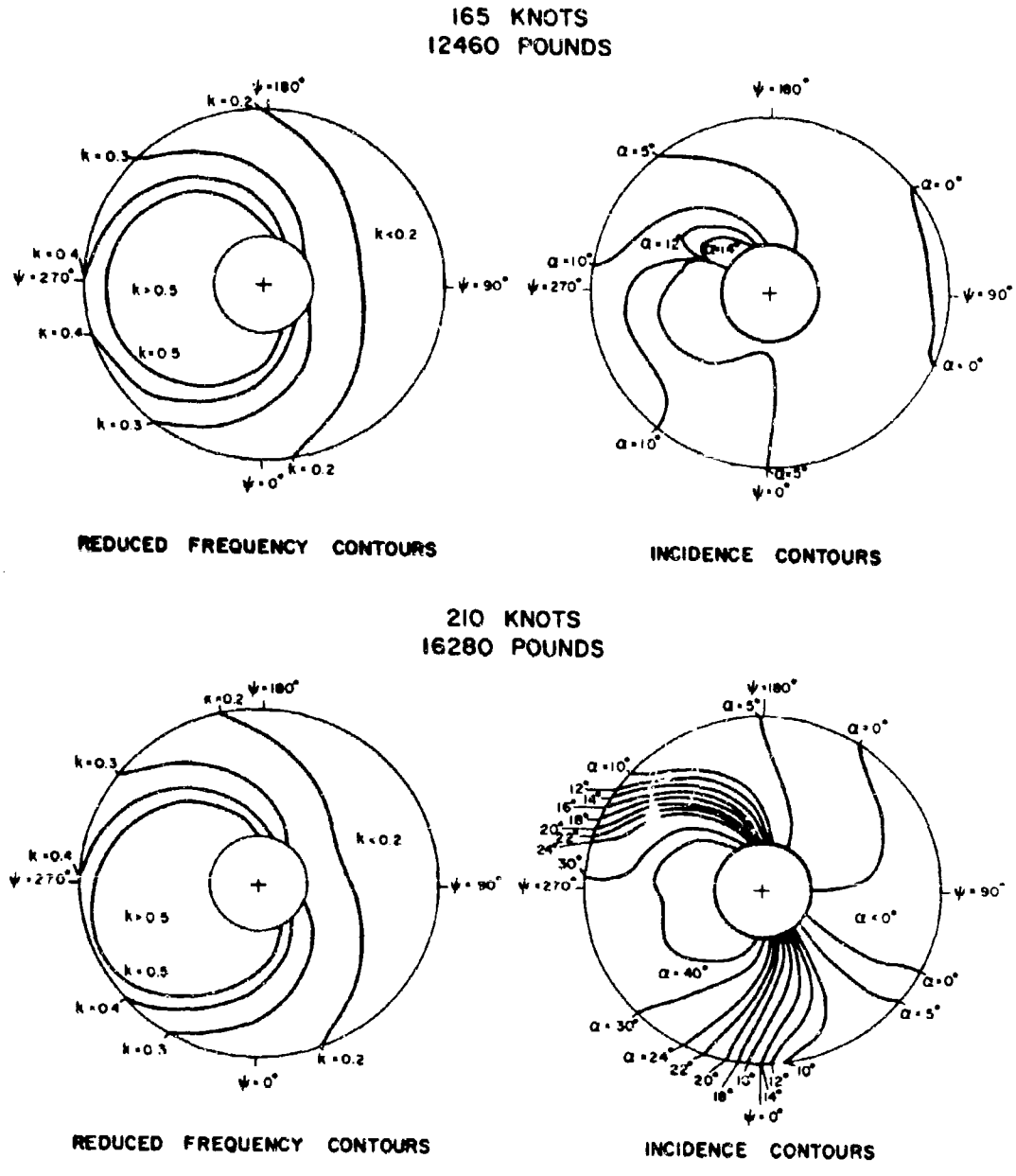

Figure 23. Polar Plots of Reduced Frequency Contours and Incidence Contours for S-61F Rotor.

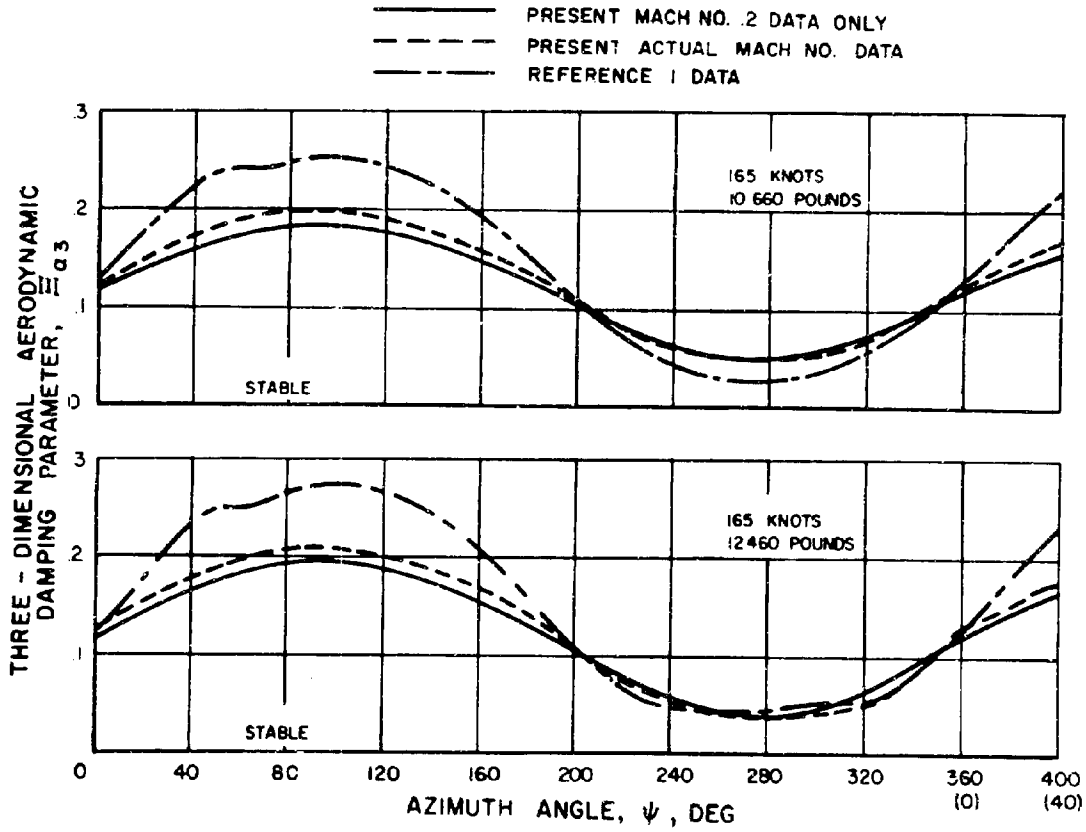

Figure 24. Variation of Aerodynamic Damping With Azimuth for an S-61F Rotor Blade.

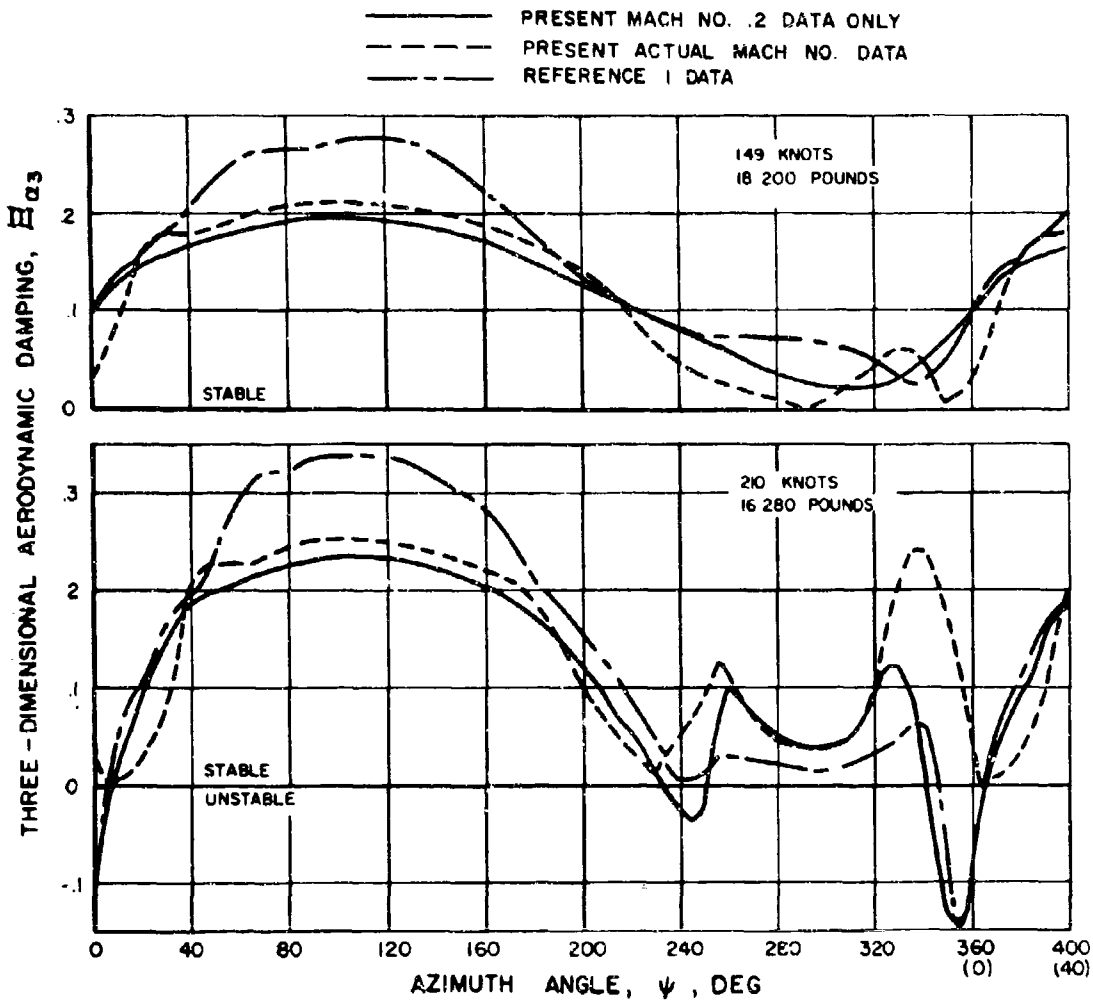

Figure 25. Variation of Aerodynamic Damping With Azimuth for an S-61F Rotor Blade.

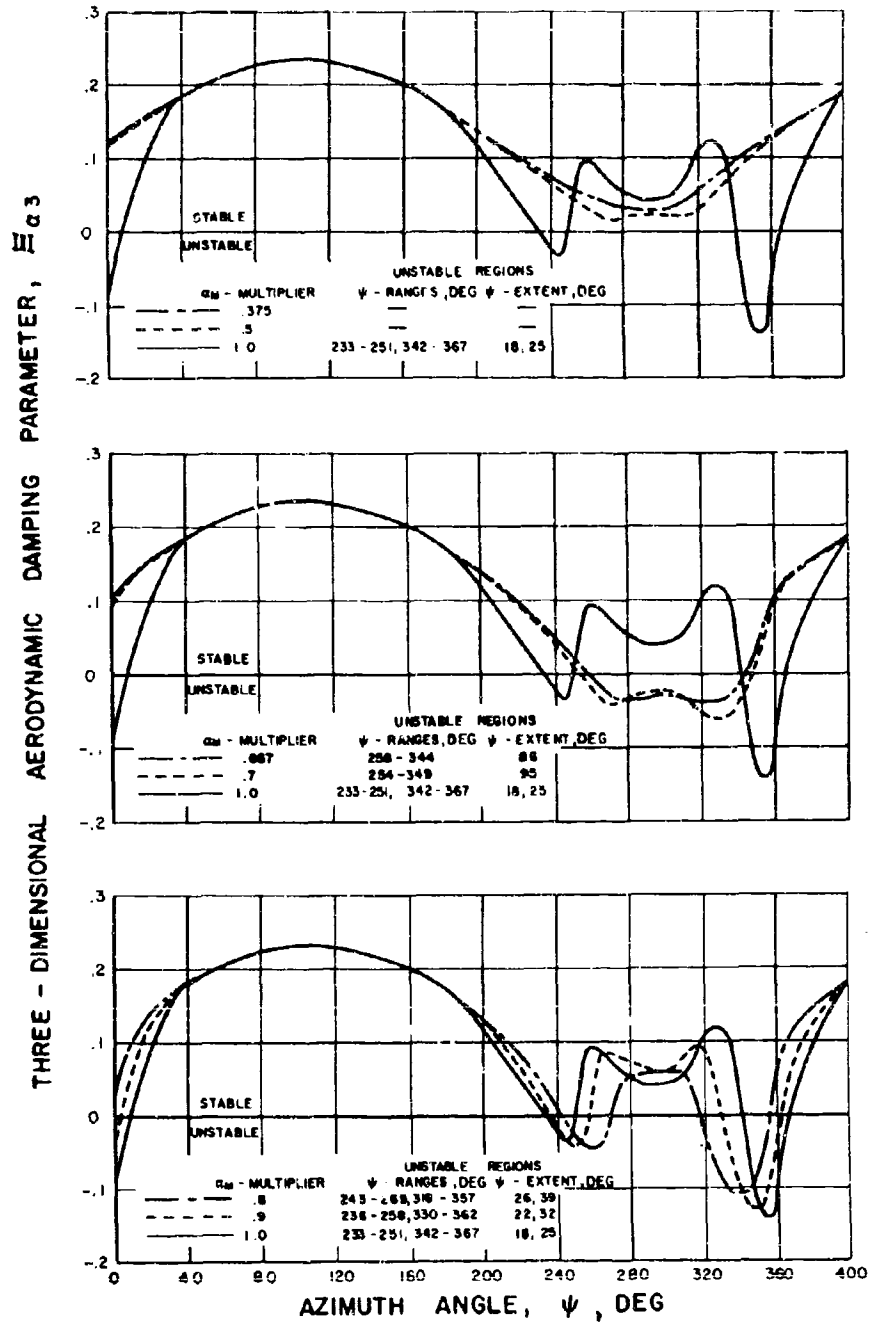

Figure 26. Effect of Incidence Angle Changes on Rotor Stability.

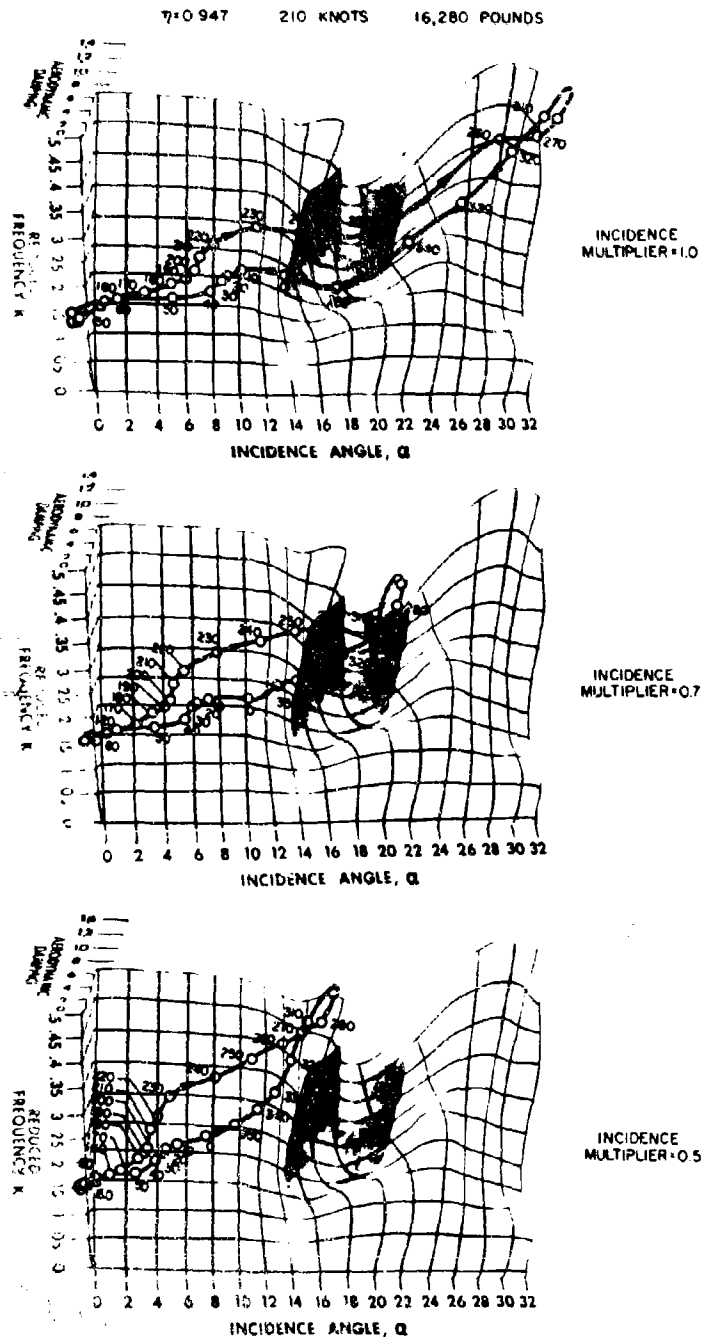

Figure 27. Reduced Frequency-Incidence Angle Trajectories for Various Loading Conditions on an S-61 Rotor Blade.

STALL FLUTTER FLIGHT CONDITION BOUNDARIES

PURPOSES AND METHODS

Upon completion of the stall flutter analysis described previously, it was recognized that stall flutter stability analyses for a more comprehensive set of rotor loading conditions were needed to provide some definition of those flight conditions which would be particularly troublesome from the standpoint of stall flutter.

The S-61 rotor was chosen as a medium for these additional studies, and the Normal Mode Transient Analysis was used to calculate required input data for the stability analysis. Rotor rotational tip speed was kept at 660 ft/sec. Rotor shaft angle was essentially zero, and uniform inflow was assumed. It should be noted that elastic blade deflections were included in the analyses. Rotor flapping was trimmed within 2 degrees for all cases, while collective pitch was changed to produce variations in rotor lift and torque. Advance ratios of .537, .473, .422, .381, .317, and .256 were chosen, corresponding to forward speeds of 210, 185, 165, 149, 124, and 100 knots respectively. At each advance ratio, from five to eight collective pitch settings were found which caused the rotor blade to be torsionally unstable for part of the azimuth, in addition to one or two which caused it to be completely stable. The Normal Mode Transient analysis provided azimuthal and radial variations in angle of the attack and Mach number for input to the stall flutter stability analysis described earlier. These data included elastic blade deformations due to inertial and quasi-steady aerodynamic forces, including stall and compressibility effects. The stability analysis program provided data such as that shown in Figures 24 through 26. The Sikorsky Aircraft test data for Mach number $M = 0.2$ were used, since these data were the most comprehensive and applicable. With reference again to Figure 25 as an example, the total number of degrees of azimuth for which negative three-dimensional aerodynamic damping existed was determined and designated ψ_{SF}. This was used as a parameter for measuring the intensity of stall flutter. With the present analysis, this would seem to be the most suitable parameter for judging the severity of stall flutter.

RESULTS

The total unstable stall flutter azimuth range ψ_{SF} was plotted against rotor lift coefficient solidity ratio C_L/σ for the advance ratios .537, .473, and .422. These plots are shown in Figure 28. Note that these graphs define the parameter ψ_{SF} as a single-valued function of C_L/σ for each advance ratio. Unfortunately, similar relationships were not generally obtained for the lower three advance ratios. It was found instead that a range of values of ψ_{SF} were possible for a given value of C_L/σ. For this reason, plots of the form shown in Figure 28 could not be provided for the advance ratios .381, .317 and .256. However, the results shown in Figure 28 were cross-plotted as shown in Figure 29, to produce boundaries on a C_L/σ versus μ plane, as originally intended.

In order to produce flight condition boundaries which would include the lower advance ratios, some other rotor performance parameter was needed, and the rotor torque coefficient-solidity ratio was chosen for this purpose. Figure 30 was therefore prepared from the previously calculated data. The corresponding cross plot is shown in Figure 31.

DISCUSSION

One of the basic aspects of flutter on helicopter blades in forward flight is its dependence on quantities which change with azimuth angle. This is particularly true of stall flutter, which tends to occur on the retreating blade side of the rotor disc, since angles of attack beyond stall occur there. Thus, as would be expected, the stall flutter analysis predicts a limited azimuthal range of instability. It would be expected in practice that blade torsional vibrations would increase while in the unstable region and decrease or damp out while in the stable azimuthal region. Therefore,it is obvious to expect that the torsional amplitude reached and the number of cycles of significant torsional amplitudes would grow with the azimuthal range of instability. This range of instability is conveniently obtained from the present stall flutter analysis. More elaborate parameters might be proposed for use with the data in their present form, such as an integral of work done on the blade by the aerodynamic torsional couples as the blade vibrates continuously at some nominal amplitude and traverses the region or regions of instability. In view of the limited range of data available, the selection of the extent of the total azimuthal range of instability as a parameter is appropriate.

The curves on Figure 29 define values of rotor lift coefficient for which the stability analysis predicts various amounts of unstable azimuth range. At a given advance ratio, increasing rotor lift from the stable region first causes a small region of instability over a range of azimuth angles on the retreating blade. This area increases in extent with rotor lift, until the blade angles of attack reach high enough values to enter another area of stability. The region of instability then splits into two smaller regions, which diminish in size and grow farther apart in azimuth as rotor lift increases. These observations are illustrated by Figures 24 through 27 and in the corresponding earlier discussion. Note that the boundary segments which are below the maximum value of ψ_{SF} at each advance ratio on Figure 29 correspond generally to a continuous region of instability, and will probably cause the highest torsional amplitudes.

It is of particular interest to compare Figure 29 with a chart of a similar type appearing as Figure 12 in Reference 2. The slender region $\psi_{SF} = 100^{\circ}$ on Figure 29 approximates an extrapolation of the points plotted for the full-scale H-21 test on Figure 12 of Reference 2.

The practical significance of the boundaries on Figure 29 will be discussed next. Since the S-61 rotor torsional natural frequency and the expected stall flutter frequency are about 8 cycles per revolution, each period of torsional vibration at its normal tip speed is represented by about 45 degrees of azimuth. Some judgement is required in order to stipulate how many cycles of instability are required to produce troublesome amounts of

torsional vibration. Comparison with the above results of Reference 2 would suggest that at least two cycles of instability, or $\psi_{sf} \cong 90°$, are required.

The largest values of ψ_{sf} obtained at the lower three advance ratios (μ = .381, .317, and .256) occurred at values of C_L/σ, which were practically coincident with the test values for the H-21 rotor on Figure 12, Reference 2, which was mentioned earlier. The values of ψ_{sf} were 120°, 130°, and 140°, respectively. It was found, however, that ψ_{sf} could vary widely with little or no change in C_L/σ because of heavy rotor stalling. Thus, the trimmed rotor could be operated at advance ratios and lift coefficients close to those given above with very little stall flutter instability. The occurrence of stall flutter was found to be more the result of extensive blade stalling than the result of attainment of a particular value of rotor lift.

Since the occurrence of blade stall is accompanied by a rapid rise in blade section drag, it was suspected that rotor torque would provide a more definitive indication of conditions for stall flutter. This proved to be the case, and Figures 30 and 31 show the resulting boundaries. It will be noted that the lower boundaries occur at a fairly constant torque level as advance ratio is varied.

The calculation of a few rotor loading cases for the untrimmed rotor and for shaft angles other than zero showed that the stall flutter boundaries will be moderately affected, although no particular trends could be defined.

The radial and azimuthal distribution of angle of attack would, of course, be somewhat different if nonuniform inflow were used in place of the assumed uniform inflow. Usually, the inclusion of nonuniform inflow tends to reduce angles of attack on the retreating blades; hence, the boundaries presented would probably be shifted upward somewhat.

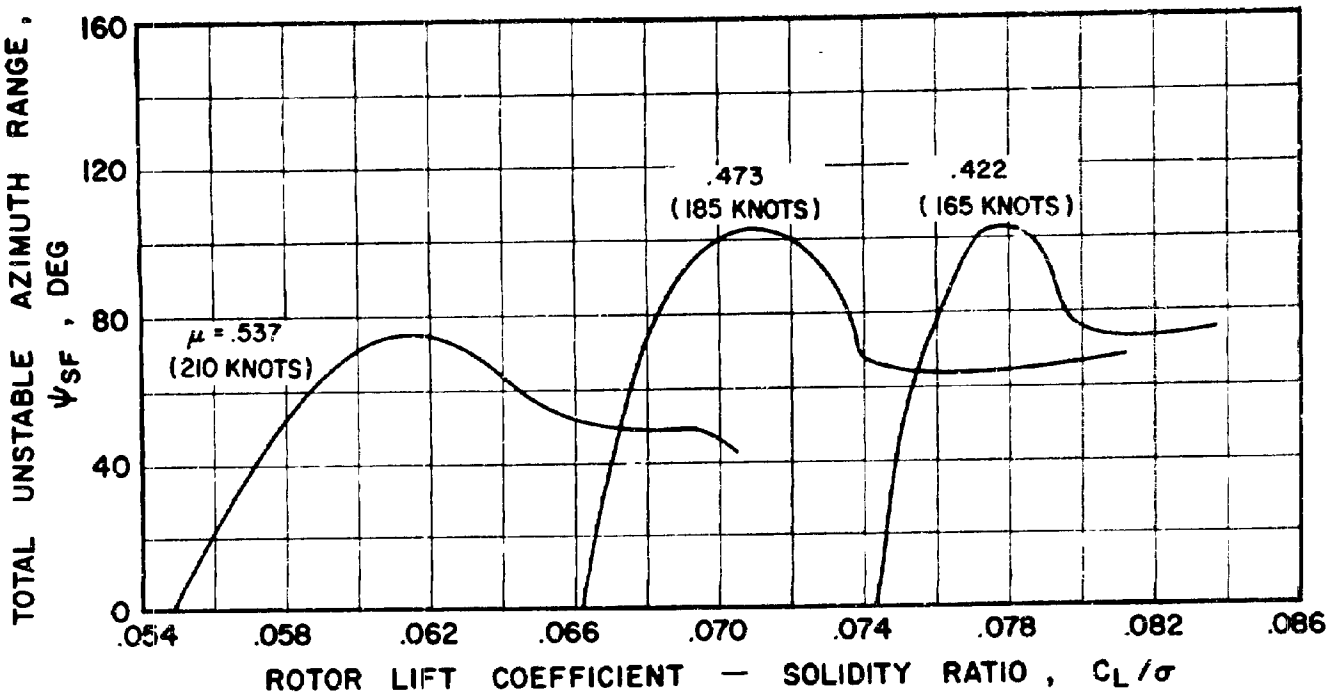

Figure 28. Effect of Rotor Lift Coefficient on Stall Flutter at Various Advance Ratios, S-61 Rotor; $\Omega R = 660$ FT/SEC, $a_s = 0°$, $a_{is} = 0°$, $b_{is} = 0°$

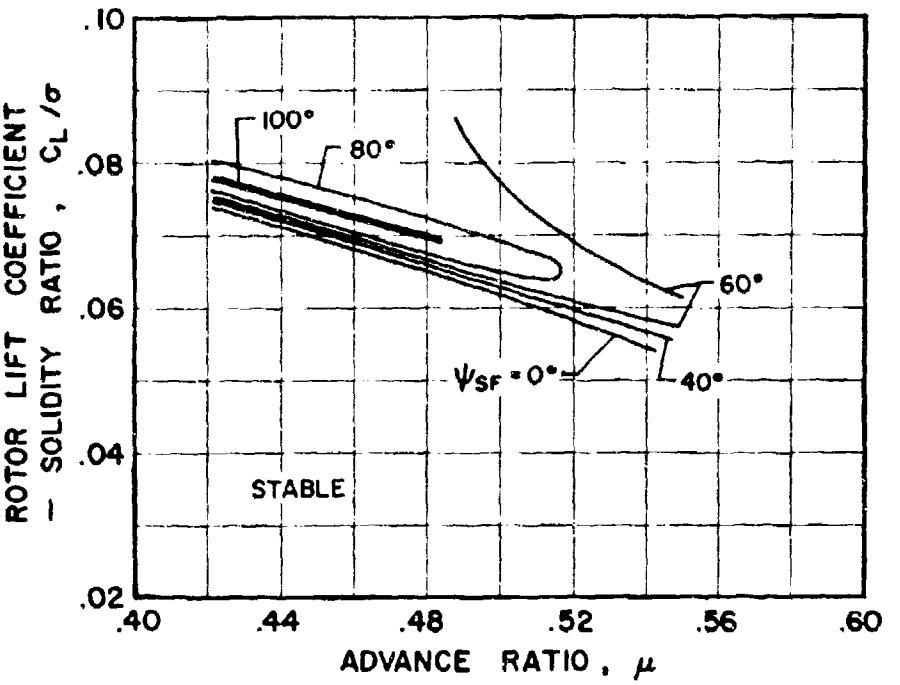

Figure 29. Stall Flutter Boundaries Related to Rotor Lift Coefficient and Advance Ratio; S-61 Rotor, ΩR =660 FT/SEC, a_s =0°, a_{1s} = 0°, b_{1s}=0°

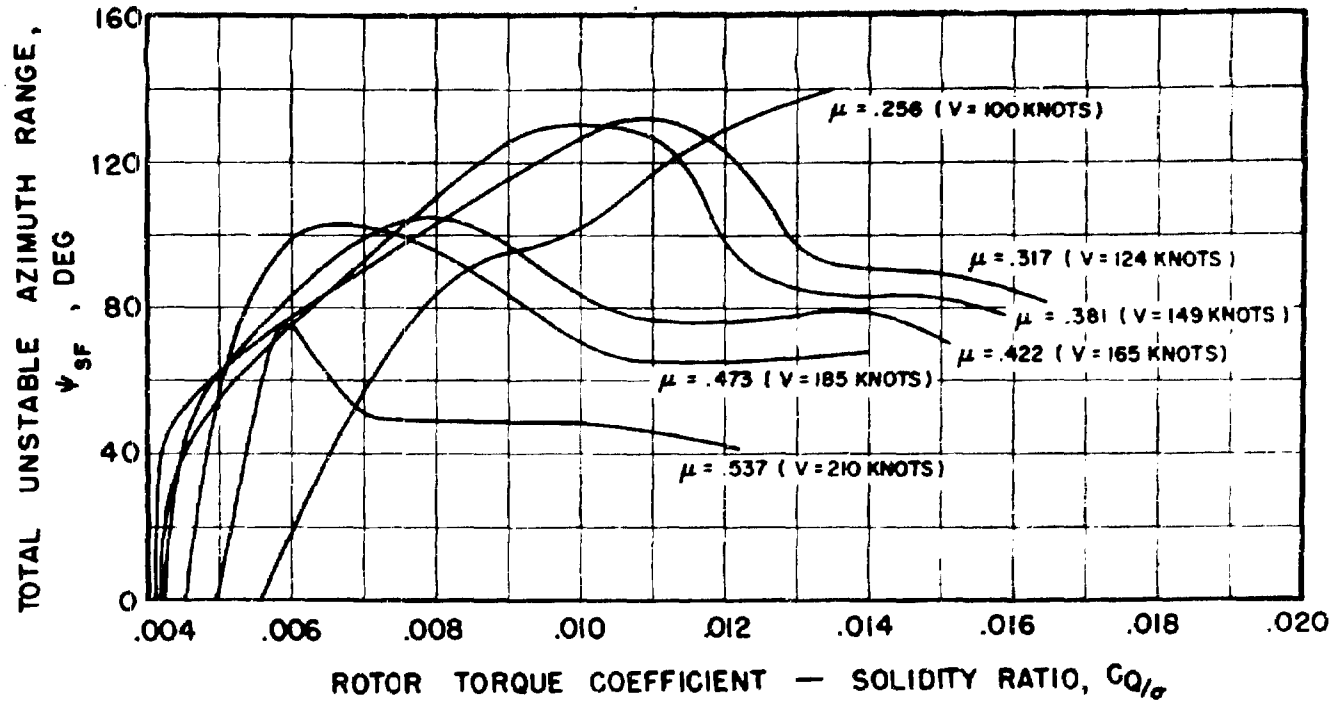

Figure 30. Effect of Rotor Torque Coefficient on Stall Flutter at Various Advance Ratios; S-61 Rotor, ΩR = 660 FT/SEC, a_s = 0°, a_{1s} = 0°, b_{1s} = 0°

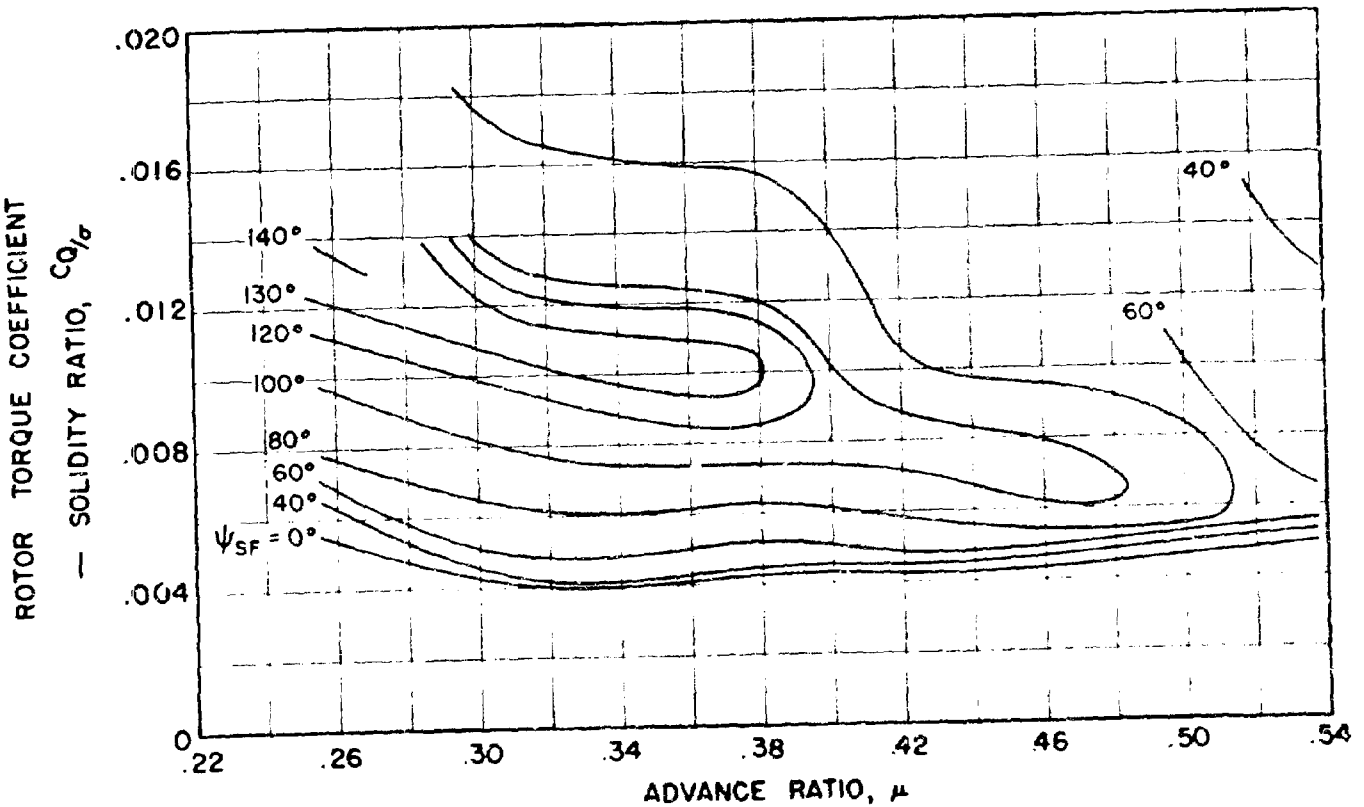

Figure 31. Stall Flutter Boundaries Related to Rotor Torque Coefficient and Advance Ratio; S-61 Rotor, $\Omega R = 660$ FT/SEC, $a_S = 0°$, $a_{1S} = 0°$, $b_{1S} = 0°$

CONCLUSIONS

1. The measured values of two-dimensional aerodynamic damping parameter in pitch, $-\pi\alpha_2$, are in good agreement with potential flow theory for low mean incidence angles, $\alpha_M \leq 9^\circ$, and depart from the theory for $\alpha_M \geq 12^\circ$.

2. At high incidence angles, $\alpha_M \geq 12^\circ$, the damping parameter in pitch decreases to negative or unstable levels; it then increases to positive values again if the mean incidence angle is increased enough. This is true unless the reduced frequency k is smaller than about .15.

3. The Reference 1 data and the present data are in generally good agreement over a substantial range of both k and α_M . Both sets of data predict essentially the same two-dimensional stability boundary at moderate values of k .

4. The available data corresponding to M = 0.2 are adequate for the analysis of contemporary rotor systems. More extensive ranges of reduced frequency and angle of attack data are needed at other Mach numbers.

5. The results of the stability analysis for the S-61 rotor are in good agreement with those of Reference 2.

6. Use of the Reference 1 data yields slightly larger blade damping for the advancing blade but produces good agreement with the present data for the retreating blade, even when instability is present.

7. The rotor lift coefficient-solidity ratio is a suitable parameter for definition of stall flutter boundaries at advance ratios of .42 and above.

8. The rotor torque coefficient-solidity ratio is a suitable parameter for definition of stall flutter boundaries for all advance ratios.

RECOMMENDATIONS

1. The existing data described in this report are adequate for contemporary rotors and operating conditions. As rotorcraft forward speeds increase, it is evident that a much larger range of data will be needed, including data for a simulated reverse-flow region.

2. The analysis described in this report is based on the calculation of torsional work for a hypothetical cycle of torsional vibration which takes place at a number of discreet azimuth locations. On the actual rotor, the azimuth angle and therefore the mean angle of attack and relative velocity changes continuously during the torsional vibration cycle. In future stall flutter analysis and testing, consideration should be given to the time history of the large variations in relative velocity and mean angle of attack that are actually taking place during a cycle of torsional vibration.

REFERENCES CITED

1. Halfman, Robert L., Johnson, H. C., and Haley, S. M., Evaluation of High-Angle-of-Attack Aerodynamic-Derivative Data and Stall-Flutter Prediction Techniques, NACA Technical Note TN 2533, National Advisory Committee for Aeronautics Washington D. C., November 1951.

2. Ham, Norman D., and Young, Maurice J., Torsional Oscillation of Helicopter Blades Due to Stall, Journal of Aircraft Vol. 3, No. 3, May-June 1966, pp. 218-224.

3. Clarke, A. E., Recent Work at the Royal Aircraft Establishment on Helicopter Dynamic Loads, With Particular Reference to High Blade Incidence Problems, Proceedings of the CAL/TRECOM Symposium on Dynamic Loads Associated with Helicopters and V/STOL Aircraft, Buffalo, New York, June 1963.

4. Ham, Norman D., An Experimental Investigation of Stall Flutter, IAS Paper No. 61-28, presented at the IAS 29th Annual Meeting, New York, January 1961. (Also appeared in the Journal of the American Helicopter Society, Vol. 7, January 1962, pp. 3-16.)

5. Woolston, D. S., and Runyan, H. L., Some Considerations on the Air Forces on a Wing Oscillating Between Two Walls for Subsonic Compressible Flow, Journal of the Aeronautical Sciences, Vol. 22, No. 1, January 1955, pp. 41-50.

6. Postel, E. E., and Leppert, E. L., Jr., Theoretical Pressure Distribution for a Thin Airfoil Oscillating in Incompressible Flow, Journal of the Aeronautical Sciences, Vol. 15, No. 8, August 1948, pp. 486-492.

7. Theodorsen, Theodore, General Theory of Aerodynamic Instability and the Mechanism of Flutter, NACA Report 496, National Advisory Committee for Aeronautics Langley Field Virginia, May 2, 1934.

8. Scanlan, Robert H., and Rosenbaum, Robert, Introduction to the Study of Aircraft Vibration and Flutter, The MacMillan Company, New York, 1951.

9. Bratt, J. B., and Wight, K. C., The Effect of Mean Incidence, Amplitude of Oscillation, Profile, and Aspect Ratio on Pitching Moment Derivatives, Great Britain ARC R&M No. 2064, Aeronautical Research Council, Great Britain, June 1945.

10. Victory, Mary, Flutter at High Incidence, Great Britain ARC R&M No. 2048, Aeronautical Research Council, Great Britain, January 1943.

11. Bratt, J. B., and Scruton, C., Measurements of Pitching Moment Derivatives for an Aerofoil Oscillating About the Half-Chord Axis, Great Britain ARC R&D No. 1921, Aeronautical Research Council Great Britain, November 1938.

12. Rainey, A. Gerald, Preliminary Study of Some Factors Which Affect the Stall-Flutter Characteristics of Thin Wings, NACA Technical Note TN 3622, National Advisory Committee for Aeronautics Langley Field, Virginia, March 1956.

13. Bisplinghoff, Raymond L., Ashley, Holt, and Halfman, Robert L., Aeroelasticity, Addison - Wesley Publishing Company, Inc., Reading, Massachusetts, 1955.

14. Regier, Arthur A., and Rainey, A. Gerald, Effect of Mean Incidence on Flutter, Paper presented at the 7th Meeting of AGARD Structures and Materials Panel, Rome, Italy, March 1958.

15. Schnittger, Jan R., Single Degree of Freedom Flutter of Compressor Blades in Separated Flow, Journal of the Aeronautical Sciences, Vol. 21, No. 1, January 1954, pp. 27-36.

APPENDIX I
TWO DIMENSIONAL UNSTEADY MOMENT FORMULATION

In the following analysis, it is assumed that the two-dimensional airfoil section is executing a single-degree-of-freedom torsional motion about a pivot axis at a . This motion is assumed to have a torsional amplitude, $\bar{\alpha}$, and a torsional frequency, $\omega = 2\pi f$. (As stated earlier in the main body of this report, complex quantities will be denoted by an asterisk superscript, and amplitudes of sinusoidal functions will be denoted as barred quantities, such as $\bar{\alpha}$.)

The complex, unsteady, total twisting moment M^*_{TOT} experienced by the airfoil about its pivot axis will consist of the sum of the steady mean moment M_M associated with the mean incidence angle α_M and the unsteady moment M^*_U associated with the torsional displacement relative to the mean incidence angle α^*

$$M^*_{TOT} = M_M + M^*_U \tag{67}$$

A convenient expression for the unsteady moment due to a single-degree-of-freedom torsional motion about a pivot axis at a is given in References 8 and 13 as

$$M^*_U = \pi\rho b^4\omega^2\left[M_\alpha - \left(L_\alpha + M_h\right)\left(\frac{1}{2}+a\right) + L_h\left(\frac{1}{2}+a\right)^2\right]\bar{\alpha}\,e^{i\omega t} \tag{68}$$

In Eq. (68), the quantities L_h , L_α , M_h , M_α are unsteady lift and moment functions which may be taken from any convenient theoretical or empirical source, and the unsteady torsional displacement has been written in terms of the torsional amplitude as

$$\alpha^* = \bar{\alpha}\,e^{i\omega t} \tag{69}$$

The moment coefficient will be defined by the general equation

$$C_M = \frac{M}{\frac{1}{2}\rho U^2(2b)^2} \tag{70}$$

and after a bit of manipulation, Eq. (68) becomes

$$C^*_{M_U} = \frac{\pi k^2}{2}\left[M_\alpha - \left(L_\alpha + M_h\right)\left(\frac{1}{2}+a\right) + L_h\left(\frac{1}{2}+a\right)^2\right]\bar{\alpha}\,e^{i\omega t} \tag{71}$$

This formulation will be returned to later. Initially, though, the analysis will proceed in a more general fashion, beginning with the coefficient form of Eq. (67),

$$C^*_{M_{TOT}} = C_{M_M} + C^*_{M_U} \tag{72}$$

and if it is assumed that the unsteady moment coefficient is a periodic function, it may be written as

$$C^*_{M_U} = \bar{C}^*_{M_U} e^{i\omega t} \tag{73}$$

where the amplitude $\bar{C}^*_{M_U}$ is still regarded as a complex quantity to account for the phase shift between torsional displacement and moment response. Thus, Eq. (72) becomes

$$\begin{aligned} C^*_{M_{TOT}} &= C_{M_M} + \bar{C}^*_{M_U} e^{i\omega t} \\ &= C_{M_M} + \left(\bar{C}_{M_{UR}} + i\bar{C}_{M_{UI}}\right) e^{i\omega t} \end{aligned} \tag{74}$$

and in terms of the notation of Eq. (71), the real and imaginary parts are given by

$$\bar{C}_{M_{UR}} = \frac{\pi k^2}{2}\left[M_{aR} - \left(L_{aR} + M_{hR}\right)\left(\frac{1}{2} + a\right) + L_{hR}\left(\frac{1}{2} + a\right)^2\right]\bar{\alpha} \tag{75}$$

$$\bar{C}_{M_{UI}} = \frac{\pi k^2}{2}\left[M_{aI} - \left(L_{aI} + M_{hI}\right)\left(\frac{1}{2} + a\right) + L_{hI}\left(\frac{1}{2} + a\right)^2\right]\bar{\alpha} \tag{76}$$

It is convenient at this point to derive the expression which was used to provide the unsteady theoretical moment loops shown in Figure 10. To do this, the condition of 25% chord pivot will be imposed on Eqs. (74), (75) and (76), whereupon the mean moment vanishes, $C_{M_M} = 0$, as does the factor $1/2 + a = 0$. Then, substitution of Eqs. (75) and (76) into Eq. (74) and expansion of the exponential factor yields the equation

$$C^*_{M_{TOT}} = \frac{\pi}{2} k^2 (M_{aR} + iM_{aI})(\cos\omega t + i \sin\omega t)\bar{\alpha} \tag{77}$$

which has a real part given by

$$C_{M_{TOT_R}} = \frac{\pi}{2} k^2 (M_{\alpha R} \cos \omega t - M_{\alpha I} \sin \omega t) \bar{\alpha} \tag{78}$$

The time variable in Eq. (78) may be eliminated by manipulating the expression for the total incidence angle, which consists of the sum of the mean incidence angle, α_M , and the torsional displacement relative to the mean incidence angle, α^* , or, by using Eq. (69),

$$\alpha^*_{TOT} = \alpha_M + \alpha^* = \alpha_M + \bar{\alpha} e^{i\omega t} \tag{79}$$

The real part of Eq. (79) is given by

$$\alpha_R = \alpha_M + \bar{\alpha} \cos \omega t \tag{80}$$

which may be solved for $\cos \omega t$ as

$$\cos \omega t = \frac{\alpha_R - \alpha_M}{\bar{\alpha}} \tag{81}$$

Use of the well-known trigonometric identity relating $\sin^2 \omega t$ and $\cos^2 \omega t$ yields

$$\sin \omega t = \pm \frac{1}{\bar{\alpha}} \sqrt{\bar{\alpha}^2 - (\alpha_R - \alpha_M)^2} \tag{82}$$

and substitution of Eqs. (81) and (82) into Eq. (78) leads to the result

$$C_{M_{TOT_R}} = \frac{\pi}{2} k^2 \left[M_{\alpha R} (\alpha_R - \alpha_M) \pm M_{\alpha I} \sqrt{\bar{\alpha}^2 - (\alpha_R - \alpha_M)^2} \right] \tag{83}$$

which is valid for an airfoil oscillating in pitch about its 25% chord. For use elsewhere in this report in comparing theory with experiment, the function M_α may be specialized to the case of an incompressible, potential flow past the airfoil (Reference 8)

$$M_\alpha = \frac{3}{8} - \frac{i}{k} \tag{84}$$

whereupon Eq. (83) reduces to the form

$$C_{M_{TOT_R}} = \frac{\pi k}{2}\left[\frac{3}{8}k\,(\alpha_R-\alpha_M) \pm \sqrt{\bar{a}^2-(\alpha_R-\alpha_M)^2}\right] \tag{85}$$

In this equation, the negative sign is associated with increasing α_R , and the positive sign with decreasing α_R .

APPENDIX II
DERIVATION OF THREE-DIMENSIONAL DAMPING EQUATION

The equations necessary to determine the three-dimensional aerodynamic damping will now be derived. Use will be made of the formulation presented on page 210 of Reference 8, with the notation altered to conform with present usage. As in Reference 8, the development begins with the relations for the virtual work due to a torsional displacement,

$$\delta W = M_{U_2}^{*/} \delta \bar{\alpha}(r) = \left(\frac{M_{U_2}^{*}}{r_T - r_0}\right) f_\alpha(r)\, \delta \bar{\alpha}_T \tag{86}$$

where

$$M_{U_2}^{*/} = \frac{M_{U_2}^{*}}{r_T - r_0} \tag{87}$$

is the unsteady moment per unit span and

$$\bar{\alpha}(r) = f_\alpha(r)\, \bar{\alpha}_T \tag{88}$$

is the spanwise twist amplitude distribution, $\bar{\alpha}_T$ is the twist amplitude at some reference station (in the present case, the reference station is at the blade tip), and $f_\alpha(r)$ is the normalized mode shape distribution. The subscript 2 has been appended to the unsteady two-dimensional moment to distinguish it from the three-dimensional quantity which will be introduced presently. The generalized force per unit span in torsion is obtained by dividing the virtual work by the virtual displacement.

$$Q_\alpha^{*/} = \frac{\delta W}{\delta \bar{\alpha}_T} = \left(\frac{M_{U_2}^{*}}{r_T - r_0}\right) f_\alpha(r) \tag{89}$$

Hence, the generalized force over the entire span (i.e., the three-dimensional unsteady moment) is obtained by integrating Eq. (89) over the span of the rotor blade, or

$$M_{U_3}^{*} = \int_{r_0}^{r_T} Q_\alpha^{*/} dr = \frac{1}{r_T - r_0} \int_{r_0}^{r_T} M_{U_2}^{*} f_\alpha(r)\, dr \tag{90}$$

As in Eq. (69), the two- and three-dimensional moment coefficients are defined by the formulas

$$M_{U2}^{*}(r) = \frac{1}{2}\rho(r)U^2(r)\left[2b(r)\right]^2 C_{M_{U2}}^{*}(r)$$

$$M_{U3}^{*} = \frac{1}{2}\rho_T U_T^2 (2b_T)^2 C_{M_{U3}}^{*} \tag{91}$$

where the subscript T denotes values taken at some reference station. After Eqs. (91) are substituted into Eq. (90) and the equation is divided through by the reference quantities, the result is given by

$$C_{M_{U3}}^{*} = \frac{1}{r_T - r_0}\int_{r_0}^{r_T}\left(\frac{\rho U^2 b^2}{\rho_T U_T^2 b_T^2}\right) C_{M_{U2}}^{*} f_\alpha(r)\,dr \tag{92}$$

The imaginary part of each side of the equation will now be taken, in amplitude form, and use will also be made of the dimensionless spanwise variable

$$\eta = \frac{r - r_0}{r_T - r_0} \tag{93}$$

whereupon Eq. (92) becomes

$$\bar{C}_{M_{U3I}} = \int_0^1 \left(\frac{\rho U^2 b^2}{\rho_T U_T^2 b_T^2}\right) \bar{C}_{M_{U2I}} f_\alpha(\eta)\,d\eta \tag{94}$$

The two-dimensional moment coefficient amplitude function on the right-hand side of Eq. (94) may now be replaced by Eq. (36); and after using Eqs. (39) and (88) for μ and $\alpha(\eta)$, respectively, Eq. (94) becomes

$$\bar{C}_{M_{U3I}} = -\bar{\alpha}_T \int_0^1 \left(\frac{\rho U^2 b^2}{\rho_T U_T^2 b_T^2}\right) \Xi_{\alpha 2} f_\alpha^2(\eta)\,d\eta \tag{95}$$

As in Eq. (35), the three-dimensional aerodynamic damping in pitch will be defined by the derivative form,

$$\Xi'_{\alpha_3} = - \frac{d\bar{C}_{M_{U3I}}}{d\bar{\alpha}_T} \tag{96}$$

After the operation defined by Eq. (96) is applied to Eq. (95) the result is

$$\Xi_{\alpha_3} = \int_0^1 \left(\frac{\rho U^2 b^2}{\rho_T U_T^2 b_T^2} \right) \Xi_{\alpha_2} f_\alpha^2(\eta) \, d\eta \tag{97}$$

In the most general case, Eq. (97) takes into account the possible spanwise variations in the parameters ρ, U, and b. However, in the present study, both the density and the semichord will be assumed to be constant over the entire active span of the rotor blade, and only the velocity will be considered to be a variable quantity. Thus, after defining the spanwise velocity ratio by the formula

$$\nu(\eta) = U(\eta)/U_T \tag{98}$$

the final form of the three-dimensional damping parameter will be

$$\Xi_{\alpha_3} = \int_0^1 \Xi_{\alpha_2} \nu^2(\eta) f_\alpha^2(\eta) \, d\eta \tag{99}$$

Unclassified

Security Classification

DOCUMENT CONTROL DATA - R & D

(Security classification of title, body of abstract and indexing annotation must be entered when the overall report is classified)

1. ORIGINATING ACTIVITY (Corporate author) Sikorsky Aircraft Division of United Aircraft Corporation Stratford, Connecticut	2a. REPORT SECURITY CLASSIFICATION Unclassified 2b. GROUP

3. REPORT TITLE

PREDICTION OF ROTOR INSTABILITY AT HIGH FORWARD SPEEDS
VOLUME III - STALL FLUTTER

4. DESCRIPTIVE NOTES (Type of report and inclusive dates)
Final Report

5. AUTHOR(S) (First name, middle initial, last name)
Franklin O. Carta
Charles F. Niebanck

6. REPORT DATE	7a. TOTAL NO. OF PAGES	7b. NO. OF REFS
February 1969	99	15

8a. CONTRACT OR GRANT NO.	9a. ORIGINATOR'S REPORT NUMBER(S)
DA 44-177-AMC-332(T) b. PROJECT NO. Task 1F125901A13904 c. d.	USAAVLABS Technical Report 68-18C 9b. OTHER REPORT NO(S) (Any other numbers that may be assigned this report) SER-50469

10. DISTRIBUTION STATEMENT

This document has been approved for public release and sale; its distribution is unlimited.

11. SUPPLEMENTARY NOTES	12. SPONSORING MILITARY ACTIVITY
Volume III of a 5-volume report	US Army Aviation Materiel Laboratories Fort Eustis, Virginia

13. ABSTRACT

The analytical study in this volume was carried out to determine the susceptibility of helicopter rotor blades to a stall flutter instability. This analysis was based on the use of unsteady aerodynamic data previously obtained by Sikorsky Aircraft for an NACA 0012 airfoil oscillating in pitch about its quarter-chord over a wide range of values of incidence angle, oscillatory frequency, amplitude of motion, and free-stream velocity. These data were originally available in the form of moment coefficient-incidence angle loops, and a twofold task was performed in carrying out the present study. First, it was necessary to convert the moment coefficient data to an aerodynamic damping parameter form. This was accomplished by integrating the moment over one cycle of motion to yield the aerodynamic work per cycle, and this in turn was multiplied by appropriate conversion factors to produce the desired two-dimensional aerodynamic damping. Second, it was necessary to apply these two-dimensional results to a helicopter rotor to evaluate the weighted three-dimensional damping at each azimuth station, and to interpret the implications of any predicted region of instability.

The stall flutter analysis was used in conjunction with the blade motion solution of Volume I to provide flight condition boundaries for stall flutter intensity.

DD FORM 1 NOV 68 1473 REPLACES DD FORM 1473, 1 JAN 64, WHICH IS OBSOLETE FOR ARMY USE.

Unclassified

Security Classification

14 KEY WORDS	LINK A		LINK B		LINK C	
	ROLE	WT	ROLE	WT	ROLE	WT
Helicopter Rotor Blade Flutter						